

# Faculteit Industriële Ingenieurswetenschappen

master in de industriële wetenschappen: nucleaire  
technologie

**Masterthesis**

**Statistical evaluation of the envelope geometry for efficiency calibration in gamma spectrometry**

**Julie De Maere**

Scriptie ingediend tot het behalen van de graad van master in de industriële wetenschappen: nucleaire technologie,  
afstudeerrichting nucleair en medisch

**PROMOTOR :**

Prof. dr. Wouter SCHROEYERS

**PROMOTOR :**

ir. Andrea GOMES

Gezamenlijke opleiding UHasselt en KU Leuven



Universiteit Hasselt | Campus Diepenbeek | Faculteit Industriële Ingenieurswetenschappen | Agoralaan Gebouw H - Gebouw B | BE 3590 Diepenbeek

Universiteit Hasselt | Campus Diepenbeek | Agoralaan Gebouw D | BE 3590 Diepenbeek  
Universiteit Hasselt | Campus Hasselt | Martelarenlaan 42 | BE 3500 Hasselt



2024  
2025

# Faculteit Industriële Ingenieurswetenschappen

master in de industriële wetenschappen: nucleaire  
technologie

## ***Masterthesis***

***Statistical evaluation of the envelope geometry for efficiency calibration in gamma spectrometry***

**Julie De Maere**

Scriptie ingediend tot het behalen van de graad van master in de industriële wetenschappen: nucleaire technologie,  
afstudeerrichting nucleair en medisch

## **PROMOTOR :**

Prof. dr. Wouter SCHROEYERS

## **PROMOTOR :**

ir. Andrea GOMES



**KU LEUVEN**



# Preface

As I reach the end of my academic journey, I would like to take a moment to express my sincere gratitude to all those who have supported me over the past years and contributed to making this achievement possible. The path leading here has not always been easy; every chapter and every page of this work has been shaped by support and collaboration.

First and foremost, I wish to express my sincere thanks to my mentor at CERN, Ir. Andrea Gomes. His continuous guidance, willingness to share his knowledge, and trust in me during my time at CERN have left a lasting impression. He inspired me through his new insights and perspectives, and I am deeply grateful for his close collaboration and care for my professional development.

I would also like to thank my internal supervisor, Prof. Dr. Wouter Schroeyers, whose support enabled me to realise my internship at CERN. His unwavering dedication and generous availability played a vital role in the completion of this thesis. Throughout my studies at UHasselt, his teaching greatly enriched my understanding and knowledge, and his guidance has been key to my development as a researcher.

My most profound appreciation goes to my parents. Their unconditional encouragement and support throughout my academic journey have been invaluable in bringing me to where I stand today. Thanks to their endless support, I have always persevered and am privileged to have received every opportunity I wished to pursue.

Finally, I would like to thank my friends for their support and their positive influence on me and my personal development. I am grateful for the enjoyable moments of relaxation, shared study sessions, and the many good times we experienced together.



# Contents

|  |           |
|--|-----------|
| <b>Word before</b>   | <b>1</b>  |
| <b>List of tables</b>  | <b>7</b>  |
| <b>List of figures</b>   | <b>10</b> |
| <b>Abstract in English</b>   | <b>11</b> |
| <b>Abstract in Dutch</b>   | <b>13</b> |
| <b>1 Introduction</b>  | <b>15</b> |
| 1.1 Host institution/situation . . . . .                                   | 16        |
| 1.2 Problem statement . . . . .  | 17        |
| 1.3 Objectives . . . . .   | 19        |
| 1.4 General methodology . . . . .  | 20        |
| 1.5 Outlook . . . . .  | 21        |
| <b>2 Literature study</b>  | <b>23</b> |
| 2.1 Gamma spectrometry . . . . .   | 24        |
| 2.1.1 Gamma interaction with matter . . . . .                              | 25        |
| 2.1.2 Semiconductor counter . . . . .                                      | 30        |
| 2.1.3 Calibration . . . . .  | 33        |
| 2.1.4 Recent developed methods for performing efficiency calibration . . . | 36        |
| 2.2 Envelope geometry . . . . .  | 38        |
| 2.2.1 ISOCS/LabSOCS . . . . .  | 39        |
| 2.2.2 Previous similar research on ISOCS/LabSOCS software . . . . .        | 41        |
| 2.2.3 Uncertainty . . . . .  | 46        |

|          |   |           |
|----------|---|-----------|
| 2.3      | Statistical techniques . . . . .  | 48        |
| 2.3.1    | Hypothesis testing . . . . .  | 48        |
| 2.3.2    | Kullback-Leibler divergence . . . . .   | 50        |
| 2.3.3    | Bootstrap method . . . . .  | 51        |
| <b>3</b> | <b>Materials and methodology</b>  | <b>53</b> |
| 3.1      | Materials . . . . .   | 54        |
| 3.1.1    | R programming language . . . . .  | 54        |
| 3.1.2    | Compiled database used for this study . . . . .                                     | 54        |
| 3.1.3    | Nuclide information . . . . .   | 57        |
| 3.1.4    | Extended Range Coaxial Germanium detector . . . . .                                 | 59        |
| 3.2      | Methodology . . . . .   | 61        |
| 3.2.1    | Comparison of measurement methods . . . . .   | 61        |
| 3.2.2    | Estimation of measurement deviations introduced by the envelope<br>method . . . . . | 64        |
| <b>4</b> | <b>Results and discussion</b>   | <b>69</b> |
| 4.1      | Comparison of measurement methods . . . . .   | 70        |
| 4.1.1    | Wilcoxon signed-rank test . . . . .   | 70        |
| 4.1.2    | Paired t-test and Shapiro-Wilk test . . . . .                                       | 71        |
| 4.1.3    | Discussion of results . . . . .   | 73        |
| 4.2      | Estimation of measurement deviations introduced by the envelope method              | 74        |
| 4.2.1    | The error . . . . .   | 74        |
| 4.2.2    | The uncertainty . . . . .   | 76        |
| 4.2.3    | The bias . . . . .  | 82        |
| 4.2.4    | Discussion of results . . . . .   | 83        |
| <b>5</b> | <b>Experimental activity and laboratory measurements</b>                            | <b>87</b> |
| 5.1      | Objective . . . . .   | 88        |
| 5.2      | Samples and instrumentation . . . . .   | 88        |
| 5.3      | Methodology . . . . .   | 90        |
| 5.4      | Results . . . . .   | 93        |
| <b>6</b> | <b>Conclusion</b>   | <b>97</b> |

|   |     |
|---|-----|
| Literature list                         | 99  |
| Annex A: Gamma spectrometry report CERN | 105 |





# List of Tables

|     |   |    |
|-----|---|----|
| 2.1 | Summary of ISOCS validation results for laboratory geometries across energy ranges . . . . .  | 42 |
| 2.2 | Results from analysing reference source as unknown for Co-60 . . . . .  | 43 |
| 2.3 | Summary of accuracy and precision from first 13 ISOXVRFY detectors . .  | 43 |
| 2.4 | Comparison of activity concentration results using different efficiency calibration methods . . . . .   | 45 |
| 2.5 | Relative bias and Z-score of Co-60 for different efficiency calibration methods   | 46 |
| 3.1 | Average relative uncertainty ( $2\sigma$ ) measured by CERN and Jacobs for Co-60 and Ti-44 . . . . .  | 55 |
| 4.1 | Results of the Wilcoxon signed-rank test for Co-60 and Ti-44 . . . . .  | 70 |
| 4.2 | Results of the Shapiro-Wilk test for Co-60 and Ti-44 . . . . .  | 72 |
| 4.3 | FWHM values for different bin sizes of the activity ratio (C/J) distribution for Co-60 and Ti-44 . . . . .  | 76 |
| 4.4 | Mean, standard deviation, and pseudo- $R^2$ for the fitted distributions of the Co-60 and Ti-44 activity ratios. For the log-normal distribution, values were back-transformed from the log scale. For the gamma distribution, the mean and standard deviation were computed from the shape and rate parameters | 78 |
| 5.1 | Overview of sample characteristics used in gamma spectrometry measurements  | 89 |
| 5.2 | Identified radionuclides for sample 1. Half-lives are expressed as Y (years), M (months), and H (hours) . . . . .   | 94 |



# List of Figures

|     |   |    |
|-----|---|----|
| 1.1 | CERN accelerator complex . . . . .  | 17 |
| 2.1 | Schematic representation of Compton scattering . . . . .  | 26 |
| 2.2 | Electron energy distribution: Compton continuum and Compton edge . . .  | 28 |
| 2.3 | Photon interaction attenuation coefficients in matter as a function of photon<br>energy . . . . .   | 29 |
| 2.4 | Block diagram of a basic gamma spectrometry system . . . . .  | 30 |
| 2.5 | Intrinsic full energy peak efficiency for germanium detectors as a function<br>of incident photon energy . . . . .  | 35 |
| 2.6 | ISOCS calibration template . . . . .  | 40 |
| 2.7 | The geometry template window in ISOCS software . . . . .  | 41 |
| 2.8 | One-tailed hypothesis testing . . . . .   | 49 |
| 2.9 | Two-tailed hypothesis testing . . . . .   | 49 |
| 3.1 | Established database in R of all samples measured by CERN and Jacobs .  | 55 |
| 3.2 | Scatter plot of the ratio of measured activity from CERN to reference<br>activity from Jacobs (C/J), based on 134 Co-60 samples and 44 Ti-44 samples                  | 56 |
| 3.3 | Decay scheme Co-60 . . . . .  | 58 |
| 3.4 | Decay scheme of Ti-44 . . . . .   | 59 |
| 3.5 | XtRa Coaxial Germanium detector . . . . .   | 60 |
| 3.6 | Efficiency curves for the XtRa with Be window and standard with Li window<br>Coaxial Detector, computed with a source-to-detector distance of 2.5 cm .                | 60 |
| 3.7 | Schematic representation of the three different types of skewness in the<br>distribution of data . . . . .  | 68 |
| 4.1 | Density plot (bandwidth = 4) of the differences in Co-60 activity measure-<br>ments between CERN and Jacobs (CERN – Jacobs), based on 134 paired<br>samples . . . . . | 71 |

|      |   |    |
|------|---|----|
| 4.2  | Density plot (bandwidth = 4) of the differences in Ti-44 activity measurements between CERN and Jacobs (CERN – Jacobs), based on 44 paired samples . . . . .                        | 71 |
| 4.3  | Kernel Density Estimation plot of Co-60 activity measurements from CERN and Jacobs, based on 134 samples . . . . .  | 74 |
| 4.4  | Kernel Density Estimation plot of Ti-44 activity measurements from CERN (Q(x)) and Jacobs (P(x)), based on 44 samples . . . . .   | 75 |
| 4.5  | Density plot (bandwidth = 0.06) of Co-60 activity ratio (C/J), based on 134 samples . . . . .   | 77 |
| 4.6  | Density plot (bandwidth = 0.06) of Ti-44 activity ratio (C/J), based on 44 samples . . . . .  | 77 |
| 4.7  | Histogram of the Co-60 (top) and Ti-44 (bottom) activity ratios between CERN and Jacobs (C/J) with parametric distribution fits . . . . .   | 78 |
| 4.8  | Histogram of the FWHM values obtained from bootstrap resampling of the Co-60 activity ratio (C/J) . . . . .   | 79 |
| 4.9  | Histogram and density estimate of the Co-60 activity ratios between CERN and Jacobs (C/J), using an optimal bandwidth of 0.0477 derived from the bootstrap-estimated FWHM . . . . . | 80 |
| 4.10 | Histogram and density estimate of the Ti-44 activity ratios between CERN and Jacobs (C/J), using an optimal bandwidth of 0.2499 derived from the bootstrap-estimated FWHM . . . . . | 80 |
| 5.1  | Measurement setups for performing gamma spectrometry . . . . .  | 90 |
| 5.2  | LabSOCS tab showing simplified box template in Apex-Gamma software . . . . .  | 91 |
| 5.3  | LabSOCS “Edit Dimensions” tab in a selected template . . . . .  | 91 |
| 5.4  | Efficiency curve in Apex-Gamma software following efficiency calibration . . . . .  | 92 |
| 5.5  | Peak fitting tab in Apex-gamma software . . . . .   | 92 |
| 5.6  | Sample 1 geometry settings using the simplified box template . . . . .  | 93 |
| 5.7  | Sample 1 spectrum with characteristic peaks . . . . .   | 94 |

# Abstract in English

At CERN, gamma spectrometry is a key technique for determining radionuclide activity during radiological characterisation. The so-called envelope method simplifies efficiency calibration for irregular samples by applying predefined standard geometries, modelled via In Situ Object Counting System (ISOCS) and Laboratory Sourceless Calibration Software (LabSOCS). However, discrepancies between real and modelled geometries can introduce systematic errors. This study assesses the accuracy of the envelope method and estimates the associated error, uncertainty, and bias.

Two representative radionuclides (Co-60 and Ti-44) were selected based on the availability of high-quality data. Identical samples were analysed at CERN using calibration based on the envelope method, and by an external reference laboratory (Jacobs) serving as the reference standard. The Wilcoxon signed-rank test and paired t-test were applied to test for significant differences. Additionally, the Kullback–Leibler divergence quantified the error.

The results reveal statistically significant differences between the two approaches, particularly for Ti-44. Nevertheless, the overall agreement may be acceptable given the operational advantages of the envelope method. While no formal acceptance criteria currently exist for the observed error, uncertainty, and bias, this study provides a technical assessment that will support CERN in defining performance thresholds and evaluating its potential for implementation.



# Abstract in Dutch

Gammaspectrometrie is bij CERN een essentiële techniek voor het bepalen van de activiteit van radionucliden tijdens radiologische karakterisering. De zogenoemde envelopmethode vereenvoudigt efficiëntiekalibratie van onregelmatige stalen via vooraf gedefinieerde standaardgeometrieën, gemodelleerd door In Situ Object Counting System (ISOCS) en Laboratory Sourceless Calibration Software (LabSOCS). Verschillen tussen werkelijke en gemodelleerde geometrieën kunnen echter systematische fouten veroorzaken. Deze studie beoordeelt de nauwkeurigheid van de envelopmethode en schat de bijbehorende fout, onzekerheid en systematische afwijking.

Twee representatieve radionucliden (Co-60 en Ti-44) werden gekozen op basis van de beschikbaarheid van kwaliteitsvolle data. Identieke stalen zijn geanalyseerd door CERN, met kalibratie gebaseerd op de envelopmethode, en door een extern referentielaboratorium (Jacobs) dat als referentiestandaard fungeert. De Wilcoxon signed-rank-test en gepaarde t-test zijn toegepast om significante verschillen te toetsen. Daarnaast werd de Kullback–Leibler-divergentie gebruikt om de afwijking te kwantificeren.

De resultaten tonen statistisch significante verschillen tussen beide methoden, vooral voor Ti-44. Desondanks kan de algemene overeenkomst acceptabel zijn, gezien de praktische voordelen van de envelopmethode. Hoewel formele acceptatiecriteria ontbreken, biedt deze studie een technische basis voor CERN om prestatiegrenzen te bepalen en het potentieel voor implementatie te evalueren.





# Chapter 1

## Introduction

This chapter outlines the context in which this research on the statistical evaluation of the envelope geometry for efficiency calibration in gamma spectrometry occurs. Then, it presents the problem statement of the research and discusses the challenges and limitations related to the envelope geometry.

In addition, the research objectives are presented, which are aimed at finding the correction factor when using envelope geometry by making statistical comparisons and determining the acceptability of this method. The general methodology of the study is then described, including the steps that will be taken to achieve the stated objectives. Finally, an outlook describes the follow-up and consistency of the forthcoming text sections.

In summary, this chapter provides an overview of the background, problem statement, objectives, methodology, and outlook of the study, laying the foundation for further detailed discussion and analysis in the following chapters.

## 1.1 Host institution/situation

CERN (European Organisation for Nuclear Research) is the world's largest particle physics laboratory, located on the French-Swiss border near Geneva. The institute is dedicated to uncovering the fundamental building blocks of the universe and to understand its workings. This is achieved through various particle accelerator facilities that enable researchers to conduct groundbreaking experiments. CERN's mission includes performing world-class research in fundamental physics in an environmentally responsible and sustainable manner [1].

The CERN Accelerator Complex (figure 1.1) is an advanced system of interconnected machines designed to accelerate particles to higher energies. It operates as a staged sequence, where each accelerator increases the energy of a particle beam before transferring it to the next. At the core of this system is the Large Hadron Collider (LHC), where particle beams reach a record energy of 6.8 TeV per beam and are brought into collision at four primary detectors: ALICE, ATLAS, CMS, and LHCb. The process begins with Linear Accelerator 4 (Linac4), which generates negative hydrogen ions and accelerates them before injecting them into the Proton Synchrotron Booster (PSB). During this transition, the ions are stripped of their electrons, leaving only protons, which are then accelerated through the Proton Synchrotron (PS) and the Super Proton Synchrotron (SPS) before being injected into the LHC. Besides proton acceleration, CERN's complex includes additional accelerators designed for experiments with other particles, such as lead ions, and facilities dedicated to antimatter research, radioactive ion studies, and neutrino physics [2], [3].

CERN is structured into various units (or departments), groups, and sections. This research is conducted within the HSE-RP-CS section. The Occupational Health & Safety and Environmental Protection (HSE) Unit ensures a highly service-oriented approach for both the radiological and conventional safety domains. Within HSE, the Radiation Protection (RP) group focuses on maintaining safe working conditions by reducing exposure to ionising radiation for both personnel and the environment. This includes monitoring and mitigating radiation risks across CERN's facilities. The Characterisation and Services (CS) section, one of five sections within RP, is crucial in managing CERN's radioactive waste and radioactive source characterisation. It also provides essential services related to radioactive materials, including sample analysis [4].

Gamma spectrometry is a key technique at CERN for identifying and measuring radionuclides based on their characteristic gamma peaks. Measured objects at CERN can include radioactive waste samples as well as reference materials used to validate experimental simulation data.

However, gamma spectrometry is challenged by the irregular geometry of many objects, such as screws and cables from accelerators, which complicates the analysis. The shape, density, and composition of these objects significantly influence the efficiency of measurement instruments. These factors affect the detector's response, ultimately impacting the accuracy of activity quantification [5].

## The CERN accelerator complex *Complexe des accélérateurs du CERN*

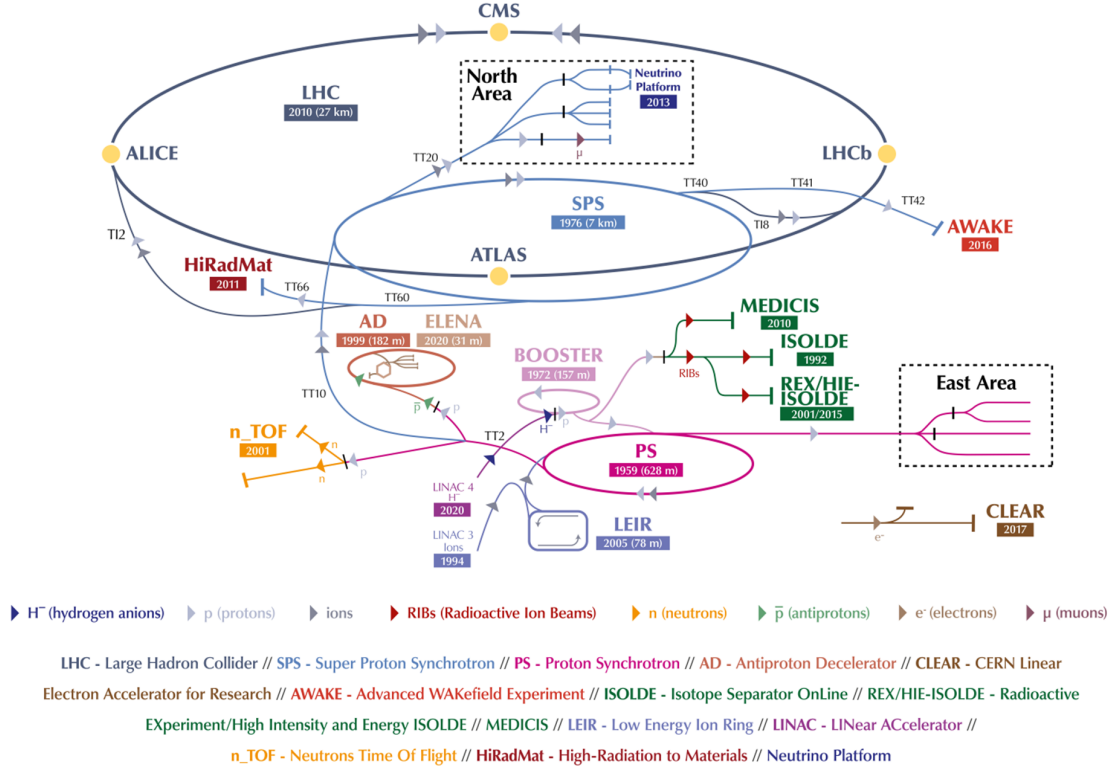


Figure 1.1: CERN accelerator complex [2].

## 1.2 Problem statement

For the radiological characterisation of samples, activity measurement is essential. One of the methods used at CERN is gamma spectrometry. The accuracy of these measurements depends on the net peak area, the absolute efficiency corresponding to the geometric model, the photon intensity, and the spectrum acquisition time. Precision in gamma spectrometry is ensured through efficiency calibration, which corrects for detector response variations, enabling accurate and reproducible radiation measurements [5].

Efficiency calibration is inherently dependent on the geometry of the measured object. However, implementing a specific geometry for each sample in gamma spectrometry is a time intensive process. CERN laboratory has implemented the envelope method, a calibration technique that enhances operational efficiency by using envelope geometry. Instead of calibrating each sample individually, this method establishes an efficiency curve that accounts for geometric variations. It relies on ISOCS and LabSOCS software, which provide a library of predefined standard geometries [6]. This method, developed in recent decades, enables the calibration of samples with varying shapes, a factor that traditionally complicates measurement accuracy. Matching the sample geometry to the closest available standard allows for activity determination while simplifying the gamma spectrometry protocol through the use of ISOCS and LabSOCS standard geometries [7]. An exact match is not always possible, and as a result the measured activity may deviate from the true value, introducing an inherent error.

Another approach for activity measurements, which employs a well-defined geometry, is radiochemical analysis. This method standardises the sample's geometry before analysis, ensuring precise calibration and establishing it as a reference technique for radioactive sample measurement. However, CERN does not conduct radiochemical analysis internally; these measurements are outsourced to specialised external laboratories [7].

The research hypothesis in this study is that the envelope method in activity measurements introduces a systematic error due to geometric simplifications, but the magnitude of this error is unknown. To quantify it, measurements from the envelope method must be compared with those from radiochemical analysis. This requires the development of a structured database to ensure organised and accessible data for statistical analysis. A key challenge is selecting the most reliable statistical comparison method, as multiple approaches exist. Additionally, there are no established criteria for determining whether the identified error is acceptable.

This study assesses whether the envelope method remains a viable alternative by statistically evaluating its error. Currently, the envelope method is not yet used in gamma spectrometry because the magnitude of its error is unknown. If this research determines that the error is quantifiable and within an acceptable range, the method could provide a faster and more practical alternative for efficiency calibration, making it a viable option for industrial implementation.

## 1.3 Objectives

The primary objective of this thesis is to evaluate the acceptability of the error introduced by using envelope geometries. To achieve this, the research is structured into several key phases, ensuring a clear and systematic approach.

The first objective is to understand the study as well as possible, which involves looking for clarification of measurement and statistical methods in literature, such as books, articles and websites. Following this, a structured database needs to be developed, containing measurements obtained using both the envelope method and radiochemical analysis. This database needs to be clear, complete and optimised for future programming and data analysis use. Next, the focus will be on gaining a deeper understanding of the mechanism behind the envelope method. To achieve this, efficiency calibration tests in gamma spectrometry need to be carried out in the laboratory using ISOCS/LabSOCS software. Following the tests, a statistical comparison must be performed between the radiochemical analysis and the envelope method. This analysis will provide an estimate of the error introduced by the envelope approach.

The final aim of this research is to assess the acceptability of the identified error, particularly as no predefined thresholds for error have been established. This evaluation needs to involve a strategic trade-off between measurement accuracy and operational efficiency. Preliminary criteria for accepting or rejecting the envelope method must be set. The goal is to provide CERN with a detailed technical study of the performance of the envelope method, and the final decision of acceptance will be taken considering both the potential drawbacks of the error and the benefits of a more streamlined process. Even if the statistical analysis reveals significant discrepancies between the methods, this study will still provide valuable insights into their respective strengths and limitations. The dataset, compiled with data from 2020-2023 measurements at CERN, ensures a robust and comprehensive evaluation between the envelope method and radiochemical analysis.

## 1.4 General methodology

The work is divided into distinct work packages (WP) to structure the research process effectively, each representing a key phase.

### WP1: Literature review

The first phase involves an extensive literature review to develop a comprehensive research framework. This consists of consulting various sources, such as websites, books, and scientific papers, independently gathered and provided by CERN. Establishing a solid theoretical foundation is essential for gaining a deeper understanding of the research and selecting the most suitable methodological approach.

### WP2: Data collection

At CERN, data related to the envelope efficiency calibration method has been collected. The analysis will focus on a reduced number of significant nuclides, for which both gamma spectrometry using the envelope method and radiochemical analysis have been performed. A thorough understanding of the database is essential for accurate data analysis. This involves reviewing relevant documentation and gaining familiarity with data sources and acquisition methods.

### WP3: Laboratory screening

The datasets used in this study were obtained over several years in a radiologically supervised laboratory at CERN. Additionally, laboratory experiments will be conducted to provide deeper insight into the experimental process, the theoretical principles underlying the envelope method in gamma spectrometry, efficiency calibration, and 3D modelling with ISOCS/LabSOCS. A comprehensive knowledge of laboratory procedures is essential, as these experiments will not only enhance learning but also provide valuable insights into the technical aspects of the methodology.

Access to the laboratory requires completion of CERN mandatory safety training, including online modules on general safety, emergency evacuations, and radiation protection in supervised areas. In addition, an in-person session on radiation protection in controlled areas must be completed to allow potential access to other laboratories.

Jacobs, based in the US, provides services to nuclear operators, decommissioning contractors, and consultants specialising in contaminated areas. The radiochemical analyses of CERN samples are conducted by Jacobs, who then provides the relevant reports, which must be interpreted accurately [8].

### WP4: Statistical analysis and critical interpretation

Statistical analysis and critical interpretation of results are key to effectively comparing the two methods. In this phase, the programming language R is used and offers a wide range of tools for statistical analysis, data manipulation, and creating visualisations. It is especially powerful for handling large datasets and performing complex calculations. To acquire the necessary skills, two online Udemy courses [9], Data Science and Machine Learning Bootcamp with R and Probability & Statistics Mastery, will be completed.

## 1.5 Outlook

This section outlines the structure of the following chapters, providing a concise overview of what to expect in this study.

Chapter 2 serves as a background study, offering a detailed explanation of gamma spectrometry, envelope geometry, and various statistical techniques. It also functions as a state-of-the-art review, referencing similar studies conducted in the past to enable comparison between previous findings and the new results presented in this thesis.

Chapter 3 provides an overview of the different materials used to perform this study. It also describes the methodologies applied during the statistical tests conducted. Several references are made to chapter 2, as a solid background understanding is necessary to grasp the purpose of the tests.

Chapter 4 presents all the results and plots of the tests described in chapter 3. This includes a discussion section that offers further interpretation of the statistical results. A comparison is also made with the findings from the state-of-the-art review (chapter 2), assessing the implications for a potential implementation of the envelope method.

Chapter 5 presents a laboratory report in which three samples were measured using gamma spectrometry, with efficiency calibration performed via the envelope method.

Finally, chapter 6 provides the concluding remarks of this study.





# Chapter 2

## Literature study

Chapter 2 provides an in-depth exploration of various key aspects of gamma spectrometry, grounded in an understanding of the fundamental interactions between photons and matter. This includes a detailed exploration of these interactions, the equipment involved, and the importance of various calibration techniques.

The chapter then shifts the focus to the envelope method, a simplified approach for efficiency calibration in gamma spectrometry. It covers the principles behind the method, the software used, and the main sources of uncertainties. The final subsection introduces the general framework of hypothesis testing, the Kullback-Leibler divergence and the bootstrap method, which are crucial to understand the statistical tests applied later in the thesis.

## 2.1 Gamma spectrometry

Gamma rays are high-energy photons with no mass or charge, emitted when an atomic nucleus transitions from an excited state to a lower energy level. In the nucleus, nucleons occupy discrete energy levels, similar to electrons in atomic orbitals. A nucleus becomes excited when a nucleon is promoted to a higher energy level as a result of a nuclear reaction or radioactive decay. It then emits gamma radiation to release excess energy, without changing its number of nucleons. The energy range of gamma rays is between 100 keV and 10 GeV. Gamma rays have strong penetrating power compared to alpha and beta radiation. While alpha particles are stopped by paper (0.05 mm) and beta particles by metal (2-5 mm aluminium), gamma rays require dense materials like lead (10 cm) or thick concrete (1 m) for shielding. This high penetration capability arises from gamma photons interacting with matter primarily through processes such as the photoelectric effect, Compton scattering, and pair production rather than through strong interactions like those experienced by charged particles.

Gamma spectrometry is a technique that enables the detection and identification of gamma-emitting radionuclides by analysing the energy of the gamma rays emitted by a sample. It plays an essential role in radioactive waste management to characterise radionuclides present in waste samples, and it also allows for precise measurement of gamma energies. One of its advantages is the relative simplicity of sample preparation, as radiochemical separation is often unnecessary. Computer software can process data from the detection system, enabling automation in the analysis. Since each emitted gamma photon corresponds to an energy peak, accurate energy measurements require precise energy and efficiency calibrations [10].

Factors such as geometry, material composition, and source-to-detector distance influence the measurement efficiency. Predefined models, e.g. ISOCS, can be used when these factors are not precisely known but have the disadvantage of inherently introducing uncertainties. These uncertainties can cause deviations in efficiency calibration, which in turn affect the accuracy of activity measurements. Without addressing these uncertainties, the precision of gamma spectrometry results could be compromised [10], [11].

Achieving accurate measurements requires reducing systematic errors, enhancing precision, and improving reproducibility. The following sections focus on gamma-matter interactions, detector operation, and calibration principles.

### 2.1.1 Gamma interaction with matter

Photons are a form of indirectly ionising radiation. Rather than ionising atoms directly, they transfer energy to charged particles (primarily electrons), which in turn cause ionisation through subsequent interactions. The interactions of photon radiation with matter depend on both the energy of the photon and the atomic number ( $Z$ ) of the material. They can be broadly classified into two categories: absorption and scattering mechanisms.

During an absorption event, the photon is fully absorbed and its energy is transferred to secondary charged particles. On the other hand, scattering can occur in two forms. In elastic scattering, a photon interacts with matter without losing energy, changing only its direction. In inelastic scattering, the photon transfers part of its energy to a charged particle, such as an electron. This interaction changes both the energy and direction of the photon.

The primary absorption processes in the gamma rays energy range are the photoelectric effect and pair production, while Compton scattering is the dominant scattering interaction.

These interactions can be further subdivided at the atomic scale: the photoelectric effect and Compton scattering are examples of photon-orbital electron interactions, while pair production is classified as a photon-nucleus interaction.

Photon-orbital electron interactions depend on the electron binding energy relative to the photon energy. For low  $Z$  materials, valence electrons have binding energies on the order of a few eV, while for high  $Z$  materials, inner-shell electrons may have binding energies up to tens of keV. When a photon interacts with an electron whose binding energy is negligible compared to the energy of the photon, the electron behaves as if it were free during the interaction, even though it remains bound under normal conditions. In contrast, the interaction involves the entire atom when a photon interacts with a tightly bound electron whose binding energy is close to the photon energy.

Photon-nucleus interactions can be divided into two main categories: the interaction of a photon with the Coulomb field of the nucleus and the interaction of a photon directly with the nucleus. These high-energy interactions are particularly relevant in nuclear physics and applications such as radiation shielding [12].

#### Photoelectric effect

The photoelectric effect occurs when a gamma photon transfers all its energy to an atomic electron, usually from an inner shell. This results in the ejection of the electron from the atom and the complete absorption of the photon. The ejected electron, also known as the photoelectron, has a kinetic energy equal to the difference between the energy of the incident photon ( $E_\gamma$ ) and the electron binding energy ( $B$ ) in its atomic shell [13]:

$$E_e = E_\gamma - B. \quad (2.1)$$

The probability of the photoelectric effect is shown in equation 2.2. It increases with the atomic number following a power law with an exponent of 5, meaning higher-Z materials are more likely to absorb photons via this process. Conversely, probability decreases with photon energy following a power law with an exponent of -3.5, meaning the photoelectric effect is more dominant at lower photon energies. This effect primarily involves electrons from the K- and L-shells and is most prominent for gamma-ray photons with energies below 50 keV. If the incident photon energy is lower than the electron binding energy, the photoelectric effect cannot occur.

$$P \propto k \frac{Z^5}{E_\gamma^{3.5}} \quad (2.2)$$

where  $P$  is the probability of occurrence,  $k$  is a proportionality constant,  $Z$  is the atomic number, and  $E_\gamma$  is the incident photon energy [14].

### Compton scattering

Compton scattering is an inelastic interaction between a gamma photon and an atomic electron, in which the photon transfers part of its energy to the electron. As a result, the electron, referred to as the recoil electron, is ejected from the atom, while the photon is deflected and re-emitted with lower energy. Its energy and angle are determined by the conservation of energy and momentum. The process is illustrated in figure 2.1 [14].

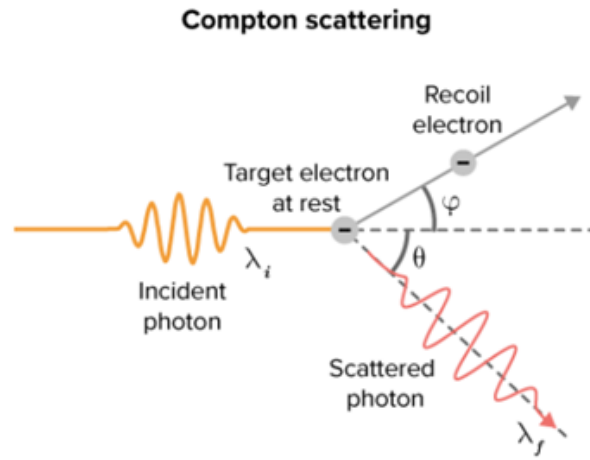


Figure 2.1: Schematic representation of Compton scattering [15].

The energy of the incident photon is  $E = h\nu$  where  $h$  is Planck's constant and  $\nu$  is the frequency of the photon. This initial energy is divided between the recoil electron and the scattered photon. The energy of the scattered photon is given by  $E' = h\nu'$ , while the electron acquires kinetic energy  $T_e$ . The following equation describes the law of conservation of energy:

$$h\nu = h\nu' + T_e. \quad (2.3)$$

Momentum (P), which represents the recoil that the particle undergoes after interacting with the gamma photon, is conserved during the interaction. The conservation of momentum can be expressed for its x- and y-components as follows:

$$x - \text{component} : \frac{h\nu}{c} = \frac{h\nu'}{c} \cos \varphi + P \cos \theta \quad (2.4)$$

$$y - \text{component} : 0 = \frac{h\nu'}{c} \sin \varphi - P \sin \theta. \quad (2.5)$$

The Compton scattering formula (equation 2.6) results from the conservation of momentum and energy during the interaction. It depends on the initial photon energy and the scattering angle  $\theta$ :

$$h\nu' = \frac{h\nu}{1 + \frac{h\nu}{m_0c^2}(1 - \cos \theta)} \quad (2.6)$$

where  $m_0c^2 = 0.511 \text{ MeV}$  is the electron rest mass energy. The energy acquired by the recoil electron is then:

$$E_{e^-} = h\nu - h\nu'. \quad (2.7)$$

According to equation 2.6, the energy transferred to the electron increases with the scattering angle  $\theta$ , reaching its maximum value when  $\theta = \pi$ , corresponding to backscattering of the photon. In this special case, equation 2.6 simplifies to:

$$h\nu' \Big|_{\theta=\pi} = \frac{h\nu}{1 + \frac{2h\nu}{m_0c^2}}. \quad (2.8)$$

Thus, the maximum kinetic energy acquired by the electron becomes:

$$E_{e^-} \Big|_{\theta=\pi} = h\nu - \frac{h\nu}{1 + \frac{2h\nu}{m_0c^2}}. \quad (2.9)$$

When the incident photon energy is much larger than the electron rest mass energy, i.e.  $h\nu \gg m_0c^2$ , equation 2.9 simplifies, and the maximum kinetic energy of the electron approaches a constant value:

$$E_{e^-} \Big|_{\theta=\pi} \approx \frac{m_0c^2}{2} = 256 \text{ keV}. \quad (2.10)$$

Compton scattering is the primary absorption mechanism for gamma rays in the energy range of 100 keV to 10 MeV. The probability of Compton scattering depends on the ratio  $Z/A$ , where  $A$  is the mass number.

In figure 2.2, the features known as the Compton continuum and the Compton edge are illustrated. The Compton continuum refers to the broad range of electron energies produced after a Compton scattering event, as photons can be deflected at any angle within the detector. The Compton edge represents the maximum electron energy achievable through this process, given by

$$E_e|_{\theta=\pi} = h\nu - h\nu'|_{\theta=\pi} = h\nu \left( \frac{\frac{2h\nu}{m_0c^2}}{1 + \frac{2h\nu}{m_0c^2}} \right). \quad (2.11)$$

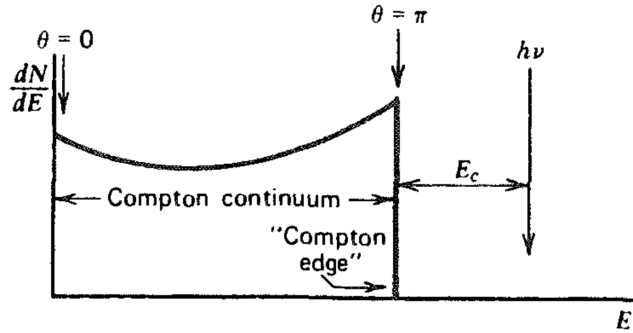


Figure 2.2: Electron energy distribution: Compton continuum and Compton edge [16].

The previous analysis and calculations assumed that the electron struck by the photon was completely free and unbound. However, this is not entirely accurate for electrons within the active region of a semiconductor detector. In reality, the binding energy between the electrons and the atomic nucleus influences the energy distribution. As a result, the sharp drop typically associated with the Compton edge is smoothed out in a real measurement. Additionally, the finite energy resolution of semiconductor detectors further blurs this transition, making the drop less distinct [13], [16].

### Pair production

Pair production is an electromagnetic process in which high-energy gamma photons interact with the electromagnetic field of an atomic nucleus, creating an electron-positron pair. The mass-energy equivalence principle from the theory of relativity, formulated by Einstein,

$$E = m_0c^2 \quad (2.12)$$

states that energy can be converted into mass. In pair production, the photon energy is transformed into the rest mass and kinetic energy of the electron and positron.

Pair production only occurs when the incident photon has an energy of at least 1.022 MeV, corresponding to the combined rest mass energies of an electron and a positron (0.511 MeV each). If the photon energy exceeds this threshold, the excess energy is distributed as kinetic energy between the two created particles.

A photon cannot spontaneously transform into electrons without an external influence due to the conservation of energy and momentum. The presence of an atomic nucleus is necessary to conserve momentum during the conversion. When a high-energy photon enters the strong electromagnetic field surrounding a nucleus, it interacts with this field, creating an electron-positron pair. After losing kinetic energy through interactions with surrounding electrons and matter, the positron comes to rest and undergoes annihilation by combining with a free electron. This process results in the complete conversion of the electron-positron pair to energy, producing two annihilation gamma photons, each having an energy of 0.511 MeV, emitted in opposite directions to maintain momentum. Formed annihilation photons can interact with surrounding matter through the photoelectric effect or Compton scattering, creating further electromagnetic interactions within the material. The probability of pair production increases with the atomic number of the absorbing material and becomes significant for high-energy gamma photons, typically above 5 MeV [13].

### Combined effects

In a medium, multiple types of photon interactions can occur simultaneously or sequentially. A Compton-scattered photon or a photon produced by an annihilation event may be absorbed by photoelectric effect or it may undergo further scattering in another Compton interaction. Figure 2.3 shows the relative contributions of the photoelectric effect, Compton scattering, and pair production to the total attenuation coefficient. In case of pair production, a photon can interact in the Coulomb field of either an atomic nucleus or an orbital electron. Interaction in the nuclear field leads to a higher attenuation coefficient due to the stronger electric field of the nucleus, with charge  $+Ze$ , compared to the electron, which carries a single negative charge. The stronger field increases the probability of interaction. In addition, the large mass of the nucleus allows it to absorb recoil momentum with minimal displacement, unlike the electron. Therefore, pair production in the nuclear field dominates at high photon energies.

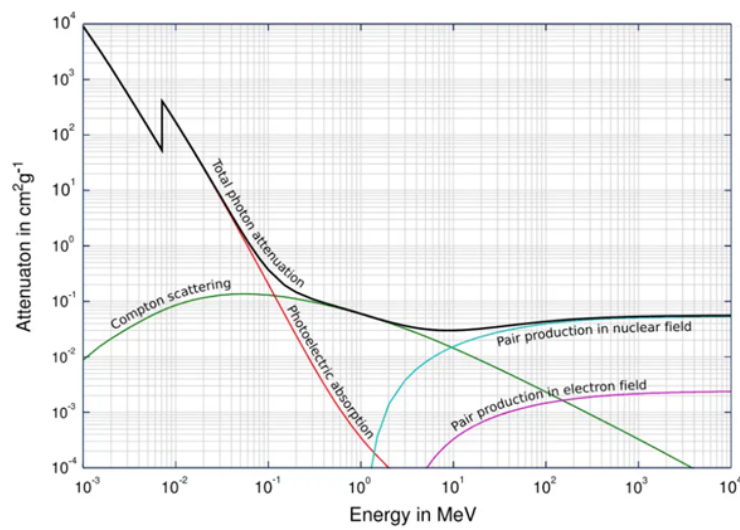


Figure 2.3: Photon interaction attenuation coefficients in matter as a function of photon energy [17].



### 2.1.2 Semiconductor counter

The fundamental components of a typical gamma spectrometry system include a High-Purity Germanium (HPGe) detector, a high-voltage power supply, a preamplifier, an amplifier with an Analogue-to-Digital Converter (ADC), and a Multichannel Analyser (MCA). Figure 2.4 shows a block diagram of a basic gamma spectrometry system [14].

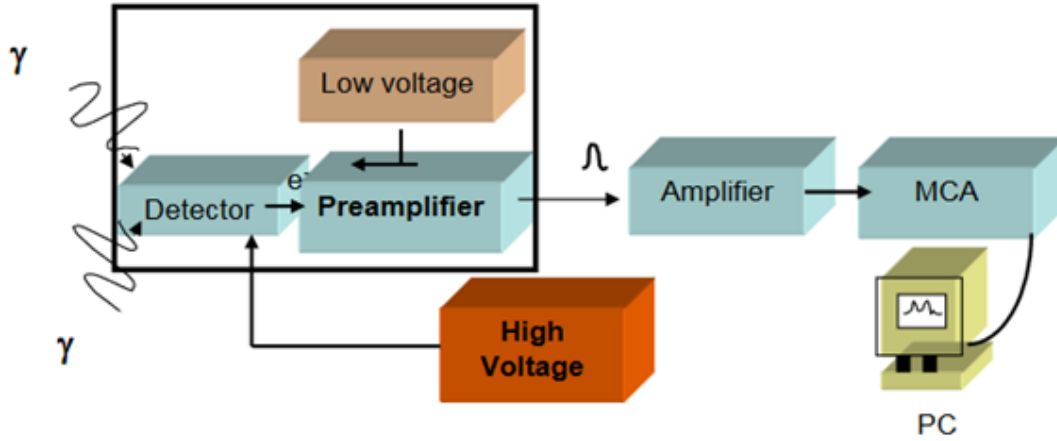


Figure 2.4: Block diagram of a basic gamma spectrometry system [14].

In a semiconductor detector, incoming gamma photons interact with the detector material, initiating a sequence of processes that ultimately lead to the formation of a detectable electrical signal. The photoelectric effect is one such interaction and produces a distinct peak in the recorded spectrum. After this interaction, the ejected photoelectron travels through the HPGe crystal and gradually loses energy through ionisation, excitation, and thermal interactions.

Each collision generates electron-hole pairs within the crystal. This cascade of secondary ionisation leads to an avalanche of free charge carriers. A strong electric field applied across the detector causes the electrons to migrate toward the anode and holes toward the cathode. The movement of these charges induces a current that is proportional to the energy deposited by the gamma photon. This current is converted into a voltage pulse, which is then processed to form a spectrum in which energy peaks can be identified.

At higher gamma energies, specifically those above 1.022 MeV, the photon may interact via pair production, resulting in the creation of an electron-positron pair. If one or both of the resulting annihilation photons escape the detector without further interaction, they give rise to additional features in the energy spectrum: a single escape peak at 0.511 MeV or a double escape peak at 1.022 MeV. If all the energy is deposited within the detector, the full energy of the original gamma photon is recorded as a photopeak [13].

## Electronics of a semiconductor counter

Gamma spectrometry detectors can be broadly classified into two types: scintillation detectors and semiconductor detectors.

Scintillation detectors use materials that emit light upon interaction with gamma rays, with NaI(Tl) (i.e. sodium iodide doped with thallium) being a common example. The energy of the photon is converted into a light pulse, which is detected by a Photomultiplier Tube (PMT) and converted into an electrical signal for further analysis.

In contrast, semiconductor detectors measure an electrical signal proportional to the energy of the incoming gamma ray. When a photon strikes the semiconductor material, it dislodges electrons from their atomic orbitals, creating electron-hole pairs. These charge carriers move under an applied electric field and generate an electrical signal. Common semiconductor detectors include silicon and HPGe detectors; this study focuses on the HPGe detector, while scintillator detectors will not be discussed further [18].

The preamplifier collects the charge generated by the interaction of photons with the detector. It amplifies the weak charge signals and shapes them into a voltage pulse suitable for further processing, with a pulse height proportional to the energy of the detected gamma photon.

The high-voltage power supply provides the necessary voltage to the detector, ensuring the electric field is strong enough to efficiently separate the charge carriers (electrons and holes) and direct them towards the respective electrodes.

The amplifier further processes the signal by increasing the pulse amplitude while minimising distortions from baseline shifts and background noise. The ADC then digitises the amplified signal and transmits it to the MCA, where it is sorted according to pulse height, i.e. to the energy of the detected gamma photon.

The MCA organises and analyses the data from the ADC. It provides real-time feedback, displaying the spectrum and allowing for detailed peak analysis. Digital Signal Processing (DSP) techniques, including DSP filters, can be used instead of traditional analogue amplification to improve signal resolution and accuracy [18].

## HPGe detector

High-Purity Germanium detectors offer superior precision in measuring gamma and X-rays compared to silicon detectors. This is primarily due to the higher atomic number of germanium and the lower average ionisation energy required to create an electron-hole pair (2.9 eV for Ge vs 3.6 eV for Si). As a result, germanium has a higher linear attenuation coefficient for gamma and X-ray radiation, which leads to a shorter mean free path for these types of radiation. Unlike silicon detectors, which are limited to a few millimeters in thickness, germanium detectors can have a sensitive region spanning several centimeters. This difference arises primarily due to the higher atomic number and greater density of germanium compared to silicon. This makes them well-suited for use as total absorption detectors for gamma radiation with energy up to several MeV.

The performance of radiation detectors depends on the purity of the detector materials. In early detectors, germanium crystals doped with lithium (Ge(Li)) were used to create an intrinsic region where electrons and holes could migrate to the electrodes, generating a signal. While the lithium doping compensated for the lack of intrinsic charge carriers, it introduced a significant drawback: lithium atoms acted as trapping centers, reducing charge carrier mobility and degrading the performance of the detector. This problem stemmed from the high impurity concentrations in Ge(Li), which affected charge collection efficiency. Advances in purification techniques have significantly reduced impurity levels in germanium, from  $10^{13}$  atoms/cm<sup>3</sup> in Ge(Li) to  $10^{10}$  atoms/cm<sup>3</sup> in HPGe. This has eliminated the need for lithium doping, significantly improving charge carrier mobility and detector efficiency and resolution.

Semiconductors such as germanium and silicon have a valence band, where electrons are bound to atoms and a conduction band, where electrons move freely, allowing electrical conduction. The energy difference between these energy levels (bandgap) dictates the electrical properties of the semiconductor. When energy is absorbed, electrons transition from the valence band to the conduction band, generating electron-hole pairs that serve as charge carriers.

Doping the semiconductor modifies its electrical properties by introducing impurities that change the balance of charge carriers. In an N-type semiconductor, doping is performed using elements with more valence electrons than the host material, such as phosphorus in silicon. These dopants contribute extra free electrons, making electrons the majority charge carriers. Conversely, a P-type semiconductor is doped with elements that have fewer valence electrons, such as boron. This creates vacancies, or “holes” in the crystal lattice, which act as positive charge carriers. As a result, holes become the majority charge carriers in P-type materials. A P-N junction formed by interfacing these materials generates an electric field that governs charge transport within the device.

An HPGe detector incorporates a P-I-N structure, where the Intrinsic (I) region is the active volume sensitive to ionising radiation. The detector is operated under reverse bias, with a negative voltage applied to the P-side and a positive voltage to the N-side. This bias widens the depletion region, an area depleted of free charge carriers, increasing the active volume available for photon interactions. The width of the depletion region is a key factor in detector performance, as it directly influences charge collection efficiency and spectral resolution. Increasing the applied voltage extends this region further, reduces noise from residual impurities and enhances detector resolution [19].

To achieve optimal performance, HPGe detectors must be cooled to cryogenic temperatures, typically using liquid nitrogen at 77 K (-195.8°C). This cooling is crucial because at room temperature, thermal excitation of electrons across the small bandgap of germanium (0.67 eV) generates undesired charge carriers. These thermally generated carriers increase the reverse leakage current and introduce noise into the signal. Cooling reduces thermal excitation, ensuring that charge carriers are generated predominantly by photon interactions rather than by thermal effects.

To maintain such a low temperature, HPGe detectors are housed within a vacuum-sealed cryostat that thermally insulates them and ensures efficient cooling. The germanium crystal is mounted within a thin metallic holder and enclosed by a 1 mm thick aluminium end cap, which minimises the attenuation of low-energy photons. Radiation enters the detector through this end cap while the crystal remains protected. A key component of the cryostat is the cold finger, a thermally conductive metal rod that transfers heat from the germanium crystal to the liquid nitrogen reservoir. The cold finger extends beyond the vacuum boundary of the cryostat into a Dewar flask, a vacuum-insulated container designed to store cryogenic liquids. By immersing the cold finger in liquid nitrogen, the detector is maintained at a stable low temperature through the slow boiling of nitrogen, which is released as a gas. Depending on the vacuum flask's size and design, this setup can maintain cryogenic temperatures for several hours to weeks before requiring refilling. Additionally, the preamplifier of the detector is integrated within the cryostat to reduce parasitic capacitance, which can store electrical charge and hinder signal processing. Although liquid nitrogen cooling is highly effective, the detector requires several hours of cooling to achieve operational readiness [11].

### 2.1.3 Calibration

Calibration ensures accurate measurements by comparing results with reference samples, i.e. objects made of known materials or standardised substances with known activities. It verifies that equipment operates within set parameters, meets quality standards, correctly identifies radionuclides and determines their activity concentrations. Without regular calibration, reliability may decrease, leading to errors and inefficiencies. The primary types of calibration include energy calibration, efficiency calibration, peak shape calibration, background calibration, and gain stabilisation calibration. The first two types are most important, as they determine the accuracy (closeness to the true value) and precision (consistency of repeated measurements) of the results [14].

#### Energy calibration

Energy calibration verifies that the pulse height scale accurately correlates with the absolute gamma-ray energy, enabling correct peak identification. Well-characterised reference sources with known gamma energies are used to establish the energy scale, allowing additional peaks within this range to be detected. Gamma spectrometry employs different calibration standards depending on the required precision level and energy range. Secondary calibration standards are used for higher-energy gamma radiation, including those relevant to nuclides with high-energy emission. The double escape peak often falls within the calibrated energy range, allowing calibration at higher energies by referencing the corresponding full-energy peak.

However, existing energy calibrations may be inadequate when analysing unknown spectra, particularly if the spectrometer exhibits small non-linearities. Even high-precision spectrometers can deviate slightly from the ideal linear response, usually within one or two channels over a range of a thousand. The accuracy of peak averaging, which involves determining the centroid energy of a peak by averaging counts over its full width, depends on the resolution and stability of the spectrometer. To ensure precise energy assignments, it is crucial to use reliable reference energies. In cases where reference calibration sources are limited, overlapping peaks from known isotopes within the unknown spectrum may be used to extend or refine the calibration across a broader energy range.

A standard source with gamma-ray energies close to those expected in the unknown sample is used to ensure accurate calibration. Multiple calibration peaks are measured over the entire energy range to correct for potential non-linearities. In high-purity germanium systems, the uncertainty in the peak position is around one part in  $10^5$ , which is comparable to the uncertainty in the calibration energy standards. Once the energy points are acquired, the peak energies are plotted against the corresponding channel numbers to create a calibration curve, typically linear, that directly correlates channel number with energy. Regular recalibration is required to compensate for potential detector drift due to time and temperature fluctuations [16].

### Efficiency calibration

In gamma spectrometry, efficiency is defined as the ratio of detected to emitted photons and is essential for accurately quantifying unknown samples. By calibrating with known sources at specific angles and distances, efficiency values are plotted against energy values to generate an efficiency curve. Higher-energy gamma rays exhibit lower detection efficiency due to their increased likelihood of passing through the detector without interacting. The efficiency characteristics of germanium detectors, particularly the differences between n-type and p-type designs, significantly impact measurement accuracy.

The intrinsic peak efficiency of germanium detectors at full energy is shown in figure 2.5 and varies with detector type, photon energy and interaction mechanisms. A key distinction between n-type and p-type high-purity germanium detectors lies in their electrical contact structure, which significantly affects their response to low-energy radiation. In p-type detectors, the outer contact is formed by lithium diffusion and is relatively thick. It creates a “dead layer” near the detector surface that does not contribute to charge collection. As a result, p-type detectors exhibit reduced efficiency for gamma rays below 150 keV, since these photons are more likely to be absorbed in the dead layer before reaching the active volume. Conversely, n-type detectors have a much thinner outer contact, typically produced by ion implantation. This allows better transmission of low-energy photons into the active volume. However, n-type detectors also exhibit a characteristic efficiency notch near 11 keV, which corresponds to the K-shell binding energy of germanium. If the resulting K X-rays escape without depositing their energy, the event does not contribute to the full-energy peak. For energies slightly below 11 keV, L-shell interactions become dominant. These occur deeper within the detector, and the lower-energy L X-rays have a reduced escape probability, increasing the likelihood of full-energy deposition.

Across the energy spectrum, different interaction mechanisms shape the efficiency profile. From a few keV up to 100 keV, photoelectric absorption dominates, resulting in high intrinsic efficiency. Between 100 keV and 1 MeV, Compton scattering becomes significant, allowing some scattered photons to escape and gradually reducing the full-energy peak efficiency. Above 1 MeV, the efficiency drops sharply as photons are increasingly likely to pass through the detector without interacting.

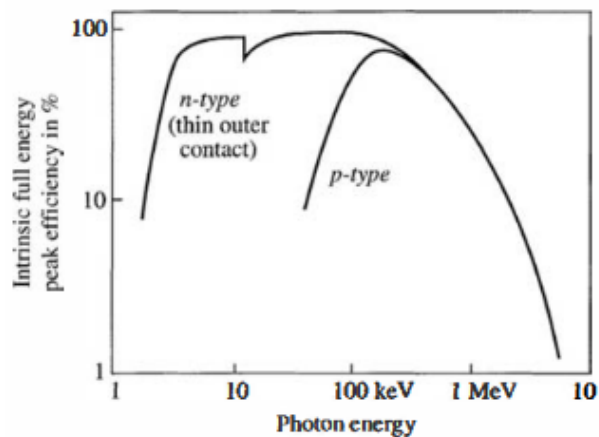


Figure 2.5: Intrinsic full energy peak efficiency for germanium detectors as a function of incident photon energy [16].

By measuring several gamma-ray energies, an empirical efficiency curve is constructed that accounts for detector-specific response variations. With careful calibration, peak detection efficiency can be typically determined within 0.5–2.0% precision. Without direct calibration, similar detectors may show 10–20% uncertainty in efficiency estimates due to differences in active volume, construction tolerances, window thickness, and long-term changes in charge collection. Direct calibration mitigates these uncertainties and is critical for accurately determining the emission rate (the number of gamma photons emitted by the source per unit time). This is calculated by recording the full-energy peak counts over a known time interval, and correcting for the solid angle subtended by the detector and the source-detector geometry [16].

### 2.1.4 Recent developed methods for performing efficiency calibration

In [20], a study investigated the Monte Carlo and experimental efficiency calibration of gamma spectrometers for the non-destructive analysis of large-volume samples with irregular geometries. The Monte Carlo code Geometry and Tracking version 3 (GEANT3) was used to simulate measurement efficiency. Experimental calibration employed radioactive standards mixed with iron-silica-copper powder, prepared in mock-ups that replicated the original sample geometry.

GEANT3, written in FORTRAN, simulates radiation-matter interactions including absorption, scattering, and secondary particle emission. Its ability to model complex geometries makes it well-suited for efficiency calibration of radiation detectors.

The study aimed to evaluate the accuracy of full-energy peak efficiency calibration of HPGe gamma-ray detectors for large-volume samples of irregular shapes, using Monte Carlo simulations validated against experimental measurements. The findings showed that a simple box model overestimated efficiency by approximately 11% relative to experimental data, while a spherical model underestimated it by 10%. These discrepancies, typically on the order of 10%, highlighted the sensitivity of Monte Carlo results to geometrical assumptions. The authors recommended integrating Monte Carlo simulations into routine efficiency calibration of gamma-emitting radionuclides in large and irregular samples [20].

A more recent study, [21], compared efficiency calibration techniques for HPGe detectors for analysing soil samples in Marinelli geometry. This investigation was motivated by the need to calibrate samples with non-standard geometries, addressed using Monte Carlo simulations with Monte Carlo N-Particle Transport version 5 (MCNP5) and Geometry and Tracking version 4 (GEANT4).

MCNP5, developed at Los Alamos National Laboratory, simulates neutron, gamma, electron, and other particle interactions and is renowned for its reliability in radiation shielding and detector calibration applications. GEANT4, developed by CERN in C++, offers advanced support for modelling complex 3D geometries. Considerable discrepancies have been observed between different codes, as well as within the same code depending on cross-section libraries and algorithms. Reported differences between MCNP and GEANT4 are up to 5% for photon transport and 10% for electron transport [22]. Rigorous validation remains essential for these codes.

For this purpose, the study used Almost Native Graphics Layer Engine (ANGLE3) software, which, unlike MCNP5 and GEANT4, is not a Monte Carlo tool but an efficiency transfer method. It mathematically adjusts existing calibration curves to new geometries, enabling efficiency determination without additional source measurements. However, its applicability is limited in highly complex geometries. ANGLE3 calculates detection efficiency using the solid angle method, based on the solid angle subtended by the sample at the detector.

ANGLE3 achieved an average calibration discrepancy of 0.73%, with values as low as 0.65% for energies below 20 keV, and no evidence of systematic bias or systematic error has been reported [23]. Although it does not require additional standards, it relies on a reference efficiency curve obtained using a calibrated source in a known geometry. Calculating detection efficiency requires knowledge of the reference efficiency curve, the geometrical parameters of both the sample and detector, and the gamma-ray attenuation coefficients of all materials involved.

The average efficiency ratio of MCNP5 relative to experimental measurements was 0.97, with a relative standard deviation of 5% (relative to the mean). For GEANT4, the ratio was 0.99 with a 4% relative standard deviation. Relative to ANGLE3, MCNP5 averaged 0.95 (5% relative standard deviation), and GEANT4 to ANGLE3 averaged 1.04 (11% relative standard deviation).

The results indicate good agreement between Marinelli efficiencies obtained using MCNP5, GEANT4 and ANGLE3 [21].



## 2.2 Envelope geometry

The envelope method is an advanced approach to efficiency calibration in gamma spectrometry that simplifies complex sample geometries by approximating them with standard shapes such as cylinders or spheres. Developed in recent decades, it addresses the challenges posed by varying sample geometries, which traditionally complicate accurate activity measurements. Rather than calibrating each sample individually, the method establishes a generalised efficiency curve that accounts for geometric differences, significantly reducing calibration time and cost. It also enhances workplace safety by minimising the use of radioactive reference sources and the associated exposure. By matching the geometry of a sample to the closest available standard, the method allows efficient activity determination without requiring exact geometric replication. Although this approximation introduces uncertainty, it streamlines the measurement process and maintains sufficient accuracy for many practical applications [5].

Mirion Technologies has developed ISOCS (In Situ Object Counting System) and LabSOCS (Laboratory Sourceless Calibration Software) to implement the envelope method in gamma spectrometry. These tools use Monte Carlo simulations and advanced algorithms to estimate detection efficiency without the need of physical calibration sources [24]. By simulating a wide range of geometries, the software generates efficiency curves that form an “envelope”, representing the upper and lower limits of possible efficiency values. For samples with unknown or irregular shapes, the efficiency can be estimated by interpolation or extrapolation within this envelope [5].

The importance of geometric modelling in efficiency calibration is evident when calculating the activity of a radionuclide that emits photons at a single energy:

$$A = \frac{N_s(E)}{\varepsilon(E) \cdot \Delta t} \times \frac{1}{I_\gamma(E)} \quad (2.13)$$

where:

- A is the activity of the radionuclide;
- $N_s(E)$  is the net peak area corresponding to energy E;
- $\varepsilon(E)$  is the absolute full-energy peak efficiency corresponding to the geometric model at energy E;
- $I_\gamma(E)$  is the emission intensity of photons with energy E;
- $\Delta t$  is the live time of spectrum acquisition.

$\varepsilon$  in equation 2.13 highlights how activity determination relies on efficiency calibration, which depends on the geometry of the source. The envelope method provides reliable estimates of activity by accounting for variations in efficiency across different geometries [5].

Although the envelope method represents a significant improvement over traditional calibration techniques, some uncertainties remain. These arise from counting statistics, dead time corrections, systematic uncertainties, gamma emission probabilities, and geometric modelling. ISOCS/LabSOCS also introduces its own sources of uncertainty, including detector validation, which ensures the radiation detector is accurately calibrated and functions reliably under various conditions to provide precise measurements. Addressing these uncertainties requires continuous efforts to better quantify and reduce them, through improvements in both the computational models and experimental validation of the envelope method [7].

### 2.2.1 ISOCS/LabSOCS

The ISOCS/LabSOCS software provides comprehensive geometry modelling templates for gamma spectrometry. ISOCS is used for in-situ measurements in field environments such as decontamination or decommissioning, whereas LabSOCS is intended for laboratory-based detector calibration. The software is approved for Non-Destructive Assay (NDA) techniques by key regulatory bodies, including the U.S. Nuclear Regulatory Commission (NRC) under Regulatory Guide 1.21, which governs the monitoring of radioactive effluents, and ASTM International Committee C26.10, which sets standards for nuclear fuel cycle applications. Traceability to calibration sources certified by the National Institute of Standards and Technology (NIST) and the German Accreditation Body (DAKKS) is ensured through detailed factory characterisation of detectors [24].

This software eliminates the need for traditional efficiency calibration in a laboratory environment by enabling off-site calibration based on predefined sample geometries. While measurement setups can be prepared and evaluated externally, the actual activity measurement must still be performed on-site. As a result, fieldwork is significantly reduced, with on-site operations limited to system setup and sample collection, even when dealing with complex or varied geometries.

The efficiency of ISOCS/LabSOCS stems from two key factors. First, Mirion Technologies characterises the energy, efficiency, and spatial response of the detector using the MCNP code. Second, the software includes mathematical templates for standard sample geometries such as flat surfaces, rectangular boxes, vessels, pipes, and beakers. Users can modify these templates through input parameters, including sample size, mass, density, and distance from the detector. The software then generates a customised efficiency calibration tailored to the measurement configuration, performing all necessary calculations and visualisations within the software environment [24].

## Working mechanism

The calibration process with ISOCS/LabSOCS follows a structured sequence that begins with the Data Quality Objective (DQO) process, determining the required measurement sensitivity and accuracy. Simultaneously, the ISOCS Uncertainty Estimator (IUE) helps define the optimal measurement strategy by assessing potential uncertainties. Once the measurement strategy is established, a characterised detector acquires counts from the sample. The appropriate geometry template is then selected based on the characteristics of the sample. Critical physical parameters, including sample dimensions, density, and distance from the detector, are entered into the software at this stage. The generated calibration is applied to the measured gamma spectrum. The complete calibration process typically takes approximately fifteen seconds.

Both ISOCS and LabSOCS offer a diverse range of geometry templates to accommodate various sample types. ISOCS includes 21 fundamental templates, covering a broad range of geometries such as simple and complex boxes and cylinders, Marinelli beaker holes, pipes, tubes, tanks, and contamination scenarios involving structural components (e.g. beams, channels, corners), as well as entire rooms and containers. Figure 2.6 illustrates an example of an ISOCS calibration template for simple and complex box geometries. LabSOCS provides ten basic and two advanced templates that allow for the import of user-defined contours. These templates include general Marinelli cups, customisable Marinelli beakers, cylinders, disks, point sources, and simplified geometric shapes such as spheres, boxes, and cups.

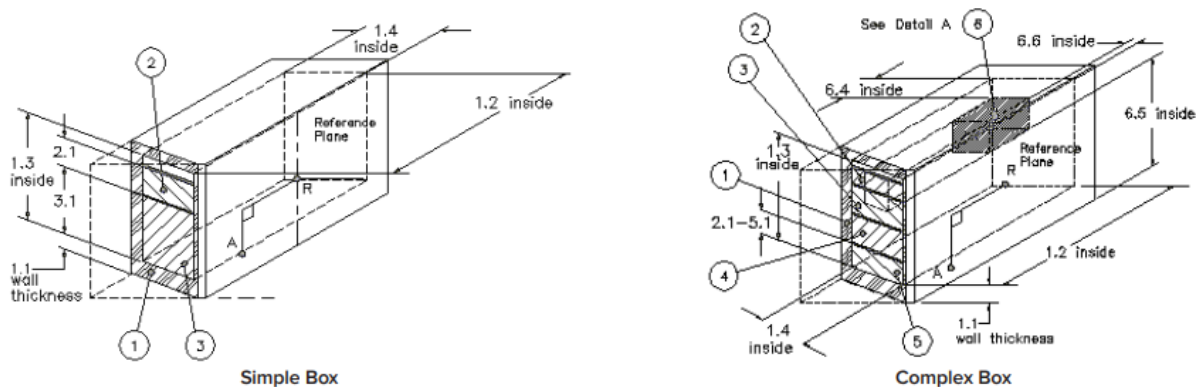


Figure 2.6: ISOCS calibration template [24].

## Software components

Once the material properties are defined using the Mu Library [25], the software provides an interactive 3D graphical interface that visualises all geometry components, including the detector, sample container, and collimator. The modelling and verification processes are streamlined through features such as a 360-degree rotating view and an object tree, allowing users to select and modify individual elements quickly.

For collimation, the software includes a predefined library of collimators and options for customisation by specifying dimensions and materials. It supports two basic collimator templates and five advanced templates, enabling the design of complex collimators, including internal liners and back shielding. This ensures flexibility in optimising measurement setups. Figure 2.7 illustrates an example of the software in operation, demonstrating its 3D visualisation capabilities.

The ISOCS system comprises several components for portable and in situ gamma spectrometry applications. These include an ISOCS-characterised HPGe detector, a portable shielding and collimator mounted on a trolley, an InSpector 2000 portable spectroscopy workstation, a laptop PC equipped with Genie 2000 software, and the ISOCS software. These components work together to provide an efficient, flexible, and highly accurate gamma spectrometry system suitable for field and laboratory use [24].

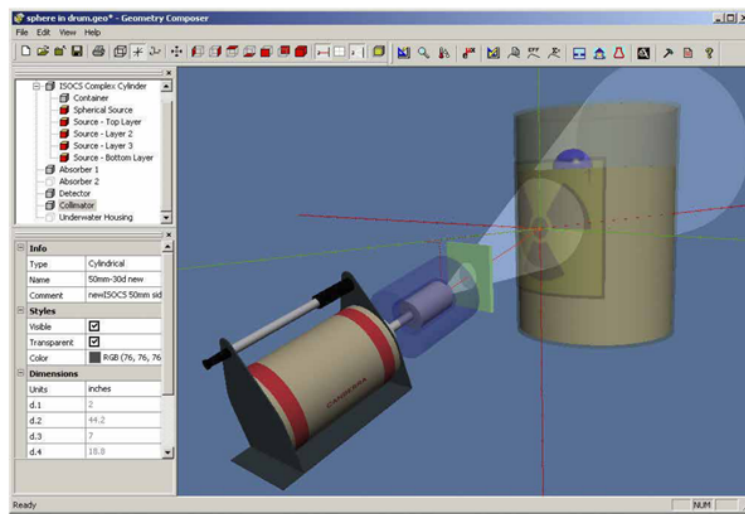


Figure 2.7: The geometry template window in ISOCS software [24].

### 2.2.2 Previous similar research on ISOCS/LabSOCS software

Mirion Technologies conducted a study to quantify a typical level of bias related to detector dimensions in the ISOCS/LabSOCS software. For this purpose, several LabSOCS detector efficiency curves were generated for a 44% Standard Electrode Coaxial Germanium (SEGe) detector, with the crystal dimensions varied within typical manufacturing tolerances. The crystal specifications and associated uncertainties were as follows: crystal diameter of  $60 \pm 2$  mm, crystal length of  $60 \pm 2$  mm, and lithium layer thickness of  $0.50 \pm 0.05$  mm. Measurements were performed to determine the uncertainty in efficiency caused by these dimensional variations, and they were evaluated across various gamma-ray energies. Manufacturing tolerances introduced uncertainties of 8–10% in the detector response efficiency within the 100–400 keV energy range. For energies below 100 keV, larger deviations were observed ( $\pm 15\%$  for the Am-241 emission energy at 60 keV). These values do not account for other factors affecting detector efficiency, such as the depth and diameter of the germanium well and the crystal bevel [26].

A study was conducted to validate the ISOCS mathematical efficiency calibration software by assessing the accuracy of the calibration method through 109 individual tests. These validation tests were grouped into three categories based on counting geometry: field, laboratory, and collimated. In each case, the efficiency value obtained by the ISOCS efficiency calibration for a given geometry was compared to an efficiency value obtained by a reference calibration. The reference efficiency values were obtained either through Monte Carlo simulations using the MCNP code or from measurements with a multi-energy source.

Table 2.1 presents the results of the validation tests for laboratory geometries. In each test, the data were divided into three energy groups:  $< 150$  keV,  $> 150$  keV, and all energies combined. For each group, a weighted average of the ratio between the ISOCS and reference efficiencies was calculated, along with the corresponding weighted standard deviation. Both the ratio and the standard deviation were weighted using the inverse of the absolute uncertainties in the reference efficiencies. The individual uncertainty ( $1\sigma$  standard deviation) values for each test were also averaged to estimate the expected standard deviation. If the observed standard deviation from the combined ISOCS/reference ratios closely matches the expected value, the distribution of the data approximates a Gaussian distribution.

Table 2.1: Summary of ISOCS validation results for laboratory geometries across energy ranges [27].

| <b>Result</b>                                    | <b>Data <math>&lt; 150</math><br/>keV</b> | <b>Data <math>&gt; 150</math><br/>keV</b> | <b>All data<br/>combined</b> |
|--|---|---|------------------------------|
| Weighted average of<br>ISOCS/reference ratio [-] | 1.05                                      | 1.02                                      | 0.97                         |
| Uncertainty in weighted<br>mean [%]              | 0.05                                      | 0.19                                      | 0.77                         |
| Standard deviation of data<br>[%]                | 12.8                                      | 9.9                                       | 9.6                          |
| Expected standard<br>deviation [%]               | 8.0                                       | 5.1                                       | 6.8                          |
| Average ISOCS standard<br>deviation [%]          | 6.7                                       | 4.5                                       | 5.4                          |

Previous validation studies using total photon cross-sections yielded underestimated ISOCS efficiencies. The current version of ISOCS no longer includes coherent scattering in the cross-section data, resulting in slightly higher but more accurate efficiency values.

In conclusion, for field and laboratory counting geometries, the average ISOCS-to-reference efficiency ratios were  $1.01 \pm 0.007$  and  $0.97 \pm 0.007$ , respectively. For collimated geometries, the average ratio was  $1.09 \pm 0.014$  [27].

In 2003, Canberra Industries conducted a validation study to evaluate potential bias introduced by the LabSOCS mathematical efficiency calibration software. The objective was to verify the reliability of the software by comparing LabSOCS-derived activity values against the certified activities of NIST-traceable point sources.

For laboratory geometries, 53 validation tests were carried out, 52 of which employed NIST-certified radioactive sources as the reference standard. Each LabSOCS-calculated efficiency was compared to the reference value, and its individual contribution to the total measurement uncertainty was isolated by subtracting the variance contributions from counting statistics and source activity uncertainty. The results showed standard deviations of 7.1% for energies below 150 keV, 6.0% for the 150–400 keV range, and 4.3% for the 400–7000 keV range.

As part of the ISOXVRFY process, four NIST-standard sources with 13 distinct gamma lines were measured in seven laboratory-representative geometries. Each spectrum was analysed as an “unknown”, and the reported activity for each of the 13 energy lines was compared against the certified activity provided in the source documentation. Table 2.2 presents sample results for two relevant energy lines from one of the seven geometries. In addition, Table 2.3 summarises the accuracy and precision data obtained from the first 13 ISOXVRFY detectors tested.

Table 2.2: Results from analysing reference source as unknown for Co-60 [28].

| Nuclide | Energy [keV] | Ratio<br>measured/true<br>activity [-] | Relative<br>uncertainty ( $1\sigma$ )<br>[%] |
|---------|--------------|--|--|
| Co-60   | 1173         | 0.94                                   | 1.53   |
| Co-60   | 1332         | 0.92                                   | 1.65   |

Table 2.3: Summary of accuracy and precision from first 13 ISOXVRFY detectors [28].

| Metric                                | < 150 keV | 150–400<br>keV | > 400 keV |
|---------------------------------------|-----------|----------------|-----------|
| Average bias [%]                      | 1.0       | 1.9            | -1.9      |
| Average  bias  [%]                    | 5.5       | 5.7            | 4.6       |
| $\sigma$ from ISOXVRFY [%]            | 5.1       | 5.1            | 4.2       |
| $\sigma$ from validation study<br>[%] | 7.1       | 6.0            | 4.3       |

The results demonstrate that LabSOCS mathematical efficiency calibrations yield accurate activity measurements within 4–5% for photon energies above 400 keV. However, larger errors, typically 10%, and up to 20–30% for large-volume detectors, can occur if sources exhibiting cascade summing effects (such as Y-88, Ce-139, Co-60 or Eu-152) are used without correction.

Under normal conditions, source-based efficiency calibrations produce a total uncertainty of approximately 3–5%, arising from the combined effects of source uncertainty, counting statistics, and fitting error. In this context, the 4–5% standard deviation achieved by the LabSOCS method is considered acceptable for most laboratory sample assay applications, especially given its practical advantages in speed and ease of use over conventional source-based calibrations [28].

Another study [29] investigated the performance of various efficiency calibration methods for potential application in HPGe gamma-ray spectrometry. The primary aim was to assess the accuracy and reliability of these calibration methods through an interlaboratory comparison exercise involving ten independent laboratories. Participants were required to determine the activity concentration of a certified multi-gamma radionuclide solution with a known reference activity.

The test sample comprised multiple radionuclides, including Co-60, Am-241, Ra-226, Th-232, Cs-137, and K-40, contained in a 250 ml polyethylene bottle, representing a standard measurement geometry. The China Institute of Atomic Energy (CIAE) provided the certified reference activity values.

Two efficiency calibration methods were evaluated: the mathematical modelling-based LabSOCS software and the ANGLE3 approach. Measurements were performed using two HPGe detectors: a broad-energy coaxial detector (Canberra) and a Detective DX-100T detector (ORTEC). The activity concentrations determined for Co-60 using each calibration method are presented in table 2.4. The expanded uncertainty was calculated as:

$$U_{\text{total}} = k \sqrt{U_1^2 + U_2^2 + U_3^2 + U_4^2} \quad (2.14)$$

where:

- $k$  is the coverage factor, set to 2;
- $U_1$  represents the uncertainty associated with the efficiency calibration of the HPGe detector, estimated from the fitted efficiency curve provided by the commercial software;
- $U_2$  corresponds to the uncertainty due to statistical counting;
- $U_3$  reflects the uncertainty in the sample weights;
- $U_4$  accounts for the uncertainty related to the sample geometry.

Table 2.4: Comparison of activity concentration results using different efficiency calibration methods [29].

| Efficiency calibration method | Activity concentration [Bq/kg] $\pm$ expanded uncertainty (k=2) |
|-------------------------------|---|
| Reference value               | $331 \pm 10$  |
| LabSOCS                       | $314 \pm 24$  |
| ANGLE3                        | $308 \pm 24$  |

The performance of the calibration methods was assessed based on relative bias and Z-scores, with trueness and precision serving as the primary evaluation criteria. The relative bias was calculated using the following equation:

$$\text{Relative bias} = \frac{\text{value}_{\text{analyst}} - \text{value}_{\text{ref}}}{\text{value}_{\text{ref}}} \times 100\% \quad (2.15)$$

where  $\text{value}_{\text{analyst}}$  is the measured activity concentration and  $\text{value}_{\text{ref}}$  is the certified reference activity concentration.

The Z-score was assessed according to the evaluation criteria established by the IAEA [30]. Performance is considered satisfactory when the absolute value of the Z-score is less than 2. If the Z-score lies between 2 and 3 in absolute terms, the performance is considered questionable, and a Z-score greater than 3 indicates unsatisfactory performance.

Trueness was evaluated using the following expressions:

$$A_1 = |\text{value}_{\text{ref}} - \text{value}_{\text{analyst}}| \quad (2.16)$$

$$A_2 = 2.58 \times \sqrt{U_{\text{ref}}^2 + U_{\text{analyst}}^2} \quad (2.17)$$

where  $U_{\text{ref}}$  represents the certified reference uncertainty and  $U_{\text{analyst}}$  denotes the expanded uncertainty associated with the measurement. The result was considered acceptable when  $A_1 \leq A_2$ .

Precision was quantified using the P-index, calculated as:

$$P = \sqrt{\left(\frac{U_{\text{ref}}}{\text{value}_{\text{ref}}}\right)^2 + \left(\frac{U_{\text{analyst}}}{\text{value}_{\text{analyst}}}\right)^2} \times 100\% \quad (2.18)$$

where precision results were considered acceptable if the P-index did not exceed 10%.



Table 2.5 summarises the relative bias and Z-scores obtained for Co-60. The results indicate a slight underestimation for Co-60; however, the relative bias remains within the 15% acceptance threshold and is therefore deemed acceptable. The Z-score also remains below 2, suggesting satisfactory performance. Furthermore, both the trueness and precision values for Co-60 meet the defined acceptance criteria.

The largest discrepancies were observed for Am-241. The LabSOCS method produced a relative bias of 25.81%, while ANGLE3 showed a relative bias of -14.31%. Despite these large biases, both trueness and precision assessments remained within acceptable limits. The substantial relative bias for Am-241 is primarily attributed to the challenges inherent in low-energy gamma-ray detection, including increased sensitivity to sample geometry and self-absorption effects.

Table 2.5: Relative bias and Z-score for different efficiency calibration methods [29].

| Efficiency calibration method | Relative bias [%] | Z-score |
|-------------------------------|-------------------|---------|
| LabSOCS                       | -5.28             | -0.53   |
| ANGLE3                        | -6.83             | -0.68   |

Overall, the study demonstrated that both LabSOCS and ANGLE3 provide sufficiently accurate estimations of activity concentration. The relative biases observed for Co-60 were within acceptable limits, highlighting the reliability of these software-based calibration approaches for gamma-ray spectrometry [29].

### 2.2.3 Uncertainty

Gamma spectrometry requires careful uncertainty evaluation to ensure accurate activity measurements and to minimise measurement errors. Among the various sources of uncertainty, efficiency calibration typically contributes the largest share, particularly with complex sample geometries and low-energy gamma-ray analysis. Key contributors to overall uncertainty include counting statistics, live-time correction, systematic uncertainties in peak fitting, gamma emission probability errors, and geometric model inaccuracies. In ISOCS/LabSOCS-based gamma spectrometry, uncertainties arise from numerical methods involved in yield calculation, peak area determination, emission intensities, activity distribution, material composition and geometric parameters such as source-to-detector distance, and sample characteristics including sample size, mass and density. Since these parameters are often only approximately known, deviations can propagate to efficiency calibration, directly affecting the final activity values. To address these challenges, tools like IUE and GURU (Geometry Uncertainty Reduction Utility) have been developed to assess and reduce uncertainties [5], [7].

Mirion Technologies (Canberra) developed the IUE to assess the influence of geometric model parameters on efficiency calibration. Building upon the standard ISOCS software, IUE first calculates a sample's reference efficiency, which includes the baseline ISOCS calibration uncertainty, typically within the range 4 to 8% [31]. This baseline assumes a perfect representation of the sample geometry. The IUE method initially introduces stochastic perturbations to all parameters to identify the most influential ones. It simulates the impact of uncertainties in factors like sample dimensions and material composition, generating multiple efficiency models. These models are generated by sampling parameter values from predefined probability distributions. After validation, the models compute detection efficiency at various energies. The standard deviation at each energy point reflects the combined effects of all uncertain parameters [5], [26].

Recently, CERN developed the GURU tool to correct and quantify the impact of geometric uncertainties on efficiency calibration and, consequently, on specific activity estimates. The GURU tool addresses uncertainties by recalculating the spatial distribution of activity, identifying hotspots based on multiple gamma spectroscopic measurements, and refining activity estimations through multiple gamma spectroscopies of the material. It associates model parameters with corresponding efficiency values and, by optimising the efficiency curve based on the recalculated source distribution, identifies the most representative model. The development of GURU was triggered by a study that identified a 25% systematic bias in activity measurements when a uniform source distribution was assumed, resulting in a systematic underestimation of activity. Furthermore, the study revealed that the standard deviation of the mean activity values between two detector measurements was initially 68%. Following GURU optimisation, this value was reduced to 9% [7].

## 2.3 Statistical techniques

Statistical methods are mathematical techniques used to collect, analyse, and interpret data in a structured and meaningful way. They enable researchers to uncover patterns, assess uncertainty, and draw valid conclusions from complex datasets. By supporting evidence-based reasoning and ensuring consistency in data interpretation, statistical analysis plays a vital role in scientific research. It provides the foundation for evaluating the reliability of experimental results and underpins objective decision-making in the presence of variability.

Statistical methods can be broadly classified into descriptive and inferential statistics. Descriptive statistics are used to summarise samples and measurements, providing an overview of the fundamental characteristics of a dataset. Inferential statistics, on the other hand, enable predictions and generalisations based on sample data. This includes hypothesis testing and investigating relationships between variables [32].

### 2.3.1 Hypothesis testing

Hypothesis testing is a method used to assess whether the observed data provide sufficient evidence to reject a default assumption (the null hypothesis) in favour of an alternative hypothesis. It quantifies the probability of observing a given outcome (or something more extreme), assuming the null hypothesis is true. This enables the determination of whether the results reflect an actual effect or are likely due to random variability.

The hypothesis testing process generally follows four main steps:

#### Step 1: Define the hypotheses

This step involves defining the null hypothesis ( $H_0$ ) and the alternative hypothesis ( $H_a$ ). The null hypothesis represents the status quo or a statement of no effect or difference. In contrast, the alternative hypothesis reflects an impact, difference, or relationship that the study aims to detect. The hypotheses should be clearly defined based on the research question and should reflect the direction of the expected outcome.

#### Step 2: Set the significance level

In this step, the significance level, denoted as alpha ( $\alpha$ ), is specified. This value represents the probability of committing a Type I error, i.e. incorrectly rejecting a true null hypothesis. Commonly used alpha levels are 0.10, 0.05, and 0.01, corresponding to confidence levels of 90%, 95%, and 99%, respectively. The Type II error ( $\beta$ ) is the probability of failing to reject a false null hypothesis. The power of the test, defined as  $1 - \beta$ , indicates the probability of correctly rejecting a false null hypothesis. Setting an appropriate alpha level establishes the false-positive tolerance and affects the sensitivity and specificity of the test.

### Step 3: Choose and apply a statistical test

This step involves selecting a statistical test based on the data and experimental design. The test produces a statistic used to determine if the observed data provide enough evidence to reject the null hypothesis. The decision is made by comparing the test statistic to a critical value or by calculating the p-value. The p-value indicates the probability of obtaining a result as extreme as the observed one, assuming the null hypothesis is true. If the p-value is less than or equal to the significance level, the null hypothesis is rejected in favour of the alternative.

The type of hypothesis test affects interpretation. In a one-tailed test, the rejection region lies in only one tail of the distribution, used when the hypothesis predicts a specific direction. A right-tailed test is applied when the alternative hypothesis states a parameter is greater than a value ( $H_0 : \mu \leq \mu_0$ ,  $H_a : \mu > \mu_0$ ), as shown in figure 2.8(a). A left-tailed test is used when the alternative suggests the parameter is less than a value ( $H_0 : \mu \geq \mu_0$ ,  $H_a : \mu < \mu_0$ ), illustrated in figure 2.8(b).

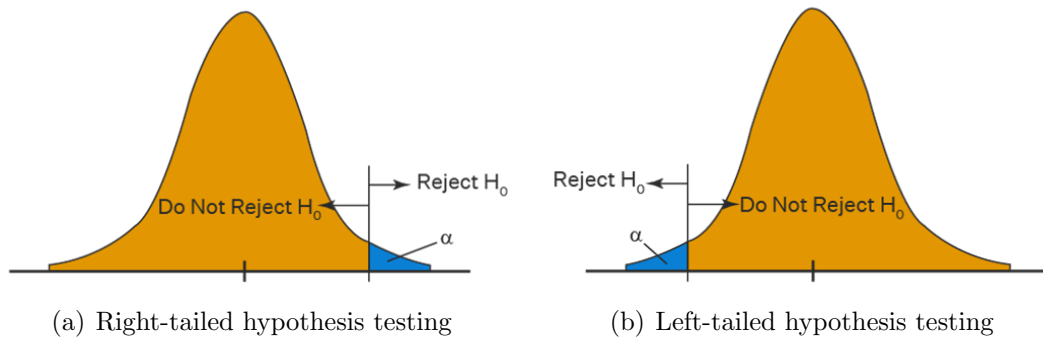


Figure 2.8: One tail hypothesis testing [33].

In a two-tailed hypothesis test, the critical regions lie on both sides of the sampling distribution. This test checks if the population parameter is different (in either direction) from a specified value. In this case, the null hypothesis is  $H_0 : \mu = \mu_0$ , and the alternative hypothesis is  $H_a : \mu \neq \mu_0$ , shown in figure 2.9.

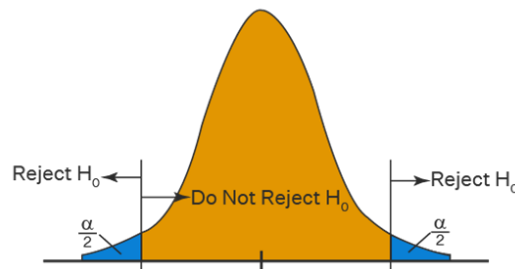


Figure 2.9: Two tail hypothesis testing [33].

### Step 4: interpret the results

The final step is to make a decision regarding the null hypothesis. This is typically done by comparing the  $\alpha$  level to the p-value: the null hypothesis is rejected if  $p \leq \alpha$ . Based on this, a conclusion can be drawn regarding the presence or absence of a statistically significant effect [9], [33].

### 2.3.2 Kullback-Leibler divergence

Kullback–Leibler (KL) divergence, also known as relative entropy, is a statistical measure that quantifies the dissimilarity between two probability distributions defined over the same random variable. Denoted as  $D_{\text{KL}}(P \parallel Q)$ , KL divergence is a type of statistical distance. It quantifies how different a model distribution  $Q$  is from a true distribution  $P$ . Probability distributions are generally classified into two types: discrete and continuous [34].

For discrete probability distributions, the relative entropy from  $Q$  to  $P$  is defined over the same sample space  $X$  as:

$$D_{\text{KL}}(P \parallel Q) = \sum_{x \in X} P(x) \log \left( \frac{P(x)}{Q(x)} \right). \quad (2.19)$$

For continuous probability distributions, it is defined as:

$$D_{\text{KL}}(P \parallel Q) = \int_{-\infty}^{\infty} p(x) \log \left( \frac{p(x)}{q(x)} \right) dx \quad (2.20)$$

where  $p(x)$  and  $q(x)$  are the probability density functions of  $P$  and  $Q$ , respectively.

KL divergence is defined only if, for all  $x$ ,  $Q(x) = 0$  implies  $P(x) = 0$ ; this requirement is known as absolute continuity. If this condition is violated, the divergence is typically defined to be  $+\infty$ . An infinite value may also occur even when  $Q(x) \neq 0$  for all  $x$ , particularly if the domain  $X$  is infinite, since in such cases the sum or integral that defines the KL divergence may fail to converge. If  $q(x) = 0$  for any  $x$  where  $p(x) \neq 0$ , the logarithmic term becomes undefined. It is therefore essential that  $q(x)$  is strictly positive wherever  $p(x)$  is non-zero.

Whenever  $P(x) = 0$ , the corresponding term in the summation or integral is interpreted as zero, following the limit:

$$\lim_{a \rightarrow 0^+} a \log \left( \frac{a}{b} \right) = 0. \quad (2.21)$$

Although KL divergence measures the difference between two distributions and is a form of distance, it is not a true metric because it does not satisfy symmetry (i.e.  $D_{\text{KL}}(P \parallel Q) \neq D_{\text{KL}}(Q \parallel P)$ ). In the context of information geometry, KL divergence is a type of divergence that generalises squared Euclidean distance and captures directional dissimilarity.

An interpretation of the KL divergence of  $P$  from  $Q$  is that it represents the expected excess surprise incurred when using  $Q$  to approximate  $P$ . KL divergence is always non-negative and equals zero if and only if the two distributions are identical [35].

Data analysts often use the discrete KL divergence for model monitoring by binning continuous data, as it is computationally simpler. Under suitable conditions, the discrete and continuous forms converge as sample size grows and bin width shrinks [36].

### 2.3.3 Bootstrap method

The bootstrap method is a statistical technique used to estimate a population parameter by computing the average of estimates from multiple resamples of an original sample. A key feature of this technique is that observations are drawn one at a time from the original dataset with replacement, i.e. each observation is returned to the dataset before the next draw. As a result, a given observation may appear multiple times in a particular resample.

In this method, a sample of size  $n$  is drawn from the population, referred to as  $S$ . Rather than analytically deriving the sampling distribution of a statistic, the bootstrap approximates it by resampling from  $S$  with replacement  $m$  times, with each bootstrap sample containing  $n$  observations. Provided that  $S$  is representative of the population, resampling  $S$   $m$  times with replacement approximates drawing  $m$  independent samples from the population itself. The resulting estimates approximate the sampling distribution of the statistic under the traditional approach.

The procedure to generate a bootstrap sample is as follows: first, a sample size  $n$  is chosen, typically equal to the original sample size. Then,  $n$  observations are drawn with replacement from the original dataset to create one bootstrap sample. This process is repeated  $m$  times to generate  $m$  bootstrap samples. For each of them, a statistic of interest (e.g. mean or variance) is computed. The collection of these statistics forms the bootstrap distribution, and their mean is often used to estimate the population parameter.

The information content of the data depends on the sample size  $n$ , which remains fixed for each resample. Therefore, the amount of information content does not increase with the iterations. However, a larger  $m$  improves the precision and stability of the bootstrap estimate, although the marginal gain in accuracy diminishes as  $m$  increases.

The bootstrap method offers several advantages:

- It makes minimal assumptions about the underlying distribution of the data, making it suitable for complex or unknown distributions.
- It is applicable to various types of data: continuous, discrete, or categorical.
- It can be used to estimate many types of statistics (e.g. means, medians, variances).
- For small samples, it can yield more reliable estimates by simulating multiple realizations from limited data.

A primary disadvantage of this technique is its computational cost: accurate estimation often requires thousands of resamples (e.g. 1,000–10,000), which may demand relevant computing resources and time [37].



# Chapter 3

## Materials and methodology

Chapter 3 provides a detailed explanation of the materials used in this study. The aim is to establish a database containing raw data, which will later serve as the basis for statistical testing. As the study involves a statistical evaluation of efficiency calibration in relation to geometry, it is essential to include samples of various shapes and dimensions. These samples are measured by CERN using the envelope method and are subsequently sent to an external laboratory, Jacobs, which also performs activity measurements and serves as a reference.

To build a comprehensive database, measurements were conducted over the period 2019–2023, enabling robust benchmarking of the dataset.

Another objective of this chapter is to describe and apply various statistical tests to evaluate the activity measurements conducted by CERN against those performed by Jacobs. The methodology is divided into two main parts. The first involves a comparison of methods, in which hypothesis testing is performed to determine whether there is a statistically significant difference, at a 95% confidence level, between the measurement techniques of CERN and Jacobs. The second focuses on estimating the measurement deviations introduced by the envelope method within the CERN measurements. This includes quantifying the error, uncertainty, and bias.



## 3.1 Materials

### 3.1.1 R programming language

R is a programming language designed by John Chambers and colleagues at Bell Laboratories in the 1970s for statistical calculations, graphics, and interactive statistical programming. It provides a comprehensive set of statistical techniques, including linear and non-linear modelling, classical hypothesis testing, time series analysis, classification and clustering. The strength of this language lies in generating high-quality graphical output, including mathematical symbols and formulas. R has a structured design, which promotes consistency and flexibility in data analysis.

In this research, the development environment RStudio was used, also due to its widespread use in the radiological characterisation team at CERN, ensuring compatibility and seamless integration with existing code [38].

### 3.1.2 Compiled database used for this study

A database was established to support this study, aiming to include samples that had been measured by both CERN and Jacobs. Initially, an Excel list containing only sample ID numbers was provided, but the corresponding measurement data had not yet been compiled into a structured database.

At CERN, samples are analysed using gamma spectrometry with efficiency calibration performed via the envelope method. The collected data is stored in the Traceability of Radioactive Equipment at CERN (TREC). TREC is an application that supports various processes, such as requesting, performing, and managing measurements. It also handles the declaration, transportation, packaging, storage, and processing of potentially radioactive equipment [39]. Each recorded sample is associated with an equipment ID. The corresponding analysis report is available in both TXT and PDF formats and contains essential details such as:

- sample material,
- mass,
- activity reporting date,
- interference-corrected report, which includes the identified radionuclides alongside their activities (uncertainty reported at two sigma, i.e. 95.45% confidence level) and their Minimum Detectable Activity (MDA).

Only the interference-corrected report is considered for this study, while the nuclide identification report and MDA report are excluded. The MDA is the lowest level of radioactivity that a measurement system can reliably detect under specific conditions. As an example, a gamma spectrometry report can be seen in annex A.

An R script was developed to extract relevant data from all available files provided by CERN and Jacobs and merge them into a single dataset. This dataset contains sample ID, measurement data, sample mass, identified nuclides, activity values, associated uncertainties and MDA. With the sample ID, CERN and Jacobs measurement data were linked. Since the measurements were made on different dates, all activity values were corrected for decay to ensure consistency.

The final database consists of 155 samples, each with several radionuclides detected. The most commonly detected nuclides were 134 samples of Co-60 and 44 samples of Ti-44. Figure 3.1 presents a section of the database processed in R, where activity\_c.bq.g represents the activity measured by CERN in Bq/g and activity\_j.bq.g represents the activity measured by Jacobs in Bq/g. In the rest of the thesis, CERN will be referred to as abbreviation C and Jacobs as J.

|    | date       | sample_id   | nuclide | halflife_d          | mass_g | activity_c.bq.g | plusminus_1 | uncertainty_c.bq.g | activity_j.bq.g | plusminus_2 | uncertainty_j.bq.g |
|----|------------|-------------|---------|---------------------|--------|-----------------|-------------|--------------------|-----------------|-------------|--------------------|
| 1  | 29/11/2020 | PSAM-011120 | Co-60   | 1924.8674999999998  | 73.0   | 1.103566e+04    | ±           | 4.224359e+02       | 1.003e+04       | ±           | 4.3e+02            |
| 2  | 13/01/2021 | PSAM-005275 | Na-22   | 949.65              | 125.0  | 4.095398e+01    | ±           | 1.101094e+01       | 2.780e+01       | ±           | 2.2e+00            |
| 3  | 13/01/2021 | PSAM-005275 | Sc-44   | 0.16841666666666666 | 125.0  | 1.127348e-185   | ±           | 1.433363e-186      | 4.430e+02       | ±           | 2.0e+01            |
| 4  | 13/01/2021 | PSAM-005275 | Ti-44   | 21586.275000000001  | 125.0  | 4.775565e+02    | ±           | 5.731870e+01       | 4.580e+02       | ±           | 6.5e+01            |
| 5  | 13/01/2021 | PSAM-005275 | Co-60   | 1924.8674999999998  | 125.0  | 7.218456e+03    | ±           | 2.784125e+02       | 6.430e+03       | ±           | 2.8e+02            |
| 6  | 29/11/2020 | PSAM-011353 | Co-60   | 1924.8674999999998  | 22.0   | 9.715534e+02    | ±           | 4.567788e+01       | 9.260e+02       | ±           | 3.8e+01            |
| 7  | 29/11/2020 | PSAM-011354 | Co-60   | 1924.8674999999998  | 21.0   | 1.111867e+03    | ±           | 5.115748e+01       | 1.038e+03       | ±           | 4.6e+01            |
| 8  | 29/11/2020 | PSAM-011355 | Sc-44   | 0.16841666666666666 | 79.0   | 7.306174e-82    | ±           | 2.086510e-82       | 5.530e+00       | ±           | 7.6e-01            |
| 9  | 29/11/2020 | PSAM-011355 | Ti-44   | 21586.275000000001  | 79.0   | 7.208952e+00    | ±           | 2.123653e+00       | 3.590e+00       | ±           | 5.1e-01            |
| 10 | 29/11/2020 | PSAM-011355 | Co-60   | 1924.8674999999998  | 79.0   | 4.981797e+02    | ±           | 2.243658e+01       | 4.930e+02       | ±           | 1.9e+01            |

Figure 3.1: Established database in R of all samples measured by CERN and Jacobs

Additionally, uncertainties at a 95% confidence level were available for each activity measurement performed by CERN and Jacobs. However, only the activity values were used in this study, as the focus was placed on the ratio rather than on individual measurements. Table 3.1 shows that the average relative uncertainties were highly consistent between the two institutions, suggesting that including these uncertainties would not significantly alter the conclusions.

Table 3.1: Average relative uncertainty ( $2\sigma$ ) measured by CERN and Jacobs for Co-60 and Ti-44.

| Nuclide | Average relative uncertainty ( $2\sigma$ ) measured by CERN [%] | Average relative uncertainty ( $2\sigma$ ) measured by Jacobs [%] |
|---------|---|---|
| Co-60   | 9.1958  | 9.1895  |
| Ti-44   | 19.5101   | 21.4936   |

To gain an overview of how the activity measurements from CERN compare to those from Jacobs, a scatter plot with error bars was created to display the activity ratios (C/J) for all measured samples (figure 3.2). The error bars represent the uncertainties, calculated by taking the ratio of the given uncertainties from CERN and Jacobs for each sample. The red horizontal line at a ratio of 1 indicates equal activity measurements between CERN and Jacobs.

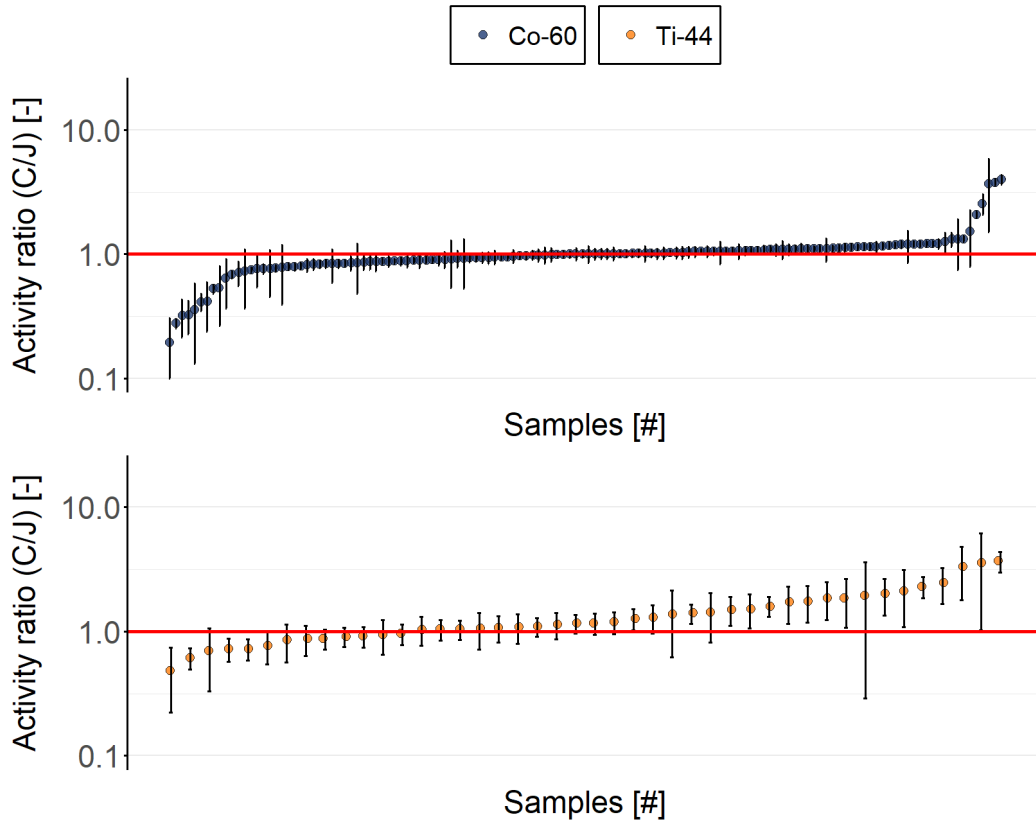
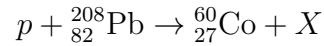


Figure 3.2: Scatter plot of the ratio of measured activity from CERN to reference activity from Jacobs (C/J), based on 134 Co-60 samples and 44 Ti-44 samples.

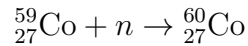
### 3.1.3 Nuclide information

This study focuses on cobalt-60 and titanium-44, as these radionuclides are commonly found in gamma spectrometry analyses of the examined samples. Co-60 is typically associated with metallic matrices due to neutron activation, whereas Ti-44 primarily originates from proton-induced reactions in accelerators.

At CERN, Co-60 is primarily produced through spallation with fragmentation and neutron capture. The spallation process occurs when high-energy protons (1 GeV), mainly produced by the Proton Synchrotron (PS) but also by Linac and Super Proton Synchrotron (SPS) accelerators, are directed at a heavy target material such as lead or uranium. These collisions cause the target nuclei to break apart into a wide range of lighter fragments, one of which can be Co-60. Because spallation generates a complex mix of isotopes, the formed Co-60 nuclei are captured and isolated using electromagnetic separation based on their mass-to-charge ratio. A representative spallation reaction is shown below, with ‘X’ representing the ensemble of residual fragments [40].



The neutron capture process for the production of Co-60 occurs mainly in n\_TOF (neutron Time-Of-Flight) facility. In this process, a stable Co-59 nucleus captures a neutron generated by proton-induced spallation on lead or uranium [41]:



Co-60 has a half-life of 5.27 years and decays 100% via beta-minus emission to excited states of Ni-60 which subsequently de-excite to the ground state by emitting characteristic gamma rays. The Q-value, i.e. the amount of energy released in this decay, is 2823.07 keV. The decay diagram is shown in figure 3.3.

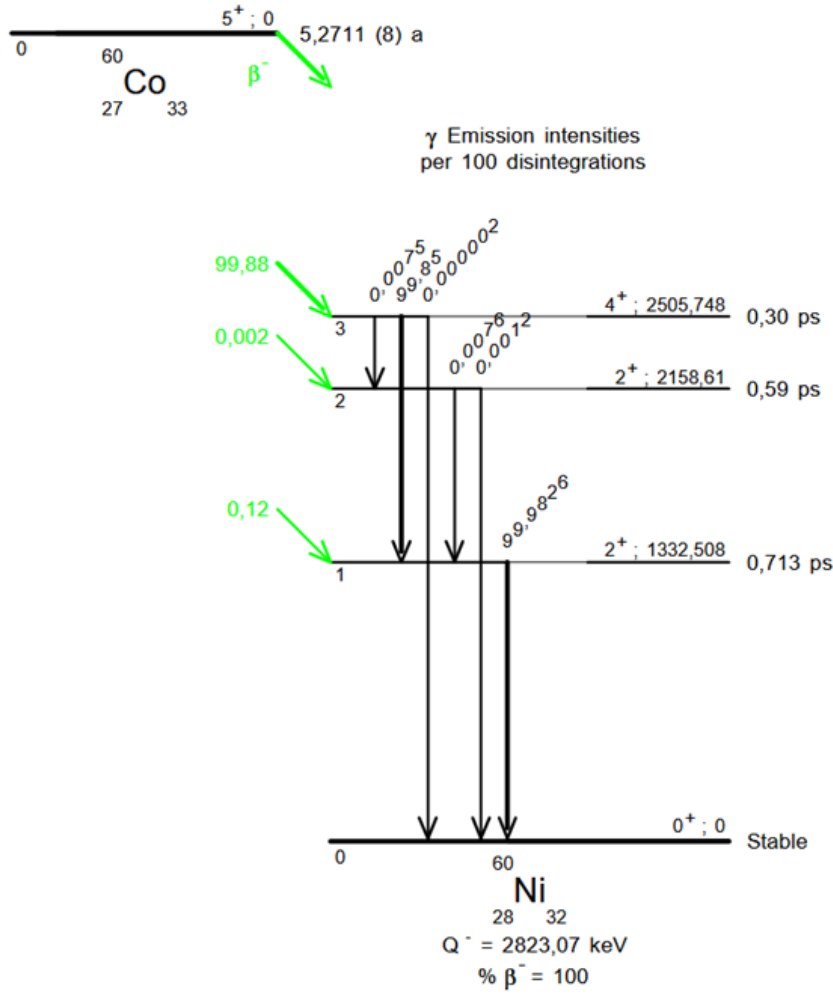
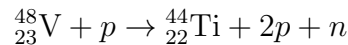
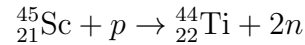


Figure 3.3: Decay scheme Co-60 [42].

Ti-44 is a rare, non-naturally occurring radionuclide. At CERN, it is generated via proton irradiation or spallation. High-energy protons produced by the PS or LINAC are directed at Sc-45 or V-48 targets, leading to the following nuclear reactions [40]:



At the ISOLDE (Isotope Separator On-Line Device) facility, Ti-44 is also produced through spallation of heavy targets by high-energy protons. The disintegration of Ti-44 is done 100% via electron capture to the excited levels in Sc-44. The ground state of Sc-44 is achieved by emitting gamma radiation from the excited levels [43].

The Q-value is 267.5 keV, which means that little energy is released during this decay, and reactions with it are endothermic. The half-life of Ti-44 is 60.0 years, and the decay diagram is shown in figure 3.4. However, the half-life of Sc-44 is short, 3.97 h, and decays by electron capture and beta plus radiation to Ca-44 [42].

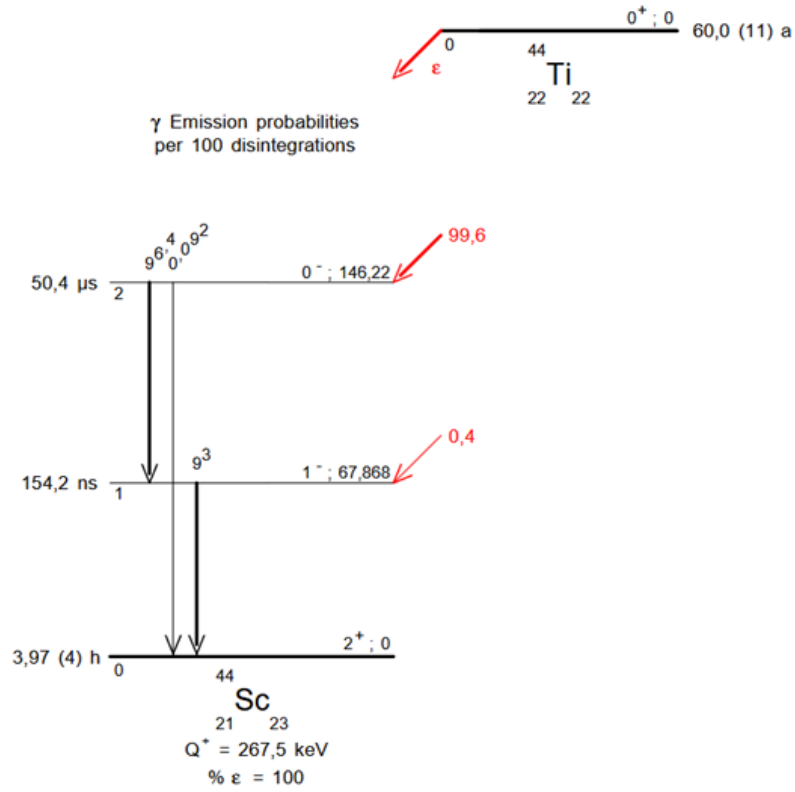


Figure 3.4: Decay scheme of Ti-44 [42].

### 3.1.4 Extended Range Coaxial Germanium detector

CERN uses the Extended Range (XtRa) Coaxial Ge detector, which is a type of HPGe detector, to perform gamma spectrometry. This detector has a thin-window contact, about 0.1–0.5 micrometers thick, made of boron-implanted silicon on the front surface, extending the effective energy range to 3 keV. In contrast, conventional coaxial detectors have a lithium-diffused contact with a thickness of 0.5–1.5 millimeters. This thick dead layer absorbs most photons below 40 keV, substantially limiting detector sensitivity to low-energy gamma rays. The XtRa Coaxial Ge detector and a carbon composite cryostat window are shown in figure 3.5(a). Figure 3.5(b) shows the detector in practice. This detector offers all the advantages of a conventional standard coaxial detector, such as high efficiency, good resolution, and moderate cost, along with the extended low-energy response of the more expensive Reverse Electrode Ge (REGe) detectors.

This detector features a vertical slimline dipstick cryostat with a carbon composite window and a 30-litre Dewar. It uses a preamplifier with a 3-meter bias, high-voltage inhibit, signal, and power cables [44].

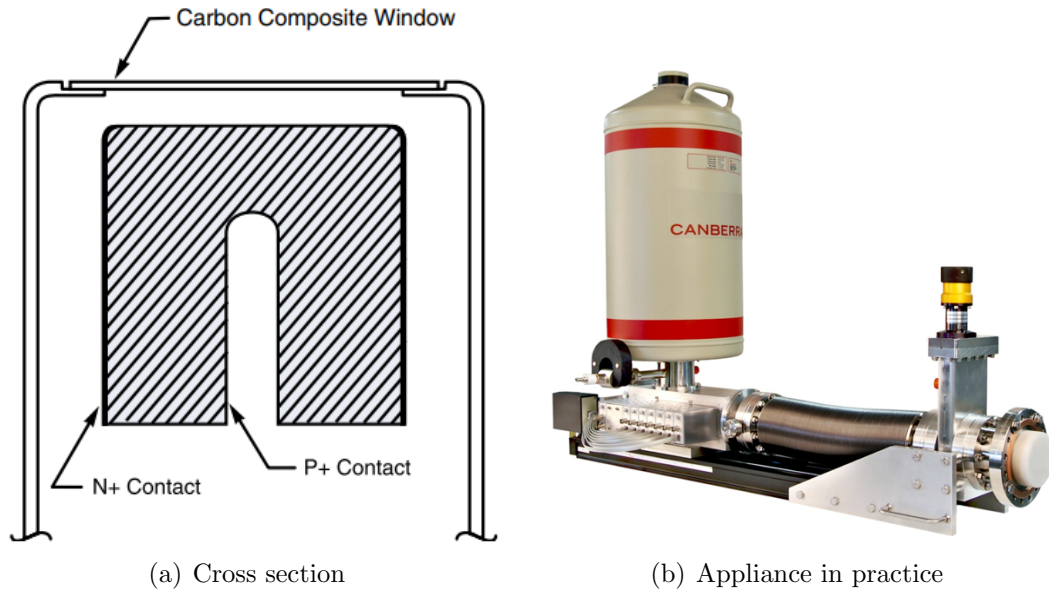


Figure 3.5: XtRa Coaxial Germanium detector [44].

The response curve of this detector is shown in figure 3.6, alongside the intrinsic efficiency of the conventional Ge detector. The principle behind this curve has already been explained before in section 2.1.3.

The adequate window thickness can be determined experimentally by comparing the intensities of the 22 keV and 88 keV gamma peaks of Cd-109. Beryllium and aluminium windows are also available; however, they are not preferred due to their higher cost, mechanical fragility, and limited suitability in Ultra-Low Background (ULB) applications. If full advantage of the low-energy capability is required, non-ULB beryllium windows may be chosen on special request after consulting the factory.

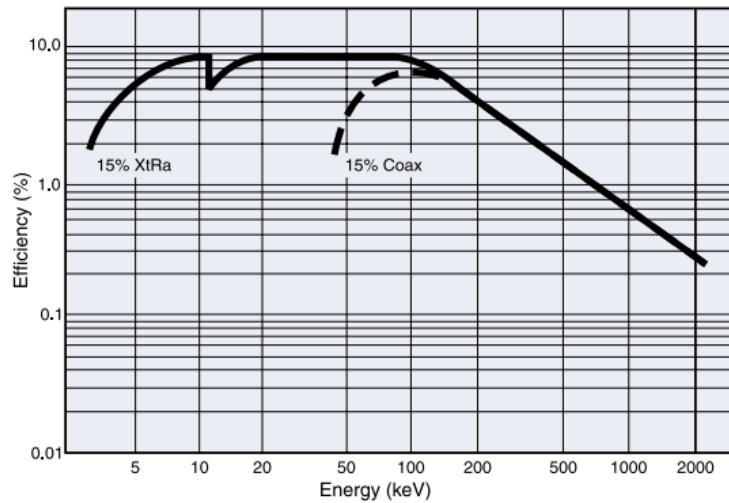


Figure 3.6: Efficiency curves for the XtRa with Be window and standard with Li window Coaxial Detector, computed with a source-to-detector distance of 2.5 cm [44].

## 3.2 Methodology

### 3.2.1 Comparison of measurement methods

To determine whether the CERN and Jacobs measurement methods produce comparable results, statistical tests must be applied to a dataset of paired observations. The Wilcoxon signed-rank test is a non-parametric method that does not assume normality and is therefore appropriate as an initial analysis tool. The paired t-test can also be used to evaluate whether there is a statistically significant difference between the two measurement methods. However, the paired t-test assumes that the differences between paired observations are approximately normally distributed. The Shapiro–Wilk test can be performed to verify this assumption.

#### Wilcoxon signed-rank test

The Wilcoxon signed-rank test is a non-parametric statistical method used to evaluate whether the median of the paired differences between two related samples significantly deviates from zero. This test is appropriate when data are measured on an ordinal or continuous scale, the samples are paired, the data is not normally distributed, and the distribution of the pairwise differences is symmetric. A key advantage of the Wilcoxon signed-rank test is its ability to analyse ordinal data and reduce the impact of outliers.

The null hypothesis states that the median of the differences between paired observations in the population equals zero. The alternative hypothesis may specify that the median is not equal to zero (in a two-tailed test) or greater than or less than zero (in a one-tailed test).

The procedure begins by computing the difference between each pair of measurements. The absolute values of these differences are ranked in ascending order, ignoring the sign. Pairs that yield a precisely zero difference are excluded from the ranking process. In cases where two or more absolute differences are identical, average ranks are assigned; this is referred to as the use of tied or connected ranks. After ranking, the original signs of the differences are reinstated. The ranks associated with positive differences are summed to obtain  $T_+$ , and those related to negative differences are summed to obtain  $T_-$ .

The correlation between these rank totals is:

$$T_+ + T_- = \frac{n(n+1)}{2} \quad (3.1)$$

where  $n$  denotes the number of non-zero paired differences. The test statistic,  $W$ , is then defined as the smaller of these two sums:

$$W = \min(T_+, T_-) \quad (3.2)$$

Smaller values of the test statistic indicate that the observed differences are closer to what would be expected under the null hypothesis of no median difference.



For small sample sizes, the statistical significance of  $W$  is typically evaluated using exact critical values from the Wilcoxon distribution. The expected value of  $W$  under the null hypothesis is given by:

$$\mu_W = \frac{n(n+1)}{4} \quad (3.3)$$

and the standard deviation by:

$$\sigma_W = \sqrt{\frac{n(n+1)(2n+1)}{24}} \quad (3.4)$$

The test statistic can then be standardised using the z-transformation:

$$z = \frac{W - \mu_W}{\sigma_W} \quad (3.5)$$

This z-value can be compared to critical values from the standard normal distribution. For a two-tailed test at the 0.05 significance level, the critical values are approximately  $\pm 1.96$ . The null hypothesis is rejected if the calculated z-value falls outside this range, indicating a statistically significant difference. Alternatively, the p-value associated with the z-score may be computed. The null hypothesis is rejected if this p-value is less than the significance level.

In R, the Wilcoxon signed-rank test can be conducted using the built-in `wilcox.test()` function as follows:

```
wilcox.test(x, y, paired = TRUE)
```

where `x` and `y` represent the two paired datasets. This function returns both the test statistic  $W$  and the associated p-value [45].

### Paired t-test

The paired samples t-test is a statistical method used to determine whether the mean of the paired differences between two related measurements significantly differs from zero. It is appropriate when each observation in one group can be naturally paired with an observation in the other group, such as when the same sample is measured under two different conditions or using two different methods.

This test relies on several assumptions:

- the observations are paired and come from the same subjects or units;
- each pair is independent of all other pairs;
- both groups must have the same sample size;
- the data should be continuous and approximately normally distributed.

The null hypothesis states that the mean of the differences between the paired observations is zero, indicating no statistically significant difference. The alternative hypothesis is that the mean difference is not zero, suggesting a statistically significant difference exists. The test can be either two-sided or one-sided, depending on the research question.

The test statistic  $t$  is calculated with the following equation

$$t = \frac{\bar{x}_d - \mu_d}{\frac{s_d}{\sqrt{n}}} \quad (3.6)$$

where:

- $\bar{x}_d$  is the mean of the differences between the paired observations;
- $\mu_d$  is the expected difference under the null hypothesis (usually equal to 0);
- $s_d$  is the standard deviation of the differences;
- $n$  is the number of pairs.

The corresponding p-value is obtained by comparing the test statistic to a t-distribution with  $n - 1$  degrees of freedom. If the p-value is less than the chosen significance level, the null hypothesis is rejected, and it is concluded that a significant difference exists between the paired groups. Otherwise, the null hypothesis is not rejected.

In R, the paired t-test can be performed using the built-in `t.test()` function:

```
t.test(x, y, paired = TRUE, alternative = "two.sided")
```

where  $x$  and  $y$  are the two numeric vectors of paired data. This function returns both the test statistic  $t$  and the associated p-value [46].

### Shapiro-Wilk test

The Shapiro-Wilk test is a hypothesis test used to evaluate whether a dataset is drawn from a normally distributed population. Normality means that the population follows a Gaussian distribution, though not necessarily a standard normal distribution (with a mean of zero and a variance of one). In a normal distribution, values are symmetrically distributed around the mean, with most values clustered near the mean and fewer values in the tails.

This hypothesis test is a goodness-of-fit test that assesses how closely the ordered sample values match the expected values from a normal distribution. It calculates a  $W$ -statistic that quantifies how well the data conforms to a normal distribution. Values closer to 1 indicate that the data likely follow a normal distribution, whereas values closer to 0 suggest deviation from normality. In practice,  $W$ -values above 0.95 are often considered indicative of normality, although the formal decision is based on the p-value. The p-value reflects the probability of obtaining the observed  $W$ -statistic if the data were normally distributed. If the p-value is less than the chosen significance level (commonly  $\alpha = 0.05$ ), the null hypothesis is rejected, indicating that the data are not normally distributed.

The test is sensitive to various deviations from normality, including skewness and outliers, so visual inspection and potential data transformation should be considered before drawing firm conclusions based solely on the p-value.

In R, the Shapiro-Wilk test is performed by using the function:

```
shapiro.test(x)
```

where  $x$  is a numeric vector of data values.

This function returns the W-statistic and the associated p-value. In R, the null hypothesis is that the data are normally distributed, while the alternative is that they are not. If the p-value is less than 0.05, there is sufficient evidence to conclude that the data deviate significantly from normality [47].

### 3.2.2 Estimation of measurement deviations introduced by the envelope method

Several statistical techniques can be used to evaluate measurement deviations introduced by the envelope method. The error in measurements by CERN, relative to those by Jacobs, can be assessed using the Kullback–Leibler (KL) divergence. The uncertainty is quantified by the Full Width at Half Maximum (FWHM) of the distribution of the activity ratio between CERN and Jacobs, abbreviated as C/J. Additionally, the bias in the ratio of CERN to Jacobs measurements is estimated as the difference between the median of the distribution and 1.

#### Estimation of the error introduced using the envelope method

The theoretical basis of the KL divergence is discussed in section 2.3.2. Since no standard R function or package directly implements this computation, a custom function must be written. The relevant formula is given in equation 2.19 for discrete probability distributions and in equation 2.20 for continuous ones.

As the KL divergence requires input in the form of probability distributions, the activity measurements from CERN and Jacobs must first be transformed accordingly. This is achieved using Kernel Density Estimation (KDE), which is a method for estimating a continuous random variable Probability Density Function (PDF). KDE produces a smooth, continuous density by centring a kernel (a smooth function) over each data point and summing them to generate the PDF. It can be seen as a continuous, smoothed alternative to a histogram, which instead groups the data into discrete bins.

A crucial subsequent step is to define the PDFs,  $P(x)$  and  $Q(x)$ , over the same set of  $x$ -values. This is done by interpolating both density estimates onto a shared domain.

If the discrete form of the KL divergence is applied, the interpolated values must be normalised, such that their sum equals one. This conversion ensures that they represent valid discrete probability distributions.

Finally, the KL divergence is computed using either the continuous or discrete form of the formula. A small constant epsilon is added to all probability values to prevent division by zero or undefined logarithmic operations [36].

If the KL divergence is zero, it indicates that the two distributions are identical. Values of KL divergence close to zero imply a high degree of similarity between the distributions, while larger values suggest a greater divergence or dissimilarity. In the context of measurement comparisons, this reflects how closely CERN measurements (after applying the envelope method) approximate those from Jacobs.

#### Estimation of uncertainty introduced using the envelope method

The activity ratio (C/J) is analysed to assess the consistency between the two sets of activity measurements. The statistical properties of the C/J distribution provide valuable insights into the agreement between the two methods. In particular, the FWHM of the distribution can serve as a proxy for estimating the uncertainty introduced by the envelope method.

Several methods are available for determining the FWHM. One approach is to calculate it directly from a histogram of the data; however, this method is sensitive to the chosen bin size and thus introduces a degree of arbitrariness in the result. An alternative and more robust strategy, particularly when no obvious distribution shape is apparent, is to fit the data to parametric distributions and compute the FWHM based on the best-fitting model. In the following, this method will be applied using the normal, log-normal, and gamma distributions to evaluate which model best fits the data.

If the C/J distribution can be modelled as a normal distribution of the form:

$$f(x) = \frac{1}{\sigma\sqrt{2\pi}} \exp\left(-\frac{(x-x_0)^2}{2\sigma^2}\right) \quad (3.7)$$

where  $\sigma$  denotes the standard deviation and  $x_0$  the expected value, then the relationship between FWHM and standard deviation of that data would be expressed as:

$$\text{FWHM} = 2\sqrt{2\ln(2)} \cdot \sigma \approx 2.355 \cdot \sigma. \quad (3.8)$$

Equation 3.8 shows that for a normal distribution, the FWHM is directly related to the standard deviation, and therefore to the statistical uncertainty of the measurement. In a normal distribution, the FWHM is directly related to the standard deviation ( $\sigma$ ), with  $\mu \pm 2\sigma$  representing the 95% confidence interval, reflecting the uncertainty in the dataset. This relationship can be expressed in terms of FWHM using equation 3.8, showing that FWHM and  $\sigma$  convey equivalent information in different forms [48].

The log-normal distribution is a continuous probability distribution of a random variable whose logarithm is normally distributed [49]. The gamma distribution is a continuous probability distribution defined by two parameters (shape  $\alpha$  and scale  $\theta$ ) generally used to model skewed distributions [50].

For distribution fitting, the classical coefficient of determination  $R^2$ , which quantifies the proportion of variance in the response explained by the predictors in a regression setting, is not applicable. Instead, the pseudo- $R^2$  is used to quantify the agreement between the empirical distribution of the data and the fitted distribution.

The formula used is:

$$\text{Pseudo } R^2 = 1 - \frac{SS_{\text{res}}}{SS_{\text{tot}}} = 1 - \frac{\sum_i [f_{\text{emp}}(x_i) - f_{\text{model}}(x_i)]^2}{\sum_i [f_{\text{emp}}(x_i) - \bar{f}_{\text{emp}}]^2} \quad (3.9)$$

where:

- $SS_{\text{res}}$  is the residual sum of squares,
- $SS_{\text{tot}}$  is the total sum of squares,
- $f_{\text{emp}}(x_i)$  is the empirical density at point  $x_i$ ,
- $f_{\text{model}}(x_i)$  is the theoretical density at point  $x_i$ ,
- $\bar{f}_{\text{emp}}$  is the mean of the empirical density values.

The statistic ranges from 0 to 1; higher values indicate a closer match between the fitted distribution and the observed data.

The `fitdistrplus` package can be used to visualise the model fit in R. It provides a histogram with theoretical density plots, Q-Q plots, P-P plots, and empirical vs. theoretical CDF plots, overlaid with the normal, log-normal, and gamma distributions.

Once the best-fitting model for the data is identified, the FWHM of the activity ratio (C/J) can be determined. For the normal distribution, FWHM is calculated using equation 3.8. For the lognormal distribution, the FWHM is derived using the mean and standard deviation of the underlying normal distribution. An approximate formula for the FWHM in the log-normal case is:

$$\text{FWHM} \approx \exp(\mu + \sigma^2) \cdot \left[ \exp\left(\sigma\sqrt{2\ln 2}\right) - \exp\left(-\sigma\sqrt{2\ln 2}\right) \right] \quad (3.10)$$

For the gamma distribution, the FWHM depends on the shape parameter  $\alpha$  and the scale parameter  $\theta$ . This calculation has no closed-form solution and must be performed numerically.

In addition to fitting parametric distributions, a non-parametric alternative is available through the bootstrap method, as explained in section 2.3.3. This approach is particularly useful when working with small datasets, where traditional statistical assumptions (e.g. normality) may not hold or where limited data prevents reliable parameter estimation. Unlike parametric methods, the bootstrap does not assume a specific underlying distribution.

There is no single function or command for applying the bootstrap method in R, so multiple steps are required. First, the original data must be accessed, and multiple bootstrap samples are generated by randomly sampling with replacement from the dataset (C/J). For each bootstrap sample, the FWHM is computed. This process yields a distribution of FWHM estimates for the activity ratio (C/J), from which the average FWHM can be derived [37].

A narrow FWHM of the activity ratio (C/J) distribution indicates low uncertainty introduced by the envelope method, while a broader FWHM corresponds to greater uncertainty and a wider spread around the ideal activity value of 1.

#### Estimation of bias introduced using the envelope method

Statistical bias refers to a property of a statistical technique or its results where the expected outcome value deviates from the true underlying quantitative parameter being estimated. This should not be confused with precision, which relates to sampling variability. Bias is formally defined as:

$$\text{Bias}(T, \theta) = E(T) - \theta \quad (3.11)$$

where  $T$  represents the statistic used to estimate the parameter  $\theta$ , and  $E(T)$  denotes the expected value of  $T$ . If  $\text{Bias}(T, \theta) = 0$ , the estimator is said to be unbiased; otherwise, it is biased [51].

In the context of this study, bias is defined as the difference between the median of the activity ratio (C/J) and the ideal value of 1. A ratio of 1 implies that the measurements from CERN and Jacobs are equal. Any deviation from this value reflects bias in the estimation method. Bias can be estimated using either the mean or the median of the ratio distribution. The median-based bias is robust to outliers, while the mean-based bias incorporates all values, including extreme ones, making it more sensitive to skewed data. In datasets where extreme values are present or the distribution is asymmetric, the median provides a more stable and representative estimate of central tendency.

Skewness is a statistical measure of the asymmetry of a probability distribution relative to a normal distribution. It indicates both the direction and degree of deviation from symmetry and provides insight into the presence and influence of outliers.

The following expression can approximate the skewness:

$$\frac{\mu - \nu}{\sigma} \quad (3.12)$$

where  $\mu$  is the mean,  $\nu$  is the median, and  $\sigma$  is the standard deviation.

This non-parametric interpretation helps to identify the direction of skew: a positive result suggests right-skewness, while a negative result indicates left-skewness.

Figure 3.7 illustrates the various forms of skewness and serves as a basis for the following discussion. In a symmetric distribution, such as the normal distribution, the two tails are of equal length and mirror each other around the mean. In such cases, the skewness is equal to zero. If the distribution is unimodal, the mean, median, and mode coincide. However, a skewness value of zero does not guarantee symmetry. Certain asymmetric distributions, for example, those with a long, thin tail on one side and a short, heavy tail on the other, may yield zero skewness. This highlights the limitation of skewness as a standalone indicator of symmetry. Therefore, assessing distribution symmetry should not rely solely on its skewness value. Instead, the overall shape of the distribution must be considered.

A positively skewed (right-skewed) distribution, as shown in the left plot of figure 3.7, has a longer right tail. This causes the bulk of the data to lie towards the left. In such cases, the mean is pulled to the right of the median, and the order of central tendency measures typically follows:  $\text{mode} < \text{median} < \text{mean}$ .

A negatively skewed (left-skewed) distribution, illustrated in the right plot of figure 3.7, features a longer left tail. Here, the bulk of the data lies to the right, with the mean shifted leftward from the median. In this case, the order of central tendency is  $\text{mean} < \text{median} < \text{mode}$  [52].

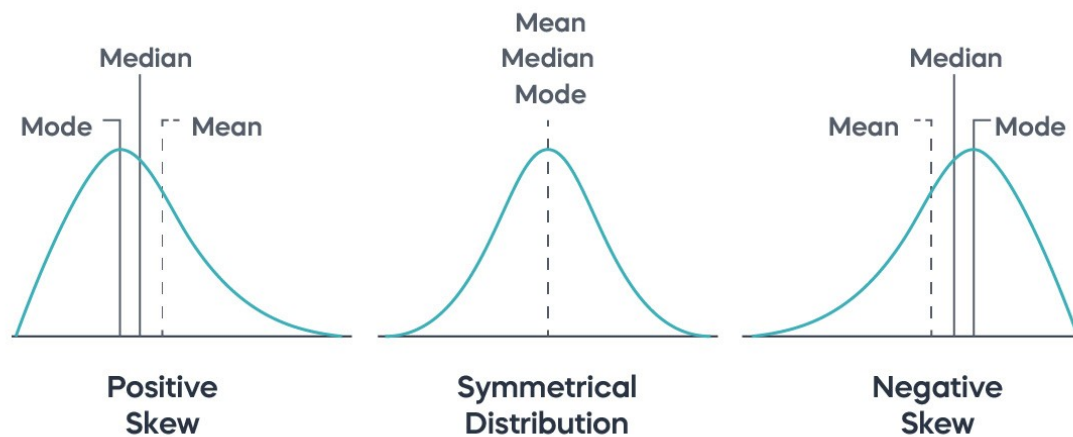


Figure 3.7: Schematic representation of the three different types of skewness in the distribution of data [53].

# Chapter 4

## Results and discussion

Chapter 4 provides an in-depth discussion, interpretation, and evaluation of the results obtained from the statistical tests used to compare the measurement methods. The same approach is applied to assess the error, uncertainty, and bias associated with the envelope method. Currently, no established acceptance criteria exist for these metrics; therefore, the results presented in this chapter cannot be directly benchmarked against predefined thresholds to determine the suitability of the envelope method for routine implementation at CERN. Nonetheless, where applicable, the results are compared with the findings reported in previous studies.



## 4.1 Comparison of measurement methods

### 4.1.1 Wilcoxon signed-rank test

The Wilcoxon signed-rank test is carried out to determine whether the median of the paired differences between the activities measured by CERN and Jacobs for the same sample significantly differs from zero. Each of the differences is calculated as CERN minus Jacobs. In R, the Wilcoxon signed-rank test is performed for both Co-60 and Ti-44 using the `wilcox.test()` function. The null hypothesis is set by default in R and states that the median of the differences between CERN and Jacobs is zero. The alternative hypothesis states that the median of the differences is not equal to zero. This code outputs the statistical value  $W$  and the associated p-value, which are presented in table 4.1.

In R, the  $W$ -value is the sum of the positive ranks ( $T_+$ ). A large  $W$ -value suggests significant positive differences between paired measurements, providing evidence against the null hypothesis. The more extreme the rank sum, the more substantial the evidence against the null hypothesis.

In the context of this study, a standard confidence level of 95% is used, corresponding to an alpha value of 0.05.

For Co-60, the p-value is 0.09102. Since  $p > \alpha$ , the null hypothesis is not rejected. At the 95% confidence level, there is insufficient evidence to conclude that the median of the paired differences between CERN and Jacobs activity measurements differs from zero.

For Ti-44, the p-value is 0.04332. Since  $p < \alpha$ , the null hypothesis is rejected. There is sufficient statistical evidence at the 95% confidence level to conclude that the median of the paired differences between CERN and Jacobs activity measurements differs from zero.

Table 4.1: Results of the Wilcoxon signed-rank test for Co-60 and Ti-44.

| Nuclide | Test Statistic $W$ | p-value |
|---------|--------------------|---------|
| Co-60   | 5284.00000         | 0.09102 |
| Ti-44   | 668.00000          | 0.04332 |

### 4.1.2 Paired t-test and Shapiro-Wilk test

The paired t-test is conducted to determine whether the mean of the paired differences between the activity measurements by CERN and Jacobs for the same samples significantly differs from zero. This test relies on two key assumptions: (1) it is performed using the differences between the two datasets, and (2) the differences must be normally distributed. To satisfy these assumptions, the activity differences were calculated as CERN minus Jacobs, and the hypothesis of normality was assessed with the Shapiro-Wilk test.

To visually inspect the distribution of these differences, a density plot was generated for Co-60 (figure 4.1) and Ti-44 (figure 4.2). Although a central peak is present for both nuclides, the asymmetry and the behaviour of the tails raise doubts about conformity to a Gaussian distribution.

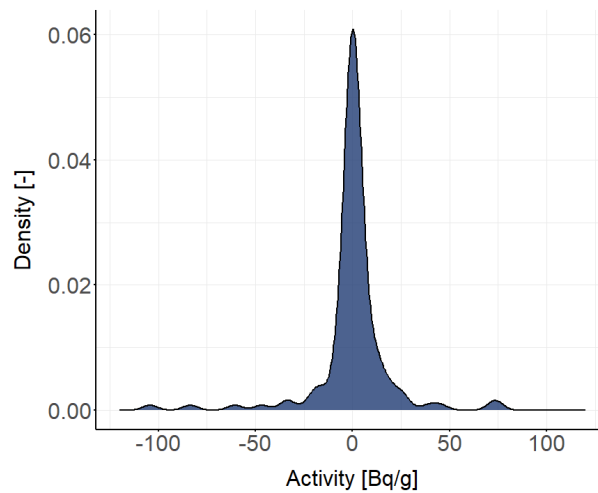


Figure 4.1: Density plot of the differences in Co-60 activity measurements between CERN and Jacobs (CERN – Jacobs), based on 134 paired samples.

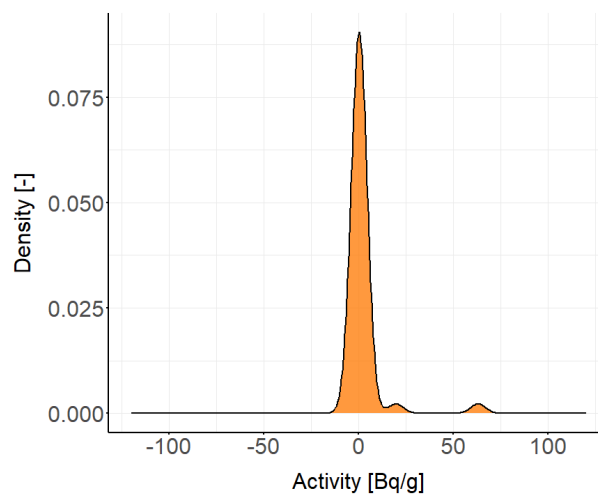


Figure 4.2: Density plot of the differences in Ti-44 activity measurements between CERN and Jacobs (CERN – Jacobs), based on 44 paired samples.

Increasing the bandwidth results in smoother curves that closely resemble a normal distribution, while decreasing it reveals more local structures and variability. Therefore, a purely visual assessment does not allow for a definitive conclusion regarding normality, especially with limited sample sizes.

To formally test for normality, the `shapiro.test()` function in R was used to conduct a Shapiro-Wilk test. The null hypothesis states that the data (the differences in activity measurements (CERN - Jacobs)) is normally distributed, while the alternative hypothesis states the opposite.

The R output provides the test statistic  $W$  and the corresponding p-value, which are reported in table 4.2 for both nuclides. Both nuclides have a  $W$ -value that is considerably far from 1, indicating strong deviations from normality.

The p-value for both nuclides are significantly lower than  $\alpha$ , leading to rejection of the null hypothesis. Therefore, at the 95% confidence level, there is strong statistical evidence that the paired differences in activity measurements between CERN and Jacobs are not normally distributed for Co-60 and Ti-44.

Table 4.2: Results of the Shapiro-Wilk test for Co-60 and Ti-44.

| Nuclide | Test Statistic $W$ | p-value                  |
|---------|--------------------|--------------------------|
| Co-60   | 0.29573            | $1.3333 \times 10^{-23}$ |
| Ti-44   | 0.29305            | $2.9129 \times 10^{-13}$ |

As the Shapiro-Wilk test did not confirm normality in the distribution of the paired differences, the application of a paired t-test cannot be performed, given that normality is a prerequisite for its validity.

### 4.1.3 Discussion of results

Two statistical tests could be applied to evaluate the comparison between the activity measurements obtained by CERN and Jacobs: the Wilcoxon signed-rank test and the paired t-test. Both tests are appropriate for paired data but differ in their underlying assumptions and statistical focus. The Wilcoxon signed-rank test assesses whether the median of the paired differences significantly deviates from zero, without assuming a specific distribution for the differences. In contrast, the paired t-test evaluates whether there is a significant difference in the mean of the paired differences, assuming that these differences are normally distributed.

The Wilcoxon signed-rank test indicated no statistically significant difference in the paired measurements for Co-60, whereas a significant difference was observed for Ti-44 at the 95% confidence level. Prior to considering the application of the paired t-test, the Shapiro–Wilk test was conducted to assess whether the distribution of paired differences conformed to the assumption of normality. This step was essential, as there was no a priori reason to assume that the distribution of paired differences would be normally distributed. The results of the Shapiro–Wilk test provided strong evidence that the paired differences in activity measurements between CERN and Jacobs were not normally distributed for either Co-60 or Ti-44. As the assumption of normality was not met, the paired t-test was deemed unsuitable for the current dataset. However, should a future study be conducted with a dataset for which the normality assumption holds, the paired t-test would be an appropriate method for determining the presence of statistically significant differences.

Accordingly, only the results of the Wilcoxon signed-rank test will be considered statistically reliable for the current dataset.

In conclusion, it can be stated that at a 95% confidence level, the activity measurement methods of CERN and Jacobs yield comparable results for Co-60. For Ti-44, however, a statistically significant difference was observed, indicating that the two methods do not produce equivalent results for this isotope. It is important to note that a non-significant result (as for Co-60) does not prove equivalence; it means that any observed difference is not large enough to be deemed statistically meaningful given the chosen significance level.

These findings are specific to the current comparison between the CERN and Jacobs methodologies and should not be generalised beyond this study. Although the statistical methods employed are well-established, the results are inherently tied to the characteristics of the present dataset and experimental design. Consequently, the outcomes of this analysis cannot be directly compared with those of previously conducted studies, which may differ in methodological approach, measurement systems, or sample composition.

## 4.2 Estimation of measurement deviations introduced by the envelope method

### 4.2.1 The error

To quantify the dissimilarity between the probability distributions of the activity measurements from CERN and Jacobs, the Kullback–Leibler (KL) divergence is employed. Specifically, its discrete form is used (equation 2.19), where  $P$  represents the reference (or “true”) probability distribution, Jacobs in this case, and  $Q$  represents the approximate or assumed distribution, CERN.

The raw data, consisting of continuous activity measurements from both institutions, do not constitute discrete probability distributions. Therefore, Kernel Density Estimation (KDE) is employed to obtain smooth probability density functions from the data. This method produces a smooth curve, representing the likelihood of different activity values. In R, the `density()` function is used to perform KDE. The resulting KDE-based distributions for both  $P$  and  $Q$  each comprise 512 evaluation points along the x-axis, as shown in figure 4.3 for Co-60 and figure 4.4 for Ti-44.

For Co-60 (figure 4.3), the KDE curves of CERN and Jacobs are nearly identical. Particularly at lower activity levels (up to 1000 Bq/g), the peaks of the two distributions align closely, suggesting strong agreement between the two measurement methods in this region. Minor differences between 1000 and 3000 Bq/g are observed, where Jacobs shows a slightly lower density than CERN. Although the densities remain similar at higher activity levels (above 3000 Bq/g), their peaks occur at somewhat different activity values. Overall, due to the high degree of overlap, the KL divergence is expected to be close to zero, indicating minimal difference between the methods.

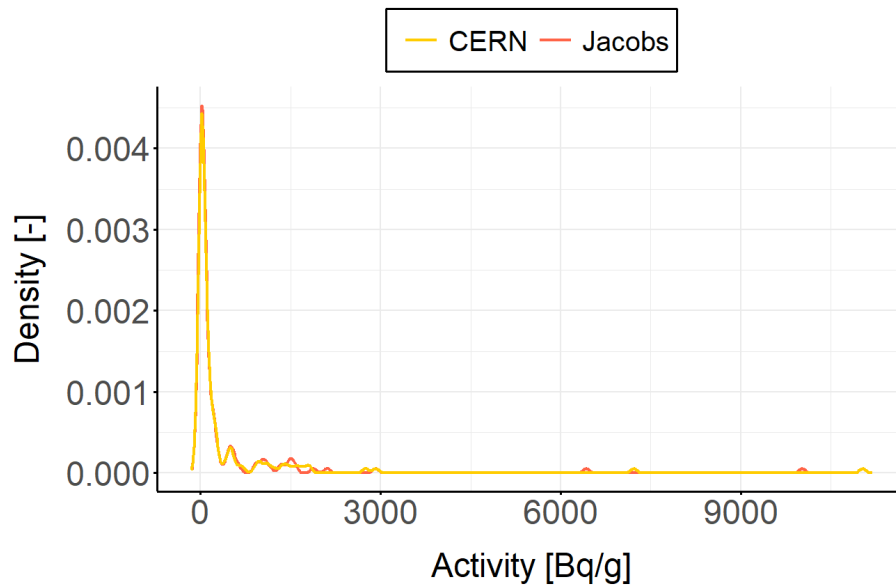


Figure 4.3: Kernel Density Estimation plot of Co-60 activity measurements from CERN and Jacobs, based on 134 samples.

In contrast, for Ti-44 (figure 4.4), the KDE curves differ more substantially. The main peak at very low activities is higher for Jacobs than for CERN. The distribution from CERN generally shows lower density values at peak locations, which are more prominent in the distribution from Jacobs. These discrepancies suggest a moderate to substantial discrepancy between the measurement methods for this radionuclide.

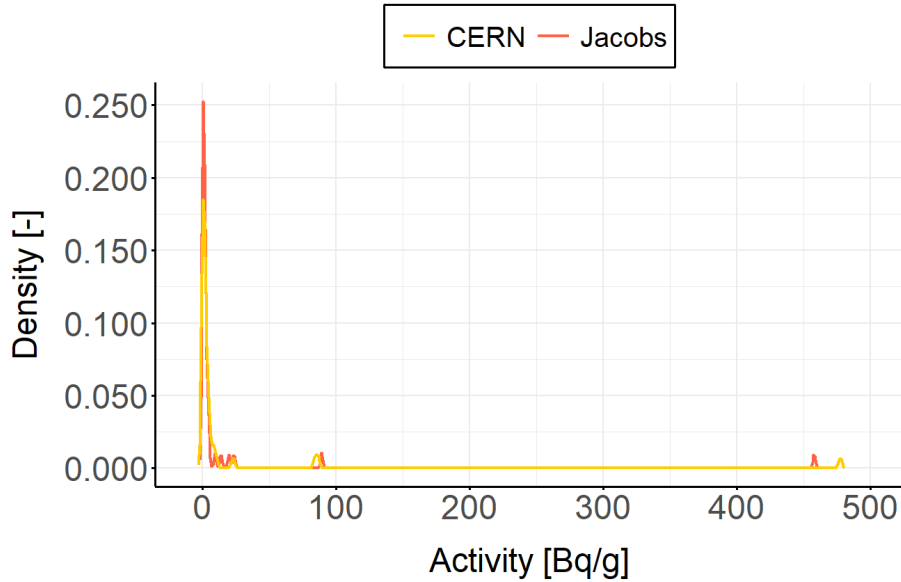


Figure 4.4: Kernel Density Estimation plot of Ti-44 activity measurements from CERN ( $Q(x)$ ) and Jacobs ( $P(x)$ ), based on 44 samples.

To compute the KL divergence, both KDE outputs are first interpolated using the `approx()` function in R to ensure that  $P$  and  $Q$  are evaluated over the same  $x$ -values. Then, both sets of density values are normalised to obtain valid discrete probability distributions.

To ensure the KL divergence is defined, it is required that whenever  $Q(x)=0$ , then  $P(x)=0$ ; this condition is fulfilled with this dataset. However, to avoid numerical instability and prevent the KL divergence from approaching infinity, a small constant is added to all values in both  $P$  and  $Q$ . This constant,  $\epsilon = 2.220446 \times 10^{-16}$ , is the smallest positive number such that  $1 + \epsilon \neq 1$  in R.

Finally, the final KL divergence is calculated in R using:

```
kl_divergence <- sum(P * log(P / Q), na.rm = TRUE)
```

where  $P$  and  $Q$  are the discrete probability distributions derived from the Jacobs and CERN KDEs, respectively.

The resulting Kullback–Leibler divergence values are 0.5528 for Co-60 and 0.9331 for Ti-44. Although no universally accepted thresholds exist for interpreting KL divergence, prior studies have proposed several heuristic guidelines and practical criteria to guide in the evaluation of such results [54]. For Co-60, the observed KL divergence indicates a moderate level of agreement between the results from CERN and Jacobs, suggesting some noticeable differences. In contrast, the KL divergence obtained for Ti-44 reflects a substantial deviation, indicating limited comparability between the two measurement methods.

### 4.2.2 The uncertainty

The FWHM of the activity ratio (C/J) distribution was used as an uncertainty metric. This uncertainty represents how much the activity measured by CERN may deviate from the reference activity measured by Jacobs, due to the use of a simplified standard geometry. The results of the three methods used in this study to determine the FWHM of the activity ratio (C/J) distribution are discussed below, followed by a comparative analysis of their outputs.

#### Histogram-based estimation

This approach involved generating a histogram of the activity ratios and estimating its FWHM as a measure of uncertainty. Since the outcome is sensitive to the choice of bin size, multiple bin sizes were tested for both Co-60 and Ti-44. Table 4.3 summarises the resulting FWHM values. The maximum frequency (i.e. the histogram peak) of the histogram was first identified, after which half its peak height was used as a reference to determine the leftmost and rightmost bins corresponding to the half-maximum level. The FWHM was then calculated as the distance between these two bin centres.

As expected, the FWHM varied substantially with minor adjustments to the bin size, as reflected in table 4.3. These fluctuations are relatively large compared to the minor adjustments in bin size, highlighting the lack of robustness and reliability of this method. Furthermore, since no optimal bin size was established, the results remain subject to interpretative variability and are therefore not considered reliable for uncertainty estimation.

Table 4.3: FWHM values for different bin sizes of the activity ratio (C/J) distribution for Co-60 and Ti-44.

| Nuclide | Bin size [-] | FWHM [-] |
|---------|--------------|----------|
| Co-60   | 0.10         | 0.30     |
|         | 0.05         | 0.25     |
|         | 0.01         | 0.39     |
| Ti-44   | 0.10         | 0.30     |
|         | 0.05         | 1.20     |
|         | 0.01         | 3.22     |

#### Parametric model fitting estimation

Another method for estimating the uncertainty involves calculating the FWHM from a fitted probability distribution that best represents the activity ratio data. As a preliminary step, the activity ratios between CERN and Jacobs were visualised for both Co-60 and Ti-44. Figure 4.5 and figure 4.6 present density plots for the Co-60 and Ti-44 ratios. Both distributions exhibited a dominant peak around a ratio of 1, alongside multiple secondary peaks.

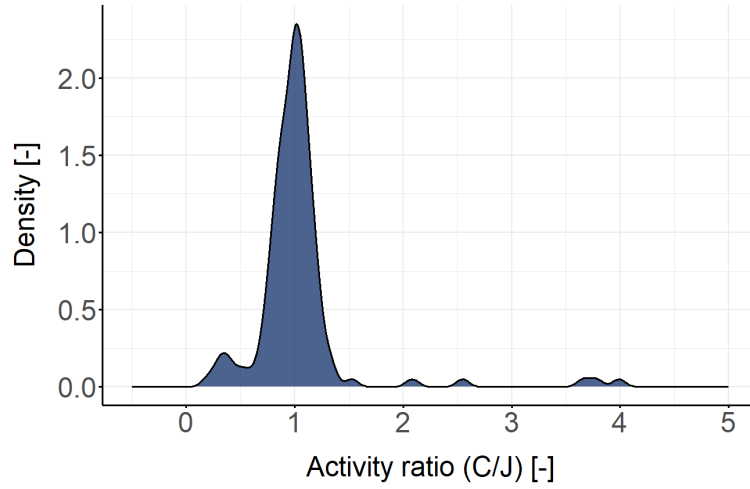


Figure 4.5: Density plot (bandwidth = 0.06) of Co-60 activity ratio (C/J), based on 134 samples.

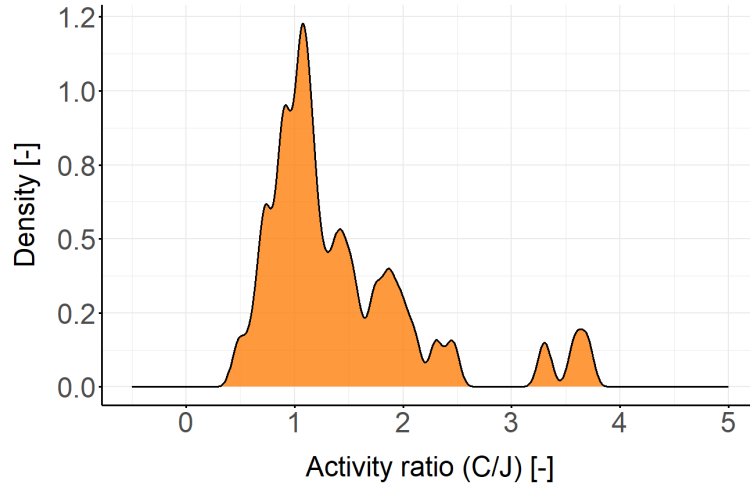


Figure 4.6: Density plot (bandwidth = 0.06) of Ti-44 activity ratio (C/J), based on 44 samples.

To better characterise the activity ratios, a distribution fitting procedure was performed using the `fitdistrplus` package in R. Three candidate distributions were considered: normal, log-normal, and gamma. The fitted curves are shown in figure 4.7. Visual inspection indicated that the log-normal distribution provided the best fit for both isotopes. This was supported by the pseudo- $R^2$  metric (section 3.2.2), which quantifies the goodness of fit. Its values are presented in table 4.4, alongside the mean and the standard deviation of each model for both nuclides. For Co-60, the log-normal and gamma distributions yielded similar pseudo- $R^2$  values (0.6225 vs. 0.6226), whereas for Ti-44, the log-normal fit achieved a much higher pseudo- $R^2$  of 0.9728, indicating a near-perfect fit.

The FWHM values derived from the log-normal fits were 0.7728 for Co-60 and 1.1567 for Ti-44.



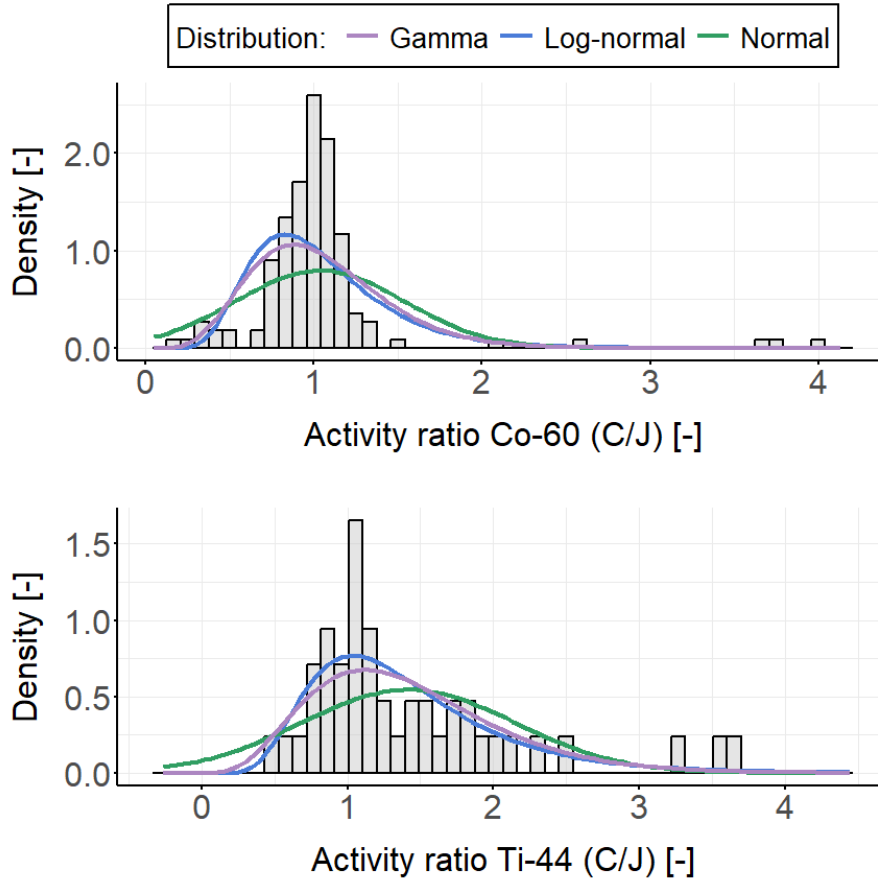


Figure 4.7: Histogram of the Co-60 (top) and Ti-44 (bottom) activity ratios between CERN and Jacobs (C/J) with parametric distribution fits.

Table 4.4: Mean, standard deviation, and pseudo- $R^2$  for the fitted distributions of the Co-60 and Ti-44 activity ratios. For the log-normal distribution, values were back-transformed from the log scale. For the gamma distribution, the mean and standard deviation were computed from the shape and rate parameters.

| Nuclide | Distribution | Mean [-] | Standard deviation [-] | Pseudo- $R^2$ [-] |
|---------|--------------|----------|------------------------|-------------------|
| Co-60   | Normal       | 1.0363   | 0.4994                 | 0.4925            |
|         | Lognormal    | 1.0329   | 0.4102                 | 0.6225            |
|         | Gamma        | 1.0363   | 0.4004                 | 0.6226            |
| Ti-44   | Normal       | 1.4187   | 0.7306                 | 0.7567            |
|         | Lognormal    | 1.4094   | 0.6706                 | 0.9728            |
|         | Gamma        | 1.4186   | 0.6500                 | 0.9502            |

### Bootstrap resampling method estimation

The third method used to estimate the FWHM of the activity ratio (C/J) distribution (independently of any parametric assumptions) is bootstrap resampling. This approach involved generating 10,000 resamples of the activity ratio data, each with replacement, and calculating the FWHM for each resampled dataset. A custom function was implemented to perform these calculations using the `replicate()` function with `replace = TRUE`.

Figure 4.8 shows the distribution of FWHM values obtained from the bootstrap resampling method for the Co-60 activity ratio (C/J) distribution. The mean FWHM from this distribution was then used to estimate the uncertainty. The results were 0.3455 for Co-60 and 1.0395 for Ti-44.

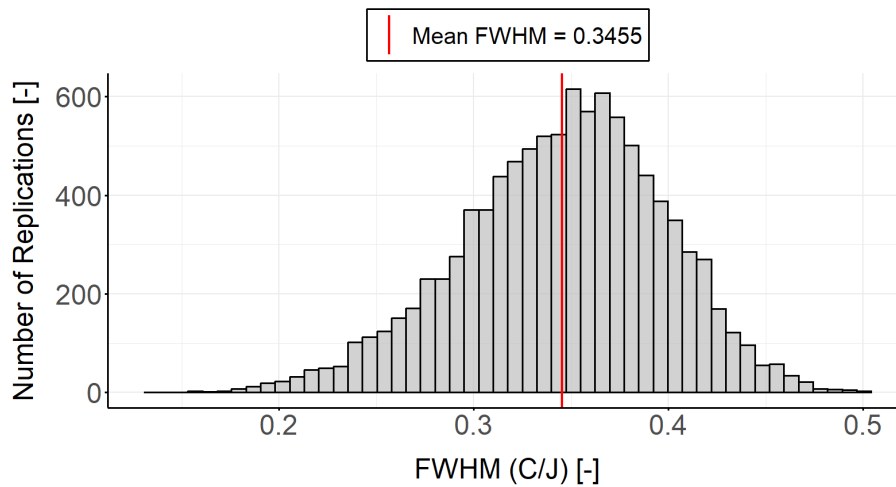


Figure 4.8: Histogram of the FWHM values obtained from bootstrap resampling of the Co-60 activity ratio (C/J).

An optimal bandwidth for visualisation purposes can be selected by adjusting its value such that the FWHM matches the one obtained through the bootstrap resampling method. Figures 4.9 and 4.10 illustrate the resulting histograms of the Co-60 and Ti-44 activity ratios between CERN and Jacobs alongside the density distributions with the optimal bandwidths. The lower optimal bandwidth for Co-60 yielded a density curve that closely matched the histogram, whereas a broader density curve was observed for Ti-44. It is important to emphasise that the FWHM of the activity ratio (C/J) distribution determines the optimal bandwidth, not the reverse. The bias visible in the plot for Ti-44 will be discussed in a later subsection.

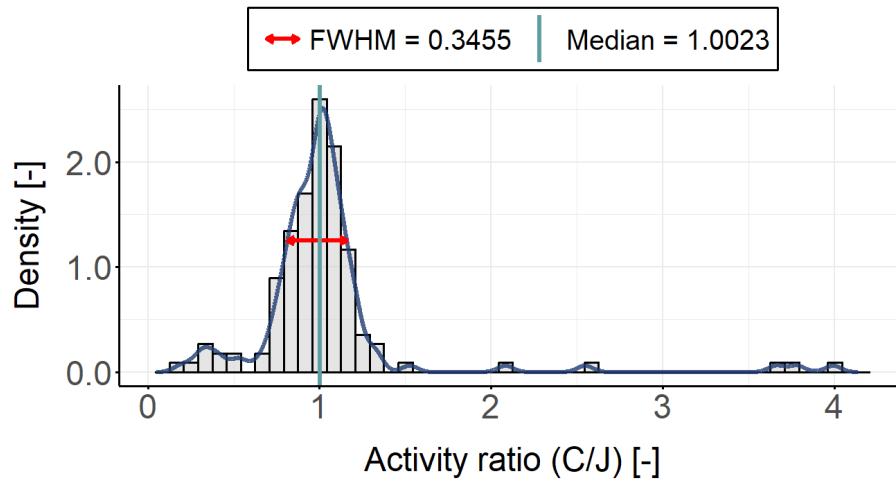


Figure 4.9: Histogram and density estimate of the Co-60 activity ratios between CERN and Jacobs (C/J), using an optimal bandwidth of 0.0477 derived from the bootstrap-estimated FWHM.

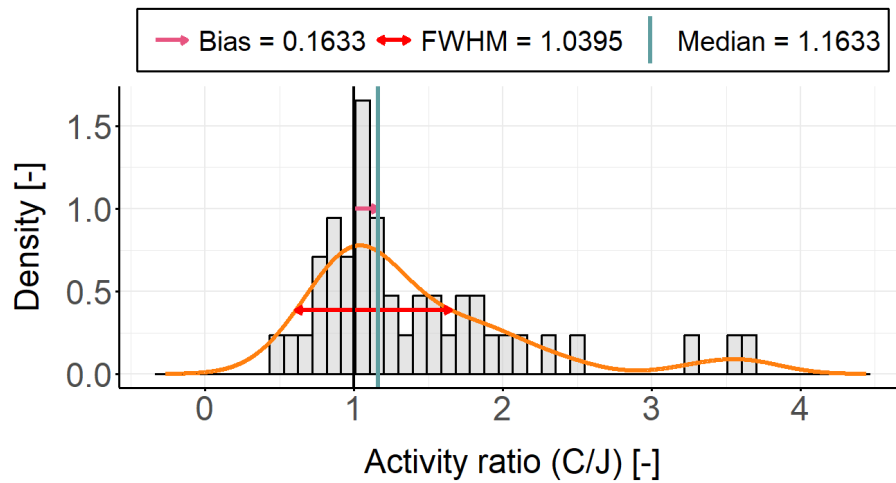


Figure 4.10: Histogram and density estimate of the Ti-44 activity ratios between CERN and Jacobs (C/J), using an optimal bandwidth of 0.2499 derived from the bootstrap-estimated FWHM.

## Discussion of the estimation of the uncertainty results

The uncertainty introduced by the envelope method was estimated using the FWHM of the activity ratio (C/J) distribution, derived through three distinct approaches. The histogram-based method was found to be unreliable due to its high sensitivity to arbitrary bin size selection and the lack of methodological rigour.

The parametric model approach, particularly the lognormal fit, yielded more stable FWHM values; however, it was still limited by imperfect model fit, as indicated by the pseudo- $R^2$  values.

In contrast, the bootstrap method provided a non-parametric and statistically robust estimate, accounting for variability across multiple resamples. Then, this method yielded the most reliable FWHM values: 0.3455 for Co-60 and 1.0395 for Ti-44. For Co-60, the narrow spread around the mode (1.0192) suggests that the use of a simplified geometry by CERN introduces only minimal uncertainty. Conversely, the broader spread observed for Ti-44 (mode at 1.0417) reflects a higher degree of inherent uncertainty.

### 4.2.3 The bias

In this study, bias is defined as the systematic deviation between the results obtained using the envelope method (CERN) and the reference measurements provided by Jacobs. Specifically, bias is calculated as the difference between the median of the activity ratio (C/J) and the ideal value of 1. An activity ratio of 1 indicates perfect agreement between the two methods; in such cases, the bias equals zero. Any deviation from this value reflects a systematic over- or underestimation by the envelope method relative to the reference.

The median is preferred over the mean in this context due to its robustness to outliers. Although the median does not account for extreme values to the same extent as the mean, it more reliably captures the central tendency in skewed distributions. This makes it a more representative measure when assessing the overall performance of the envelope method.

For Co-60, the median activity ratio (C/J) was found to be 1.0023, resulting in a bias of +0.0023. This marginally positive bias suggests a slight overestimation of activity by the envelope method relative to the reference values from Jacobs. However, the deviation is negligible and is therefore not depicted in figure 4.9 for visualisation purposes.

For Ti-44, the median activity ratio was 1.1633, corresponding to a bias of +0.1633. This higher value similarly indicates an overestimation by the envelope method, albeit to a greater extent than for Co-60. This deviation is visualised in figure 4.10 using a rightward-pointing arrow.

The skewness of the activity ratio (C/J) distributions was evaluated. Skewness quantifies the asymmetry of a distribution and offers insight into potential biases in central tendency. The skewness values were computed using equation 3.12.

While no universally accepted thresholds exist for interpreting skewness, practical guidelines suggest that values between 0 and 0.5 indicate approximate symmetry, values between  $\pm 0.5$  and  $\pm 1.0$  indicate moderate skewness, and values exceeding  $\pm 1.0$  reflect substantial skewness [55].

The skewness of the Co-60 activity ratio (C/J) distribution was calculated to be +0.0678, and that of Ti-44 was +0.3456, both suggesting nearly symmetric distributions. However, it is important to note that skewness, while offering a numerical measure of asymmetry, does not always capture the full complexity of a distribution shape. Visual inspection of the corresponding density plots is therefore essential for a more comprehensive understanding.

## 4.2.4 Discussion of results

This section provides a comprehensive discussion of the results and is divided into two subsections. The first addresses the interpretation of systematic error, uncertainty, and bias introduced by the envelope method, with a focus on differences between Co-60 and Ti-44. The second subsection compares these findings to relevant literature, highlighting methodological differences and the limitations of direct comparison.

### Interpretation of the results

A consistent trend observed in this study is the significantly lower systematic error, uncertainty, and bias for Co-60 compared to Ti-44. This is particularly apparent in the FWHM of the activity ratio (C/J) distribution and underscores the sensitivity of the envelope method to photon energy. Ti-44 emits low-energy gamma photons (67.9 and 78.3 keV), which are more prone to self-absorption and are associated with higher measurement uncertainties, both due to increased attenuation within the sample and the limitations of the detector at lower energies. These effects are further compounded by the envelope method, which may introduce additional uncertainty when applied to such low-energy emissions. In contrast, Co-60 emits higher-energy gamma rays (1173 and 1332 keV), for which both the detector response is more reliable and the envelope method yields more stable results due to reduced self-absorption and attenuation.

The challenges posed by low-energy gamma-ray emitters have been extensively documented. A study by Mirion Technologies [26] reported that detector-related uncertainties rise sharply below 100 keV, with values increasing from approximately 8% to 15% as photon energy decreases. Similar findings were observed for Am-241 (59.54 keV) in other studies [28], [29], emphasising the need for improved computational models to enhance gamma spectrometry accuracy in this energy range.

Although Ti-44 remains within the calibrated energy range of ISOCS/LabSOCS (extending down to 50 keV), measurements below 100 keV are inherently associated with greater uncertainty. These increased uncertainties stem from limitations in the detector response model, the ISOCS/LabSOCS software and elevated sensitivity to geometrical configurations and material composition. Such effects are key contributors to the discrepancies observed in Ti-44 results and highlight the critical need for careful scrutiny of measurements in the low-energy regime.

While this study focuses on Ti-44, its emission characteristics are sufficiently similar to Am-241 to invoke comparable metrological challenges. In contrast, Co-60 continues to serve as a reference nuclide of choice due to its high-energy emissions and well-established performance in gamma spectrometric assessments. This selection is consistently supported by the literature [20], [28], [29] which affirms the reliability of Co-60 in both calibration and benchmarking contexts.

Another reason the deviations for Ti-44 may appear smaller than those for Co-60 lies in the limited number of available Ti-44 samples. Although Ti-44 is, in principle, detectable, its low-energy gamma emission (78 keV) makes accurate detection more challenging compared to the higher-energy emissions of Co-60. This difficulty is closely related to the concept of secular equilibrium.

Secular equilibrium occurs in a radioactive decay chain when the half-life of the daughter radionuclide is much shorter than that of the parent, as is the case for Ti-44 and its daughter Sc-44 (half-life  $\approx 3.97$  hours). In such a system, the decay rate of the parent remains nearly constant over time, while the daughter builds up until its decay rate equals its production rate, resulting in equal and stable activities for both isotopes. Since Sc-44 emits a high-energy gamma ray (1.15 MeV), it is more easily detected than Ti-44, whose emissions lie in a low-energy range. Therefore, Ti-44 is often quantified indirectly by measuring the activity of Sc-44, which under equilibrium conditions is equal to that of the parent [56].

However, this indirect quantification can lead to classification inconsistencies. While gamma spectrometry software such as Genie 2000 (version 2.0) typically accounts for secular equilibrium, it may be overlooked in radiochemical analyses performed by Jacobs. Consequently, samples may be reported under Sc-44 rather than Ti-44, reducing the apparent number of Ti-44 entries in the dataset. In this case, 44 samples are labelled as Ti-44, compared to 134 for Co-60. Given that statistical tests are sensitive to sample size, a more meaningful comparison between the two isotopes would ideally require a similar number of observations.

Importantly, neither Co-60 nor Ti-44 achieved the ideal median activity ratio (C/J) in the distribution of 1. A value of unity would indicate that the geometrical simplifications applied in the envelope method do not introduce systematic bias. However, this study found the median activity ratios to exceed unity in both cases, by 0.23% for Co-60 and 16.33% for Ti-44, implying systematic overestimation of activity. Although geometric simplification is a contributor to this bias, other factors also play significant roles.

In the case of Co-60, summing effects and cascade coincidences may lead to systematic deviations. As described by [28], such effects are especially relevant for nuclides like Y-88, Co-60, and Ce-139 that emit multiple gamma photons in rapid succession. When these photons are detected simultaneously, they can artificially inflate the count rate. The probability of such coincidences increases with higher detection efficiency, reduced source-to-detector distances, and larger detector volumes. Although standard correction algorithms are often applied, residual effects may still influence the results. One such algorithm is integrated into Genie-2000 Version 2.0, the gamma spectrometry software used in the CERN laboratory.

Further deviations may arise across the entire energy spectrum due to factors such as matrix composition and self-absorption effects. Neither Genie-2000 version 2.0 nor ISOCS/LabSOCS software inherently accounts for these factors; therefore, they must be explicitly incorporated through Monte Carlo-based simulations to ensure reliable activity quantification. In contrast, radiochemical analysis, by directly measuring radionuclide concentrations, circumvents the need for such modelling. Additionally, poor peak fitting, particularly in spectra with low resolution or overlapping peaks, can lead to misidentification and inaccurate area estimation. While manual inspection and software validation routines can reduce such errors, they cannot eliminate them entirely.

## Comparison with previous research

This research estimated systematic error, uncertainty, and bias using multiple complementary approaches, including Kullback–Leibler divergence, bootstrap resampling, and deviation of the median activity ratio (C/J) from unity. Nevertheless, the current literature lacks clearly defined thresholds or guidelines to assess the acceptability of discrepancies between activity estimates obtained through differing methodologies. To place these findings in a broader scientific context, a comparative evaluation with existing literature is warranted. Sections 2.1.4 and 2.2.2 provide an overview of related studies. While such comparisons offer important contextual insights, direct quantitative equivalence is precluded by substantial methodological and metrological disparities. The following discussion outlines the primary scientific limitations of these comparisons.

In [20], the GEANT3 framework was employed to simulate calibration efficiencies using simplified geometries such as boxes and spheres. The study reported deviations of +11% and −10%, indicating high sensitivity to geometric modelling assumptions. However, this work focused on absolute efficiencies at discrete gamma-ray energies, whereas the present study assesses activity ratios. Moreover, the absence of specified radionuclides in [20] precludes any direct translation of efficiencies into activity values, rendering a rigorous comparison infeasible.

A study by Canberra Industries ([28]) investigated LabSOCS-derived activity ratios for multiple radionuclides, including Co-60, using NIST-certified reference sources. Despite employing HPGe detectors in both studies, the detector models differ: [28] used an ISOXVRFY detector, while this study used an XtRa coaxial HPGe detector. Differences in crystal geometry, dead layer thickness, and endcap design can significantly affect detection efficiency, particularly at low energies. [28] reported an average activity ratio of approximately 0.93 for Co-60, suggesting underestimation, whereas this study found a median value of 1.0023, indicating slight overestimation. Given the noted differences, a direct comparison is not scientifically justified.

Finally, [29] evaluated the performance of LabSOCS and ANGLE3 using certified multi-gamma reference sources. The authors reported a relative bias of −5.28% for Co-60 when applying LabSOCS, indicative of a systematic underestimation. In contrast, the research conducted in this thesis determined a relative bias of +3.63% for Co-60, when applying the same calculation formula (equation 2.15) as reported in [29]. Although both studies employed comparable statistical techniques for bias estimation, the use of different reference standards significantly limits the potential for meaningful cross-study comparisons.

None of the reviewed studies offers a directly transferable comparator for the current investigation, which uniquely evaluates ISOCS/LabSOCS performance using radiochemical analysis as the reference. The observed deviations from ideal activity ratios can be attributed to a combination of modelling limitations and physical effects. These influences must be thoroughly considered when interpreting results and determining the reliability of computational calibration techniques in gamma spectrometry.





# Chapter 5

## Experimental activity and laboratory measurements

This chapter provides a practical overview of laboratory measurements conducted at CERN using the envelope method. The primary objective is to analyse samples with non-standard geometries and to gain hands-on experience with the ISOCS/LabSOCS software for efficiency calibration in gamma spectrometry.

The measurements described in this section are not included in the existing database. This exclusion is due to procedural constraints: under the standard protocol, each sample must first be measured at CERN and subsequently analysed by Jacobs. Within the scope of this study, such a process was impractical due to significant logistical limitations. These include the extended time required for inter-institutional sample transport, which can span several weeks to months, and the high costs involved, especially when transporting only a limited number of samples.

Although database measurements are not carried out directly, performing a selected number of independent measurements is essential to deepen the understanding of both the theoretical foundations and the practical implementation of the envelope method for efficiency calibration.

## 5.1 Objective

The Radioanalytical Laboratory at CERN is responsible for the radiological analysis of samples and waste materials produced in all CERN facilities. To ensure accurate characterisation, the laboratory employs a variety of techniques, including gamma spectrometry, alpha and beta counting, and liquid scintillation techniques. These methods allow precise identification and quantification of radionuclides to support both radiation protection and waste management objectives.

This report presents the measurement and analysis of three samples, with a particular focus on the efficiency calibration step in gamma spectrometry using the LabSOCS software. The aim is to develop proficiency in operating the software by performing key tasks such as sample preparation, detector efficiency calibration, peak fitting optimisation, radionuclide identification, and critical assessment of the generated reports.




A detailed explanation of gamma spectrometry principles and methodology is provided in section 2.1.

This report provides an in-depth analysis of one selected sample and a summary of the procedures applied to the remaining two, as the analytical procedure remains consistent across all measurements.

## 5.2 Samples and instrumentation

Three distinct samples are selected for analysis in this practical session. Each sample is assigned a unique identification number and description to ensure traceability and documentation through the internal TREC system at CERN, which centralises the recording of radiological data and metadata for analysed materials. Table 5.1 summarises the relevant information for each sample.

Table 5.1: Overview of sample characteristics used in gamma spectrometry measurements.

| Parameter              | Sample 1  | Sample 2   | Sample 3  |
|------------------------|---|--|---|
| Sample analysis number | 34809570  | 34822460   | 34812247  |
| Sample description     | Rack électronique TT  | Bandes chauffantes bakeout   | Huilles Futs 1-2-3-4 circuits hydrauliques caverne ATLAS                            |
| Mass [g]               | 7480  | 14060  | 860   |
| Visual representation  |  |  |  |

All measurements are performed using HPGe detectors of the same model: the GX4018 extended-range coaxial germanium detector manufactured by Canberra. Each system is coupled with a 7500SL cryostat and an iPA-SL preamplifier. The germanium crystal has a diameter of 60.5 mm and a length of 63.4 mm, with the front surface located 5.5 mm from the cryostat window. The system operates under a bias voltage of +3000 Vdc, with a depletion voltage of +2500 Vdc, a leakage current of 0.01 nA, and a preamplifier test point at  $-1.0$  Vdc. The system achieves a FWHM of 1.74 keV at the 1332 keV line of Co-60, and a relative efficiency of 45.0% with respect to a standard  $3'' \times 3''$  NaI(Tl) detector positioned at 25 cm from the source [44].

Sample positioning and shielding configurations are adapted to the size and shape of each sample. A range of lead castles is available in the laboratory to accommodate samples of varying volumes. Smaller samples are measured using Detector 10 (reference GE10-B17188), with the detector placed beneath the sample inside the lead shielding, as shown in figure 5.1(a). In contrast, larger samples require Detector 5 (reference GE5-B10162), which is positioned laterally relative to the sample chamber, as depicted in figure 5.1(b).



(a) Detector 10 with lead castle for small samples. (b) Detector 5 with lead castle for large samples.

Figure 5.1: Measurement setups for performing gamma spectrometry.

## 5.3 Methodology

The measurement campaign followed a systematic procedure comprising the following steps:

### Step 1: Sample preparation and characterisation

Each sample needs to be first sealed to prevent contamination, after which its mass and geometrical dimensions (height, width, and depth) need to be measured. These parameters are fundamental for efficiency calibration, as gamma-ray attenuation and detector response are highly sensitive to sample geometry and density. The material composition also needs to be estimated to account for attenuation properties.

The sample then needs to be placed inside a lead-shielded counting chamber and positioned relative to the detector based on its size. The geometry needs to ensure that the system dead time remains below 1%, where achievable, in order to minimise statistical uncertainty and data loss.

### Step 2: Detector setup and data acquisition

Samples need to be registered in the digital system using the Apex-Gamma software, which incorporates Genie-2000 Version 2.0 for activity measurement. Within the “Samples” menu, the user needs to select the appropriate sample type based on the sample origin (e.g., accelerator type or experimental context). Sample metadata then needs to be entered, including the TREC number, CR code, material type, detector, geometry, and acquisition time (which is fixed by default at 10,000 seconds). The software automatically determines the appropriate unit for reporting activity (Bq, Bq/g, or Bq/l), based on the selected sample type.

### Step 3: Efficiency calibration using ISOCS/LabSOCS

Efficiency calibration needs to be performed using the ISOCS/LabSOCS software package. Within the “Settings” menu, the “Geometry Composer” is used to define the sample geometry by selecting a predefined template that most closely resembles the physical characteristics of the sample. Figures 5.2 and 5.3 illustrate the interface for template selection and dimension input. The sample density needs to be adjusted so that the calculated mass corresponds to the measured value. Once the geometry is correctly defined, it is saved and assigned to the sample within the software.

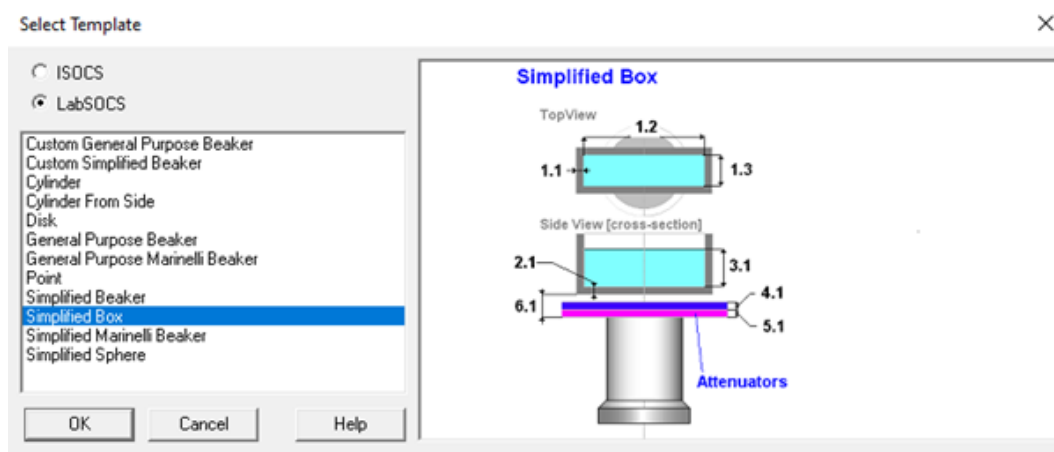


Figure 5.2: LabSOCS tab showing simplified box template in Apex-Gamma software.

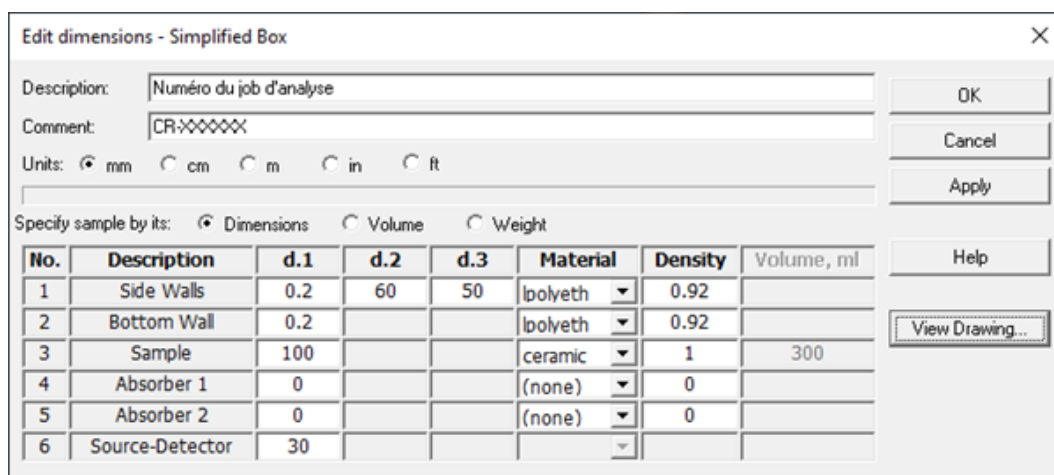


Figure 5.3: LabSOCS “Edit Dimensions” tab in a selected template.

Following geometry definition, the efficiency model needs to be generated using the “Generate LabSOCS Efficiency” function under the “Calibration” tab. This option is selected to initiate the modelling process. The option “Generate LabSOCS Efficiency” is then selected to initiate the modelling process. The resulting efficiency curve then needs to be reviewed to ensure consistency and correct shape across the relevant energy range as shown in figure 5.4.

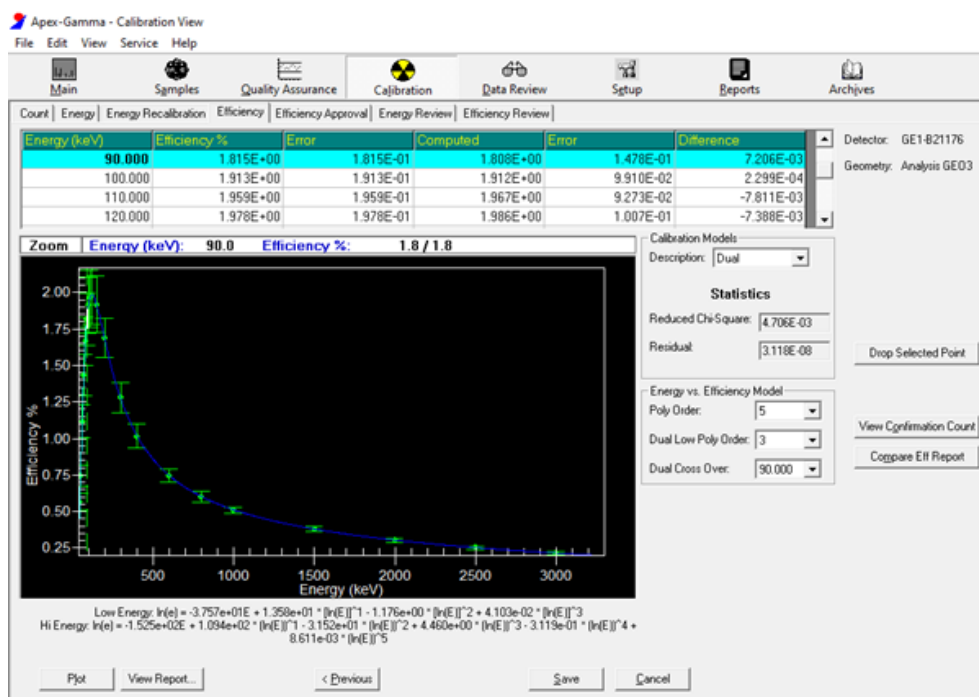


Figure 5.4: Efficiency curve in Apex-Gamma software following efficiency calibration.

#### Step 4: Spectrum acquisition and peak analysis

After calibration, the measurement needs to be launched for 10,000 seconds. The resulting spectrum needs to be reviewed for peak identification and fitting using the “Interactive Peak Fit” tool. This tool is used to verify, resize, add, or remove peaks as required to ensure accurate characterisation. An example of the peak fitting interface is provided in figure 5.5.

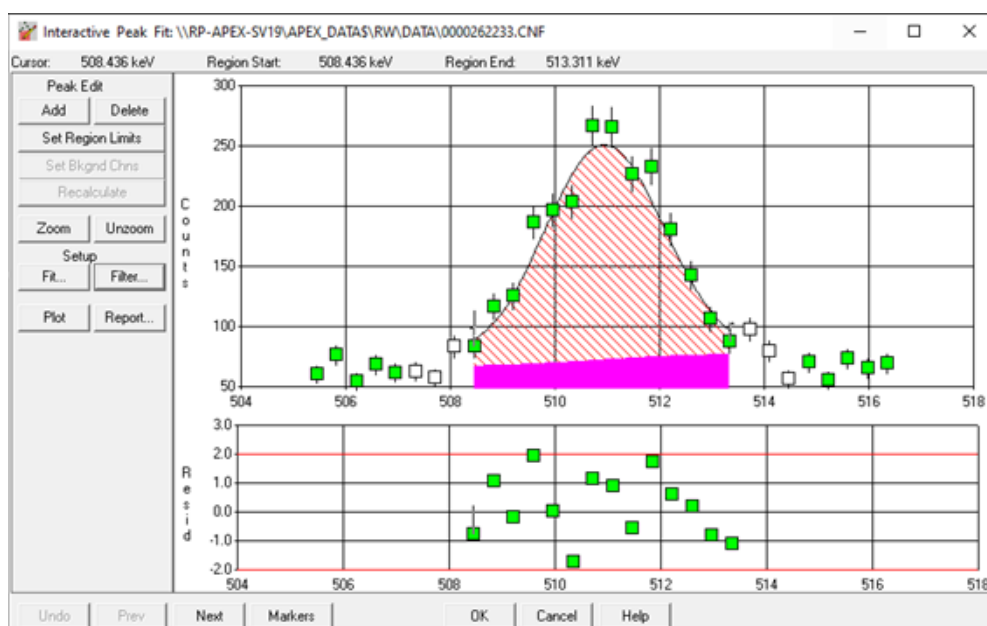


Figure 5.5: Peak fitting tab in Apex-gamma software.

Peak assignments suggested by the software need to be manually verified. When a peak can be associated with multiple radionuclides, additional emissions need to be sought to confirm the identification. Contributions from natural background radiation and decay chains need to be taken into consideration.

## 5.4 Results

Sample 1 was selected as the primary case study for detailed analysis. The complete methodology, as previously described, is applied using detector GE5-B10162. Following initial characterisation, the geometrical parameters of the sample were entered into the LabSOCS software, where the “simplified box” geometry template was identified as the most suitable match. The configuration settings used in this step are displayed in figure 5.6.

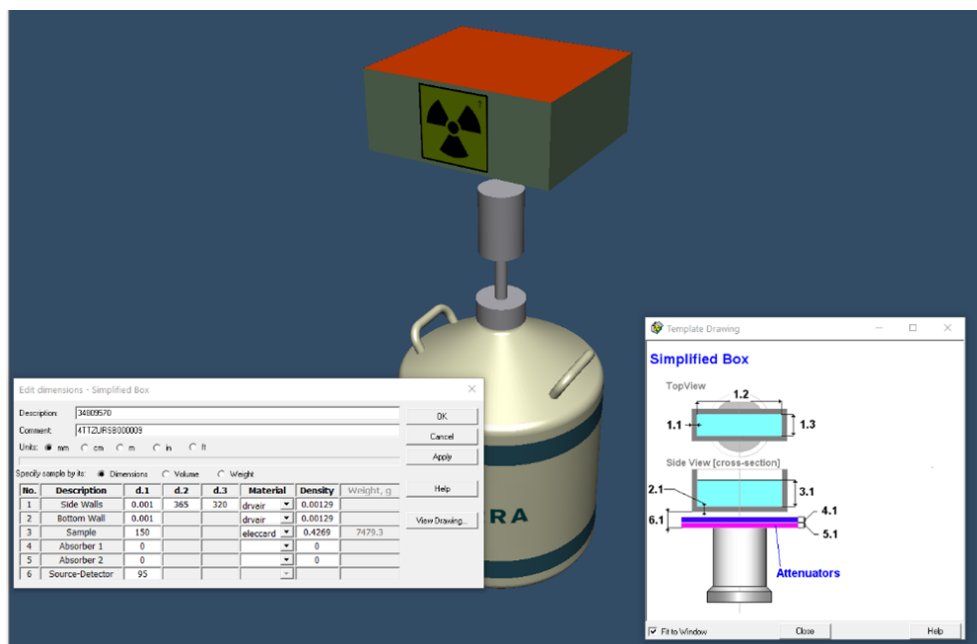


Figure 5.6: Sample 1 geometry settings using the simplified box template.

After completing the 10,000-second gamma-ray measurement, the resulting spectrum was processed through peak fitting and reanalysis routines. The acquired spectrum, annotated with its characteristic peaks, is presented in figure 5.7. Concurrently, the software generated a detailed report listing all identified peaks along with their respective activity values and associated uncertainties. These uncertainties are expressed as percentages, corresponding to a 95% confidence interval ( $2\sigma$ ). Values exceeding 100% uncertainty indicate a poor fit, typically due to incorrect peak identification, and therefore require further scrutiny. This highlights the importance of critically assessing the automated results.



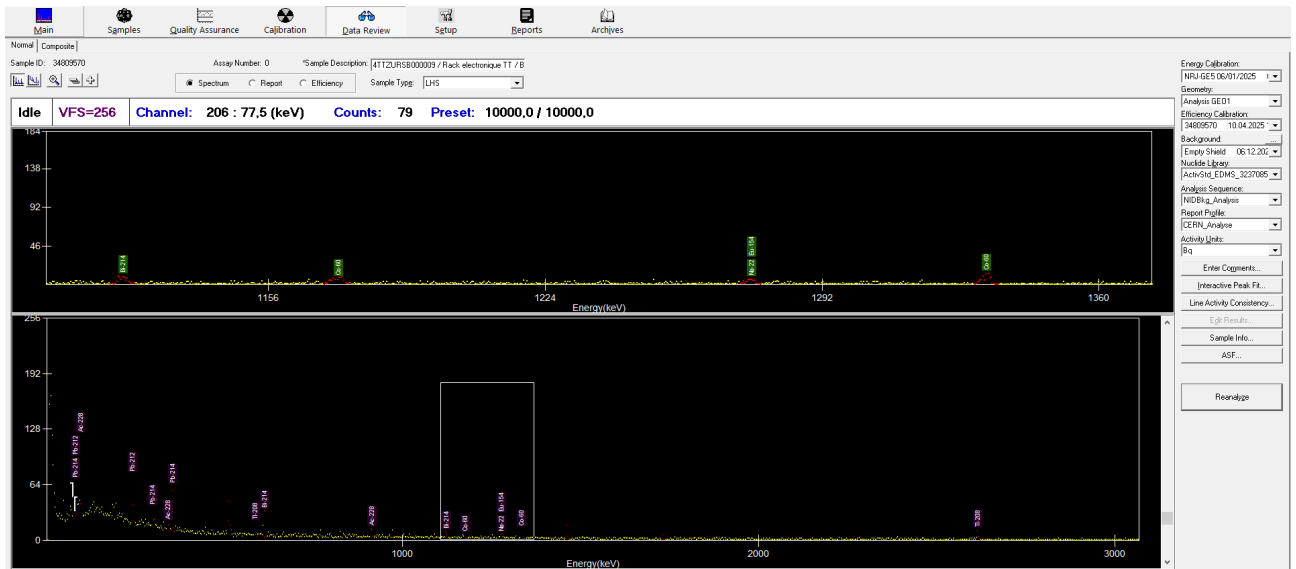


Figure 5.7: Sample 1 spectrum with characteristic peaks.

Following validation of the spectrum and review of the report, the interference-corrected nuclide list was extracted. This corrected report, automatically generated by the software, is of primary relevance for the Radiation Protection team. Table 5.2 presents the identified radionuclides, their half-lives, specific activities (in Bq/g), and corresponding relative uncertainties.

The confirmed radionuclides include Na-22, Co-60, and Eu-154. A number of additional peaks corresponding to Tl-208, Pb-212, Bi-214, Pb-214, and Ac-228 were also detected. These are considered background signals, attributable to the decay series of Th-232 and U-238, which are routinely observed in accelerator environments. Such nuclides are present in all measured samples and consistently exhibit low activity levels.

Table 5.2: Identified radionuclides for sample 1. Half-lives are expressed as Y (years), M (months), and H (hours).

| Nuclide | Halflife [time] | Activity [Bq/g] | Uncertainty [%] |
|---------|-----------------|-----------------|-----------------|
| Na-22   | 2.602E+00 Y     | 7.147E-04       | 55.2            |
| Co-60   | 5.271E+00 Y     | 2.086E-03       | 18.6            |
| Eu-154  | 8.593E+00 Y     | 2.041E-03       | 55.2            |
| Tl-208  | 3.053E+00 M     | 2.566E-03       | 30.6            |
| Pb-212  | 1.064E+01 H     | 5.919E-03       | 37.8            |
| Bi-214  | 1.990E+01 M     | 4.613E-03       | 24.8            |
| Pb-214  | 2.680E+01 M     | 3.447E-03       | 22.4            |
| Ac-228  | 6.150E+00 H     | 4.227E-03       | 31.2            |

Sample 2 was analysed using the same procedure, though a different geometry was applied. The “cylinder from the side” template was selected in LabSOCS, as it more accurately reflects the physical characteristics of this sample. No significant radionuclides were detected in sample 2, aside from those originating from the Th-232 and U-238 decay chains, which are consistently present in the environmental background.

Sample 3 was processed using the same analytical procedure as sample 1. For this sample, the “simplified box” template was again the most appropriate geometrical representation. As with sample 2, only background nuclides associated with the Th-232 and U-238 decay chains were observed in the final spectrum, with no additional radionuclides detected.



# Chapter 6

## Conclusion

This study evaluated the envelope method, implemented via ISOCS/LabSOCS software, for determining radionuclide activity in radioactive waste samples with complex geometries using gamma spectrometry. A statistical comparison was conducted between activity measurements performed by CERN, using the envelope method, and by an external reference laboratory (Jacobs), which employed radiochemical analysis. The aim was to quantify the systematic error, uncertainty, and bias introduced by the envelope method.

To assess the statistical difference between the two methods, the Wilcoxon signed-rank test was applied to the paired differences (CERN – Jacobs). This non-parametric test was selected based on the results of the Shapiro–Wilk test, which indicated that the differences were not normally distributed. At a 95% confidence level, a statistically significant difference was found for Ti-44, while no significant difference was observed for Co-60. This indicates that, for Co-60, the two methods are statistically comparable.

Systematic error was quantified using the Kullback–Leibler (KL) divergence. The KL value of 0.5528 for Co-60 suggests a moderate level of agreement between CERN and Jacobs measurements, whereas the higher KL value of 0.9331 for Ti-44 reflects a substantial deviation between the two measurement methods.

The uncertainty introduced by the envelope method was evaluated using the Full Width at Half Maximum (FWHM) of the activity ratio (C/J) distribution. Parametric model fitting revealed that a lognormal distribution provided an excellent fit for the Ti-44 activity ratio. Additionally, a non-parametric bootstrap resampling method was applied to estimate the uncertainty and ensure statistical robustness. The estimated FWHM values were 0.3455 for Co-60 and 1.0395 for Ti-44, indicating significantly higher uncertainty for the latter.

Systematic bias was assessed by comparing the median activity ratio (C/J) to the ideal value of 1. Co-60 showed negligible bias (+0.0023), whereas Ti-44 exhibited a notable positive bias of +0.1633. This suggests that the envelope method tends to overestimate activity values compared to Jacobs, particularly for Ti-44 activity.

Across all assessed metrics (error, uncertainty, and bias), Co-60 consistently showed better results than Ti-44. This disparity is attributed to the known limitations of ISOCS/LabSOCS when analysing low-energy gamma emitters (below 100 keV). Previous studies ([20], [28], [29]) support this observation, particularly for radionuclides like Am-241, which also exhibit increased variability and the presence of outliers. Additional factors contributing to deviations from the ideal activity ratio of 1 include cascade summing effects, particularly for Co-60, simplified geometry assumptions, matrix composition, self-absorption phenomena and challenges in peak fitting.

While the envelope method introduces systematic effects, its overall performance can still be considered operationally acceptable. This is largely due to its practical advantages: the envelope method is more cost-effective, time-efficient, and safer than traditional calibrations with reference sources.

Given the absence of established acceptance criteria for a comparison of this kind between two measurement methods, direct comparison with previous studies is limited. Nevertheless, the findings of this study offer a robust technical foundation for defining future performance thresholds and support the prospective implementation of the envelope method in gamma spectrometry applications at CERN and similar facilities.

In conclusion, this study contributes to the expanding research efforts on alternative calibration methods in gamma spectrometry, particularly for the complex geometries typical of radioactive waste management. By quantifying and contextualising the limitations of the envelope method, it provides evidence-based criteria for its integration in operational workflows. The findings are particularly relevant for institutions aiming to streamline radiological characterisation while ensuring traceability and regulatory compliance.

# Bibliography

- [1] CERN, “Radiation protection — hse unit at cern,” 2025. [online]. <https://hse.cern/services-support/radiation-protection>. [Accessed: Feb. 02, 2025].
- [2] CERN, “The accelerator complex,” 2025. [online]. <https://home.cern/science/accelerators/accelerator-complex>. [Accessed: Mar. 06, 2025].
- [3] R.-C. Röhrig, *Search for Dark Matter Production in Association with a Higgs Boson with the ATLAS Detector at the LHC*. München: Werner-Heisenberg-Institut, 2019. [PhD].
- [4] H. U. at CERN, “Hse-rp,” 2025. [online]. <https://hse.cern/content/hse-rp>. [Accessed: Feb. 16, 2025].
- [5] T. Frosio, N. Menaa, P. Bertreix, M. Rimlinger, and C. Theis, “A novel technique for the optimization and reduction of gamma spectroscopy geometry uncertainties,” *Applied Radiation and Isotopes*, vol. 156, Feb. 2020. Art. no. 108953.
- [6] Mirion, “Isocs / labsocs calibration methodology,” 2024. [online]. <https://www.mirion.com/isocs>. [Accessed: Nov. 17, 2024].
- [7] T. Frosio, N. Menaa, C. Duchemin, N. Riggaz, and C. Theis, “A new gamma spectroscopy methodology based on probabilistic uncertainty estimation and conservative approach,” *Applied Radiation and Isotopes*, vol. 155, Jan. 2020. Art. no. 108929.
- [8] Jacobs, “Radiochemical analysis,” 2025. [online]. <https://www.jacobs.com/solutions/markets/energy-environment/nuclear-lifecycle/radiochemical-analysis>. [Accessed: Feb. 20, 2025].
- [9] Udemy, “Cern learning,” 2025. [online]. <https://www.udemy.com/organization/home>. [Accessed: Feb. 16, 2025].
- [10] S. Topics, “Gamma spectroscopy - an overview,” 2024. [online]. <https://www.sciencedirect.com/topics/earth-and-planetary-sciences/gamma-spectroscopy>. [Accessed: Oct. 15, 2024].
- [11] G. Gilmore and D. Joss, *Practical Gamma-ray Spectrometry*. John Wiley & Sons, 2024.
- [12] B. Reyniers, *Photon Interactions*. UHasselt, 2023. [online course]. Academic year 2023-2024.

- [13] E. Vandersmissen, J. Camps, and W. Eerdeken, *Labo Stralingsfysica 2*. UHasselt, 2024. [online course]. Academic year 2023-2024.
- [14] N. Reguigui, *Gamma Ray Spectrometry*. International Atomic Energy Agency, 2014.
- [15] C. Foundation, “Flexi answers – what is the compton effect?,” 2024. [online]. <https://www.ck12.org/flexi/chemistry/photoelectric-effect-in-chemistry/what-is-the-compton-effect>. [Accessed: Nov. 10, 2024].
- [16] G. F. Knoll, *Radiation Detection and Measurement*. Hoboken, NJ: Wiley, 4th ed., 2010.
- [17] N. Power, “Interaction of gamma radiation with matter — mechanisms,” 2025. [online]. <https://www.nuclear-power.com/nuclear-power/reactor-physics/interaction-radiation-matter/interaction-gamma-radiation-matter>. [Accessed: Mar. 7, 2025].
- [18] R. Carchon, M. Moeslinger, L. Bourva, C. Bass, and M. Zendel, “Gamma radiation detectors for safeguards applications,” *Nucl. Instrum. Methods Phys. Res. Sect. Accel. Spectrometers Detect. Assoc. Equip.*, vol. 579, pp. 380–383, Aug. 2007.
- [19] M. U. Khandaker, “High purity germanium detector in gamma-ray spectrometry,” *Int. J. Fundam. Phys. Sci.*, vol. 1, pp. 42–46, June 2011.
- [20] A. Kováčik, I. Sýkora, and P. P. Povinec, “Monte carlo and experimental efficiency calibration of gamma-spectrometers for non-destructive analysis of large volume samples of irregular shapes,” *Journal of Radioanalytical and Nuclear Chemistry*, vol. 298, pp. 665–672, Oct. 2013.
- [21] V. D. Ho, B. Q. H. Phan, N. S. Pham, V. H. Dao, H. D. Tam, and M. D. Ho, “Comparison of efficiency calibration techniques of hpge detector for radioactivity measurement of soil sample in marinelli geometry,” *Journal of Radioanalytical and Nuclear Chemistry*, vol. 331, pp. 1361–1365, Mar. 2022.
- [22] H. Yoriyaz, M. Morales, P. de T. D. Siqueira, C. da C. Guimarães, F. B. Cintra, and A. dos Santos, “Physical models, cross sections, and numerical approximations used in mcnp and geant4 monte carlo codes for photon and electron absorbed fraction calculation,” *Medical Physics*, vol. 36, pp. 5198–5213, Nov. 2009.
- [23] S. Jovanovic, A. Dlabac, and N. Mihaljevic, “Angle v2.1—new version of the computer code for semiconductor detector gamma-efficiency calculations,” *Nuclear Instruments and Methods in Physics Research Section A: Accelerators, Spectrometers, Detectors and Associated Equipment*, vol. 622, pp. 385–391, Oct. 2010.
- [24] M. Technologies, “S573 isocs calibration software,” 2024. [online]. <https://www.mirion.com/products/technologies/spectroscopy-scientific-analysis/gamma-spectroscopy/gamma-spectroscopy-software/lab-applications/s573-isocs-calibration-software>. [Accessed: Nov. 17, 2024].
- [25] N. I. of Standards and T. (NIST), “X-ray mass attenuation coefficients,” 2009. [online]. <https://www.nist.gov/pml/x-ray-mass-attenuation-coefficients>. [Accessed: Apr. 15, 2025].

- [26] Mirion2025, “Technical advantages of isocs / labsocs,” 2025. [online]. <https://www.mirion.com/discover/knowledge-hub/product-literature/technical-papers/technical-advantages-of-isocs-labsocs>. [Accessed: Mar. 09, 2025].
- [27] R. Venkataraman, F. Bronson, V. Abashkevich, B. M. Young, and M. Field, “Validation of in situ object counting system (isocs) mathematical efficiency calibration software,” *Nuclear Instruments and Methods in Physics Research Section A: Accelerators, Spectrometers, Detectors and Associated Equipment*, vol. 422, pp. 450–454, Feb. 1999.
- [28] F. L. Bronson, “Validation of the accuracy of the labsocs software for mathematical efficiency calibration of ge detectors for typical laboratory samples,” *Journal of Radioanalytical and Nuclear Chemistry*, vol. 255, pp. 137–141, Jan. 2003.
- [29] B. Yang, “Performances of different efficiency calibration methods of high-purity-germanium gamma-ray spectrometry in an inter-comparison exercise,” *Nuclear Science and Techniques*, vol. 30, p. 37, Mar. 2019.
- [30] IAEA, *Report on the IAEA-CU-2006-04 ALMERA proficiency test on the determination of gamma emitting radionuclides*. Vienna: International Atomic Energy Agency, 2007. [Report].
- [31] F. Bronson, V. Atrashkevich, G. Geurkov, and B. Young, “Probabilistic uncertainty estimator for gamma-spectroscopy measurements,” *Journal of Radioanalytical and Nuclear Chemistry*, vol. 276, pp. 589–594, June 2008.
- [32] J.-W. Romijn, “Philosophy of statistics,” 2014. [online]. <https://plato.stanford.edu/entries/statistics>. [Accessed: May. 01, 2025].
- [33] Cuemath, “Hypothesis testing - definition, examples, formula, types,” 2024. Accessed: 2 December 2024.
- [34] S. Prabhakaran, “Kl divergence - what is it and mathematical details explained,” 2025. [online]. <https://www.machinelearningplus.com/machine-learning/kl-divergence-what-is-it-and-mathematical-details-explained>. [Accessed: Apr. 20, 2025].
- [35] I. Csiszar, “ $i$ -divergence geometry of probability distributions and minimization problems,” *Annals of Probability*, vol. 3, no. 1, pp. 146–158, 1975.
- [36] A. Dhinakaran, “Understanding kl divergence,” 2025. [online]. <https://towardsdatascience.com/understanding-kl-divergence-f3ddc8dff254>. [Accessed: Apr. 20, 2025].
- [37] B. Efron and R. Tibshirani, *An Introduction to the Bootstrap*. Boca Raton, FL: Chapman & Hall/CRC, 1993. Software archived 2012-07-12 at archive.today.
- [38] R Project, “R: What is r?,” 2025. [online]. <https://www.r-project.org/about.html>. [Accessed: Mar. 28, 2025].
- [39] CERN, “Trec — eam service at cern,” 2025. [online]. <https://eam-service.web.cern.ch/tool/trec>. [Accessed: Apr. 03, 2025].



- [40] CERN, “The proton synchrotron,” 2025. [online]. <https://home.cern/science/accelerators/proton-synchrotron>. [Accessed: Apr. 15, 2025].
- [41] n\_TOF Collaboration, “n\_tof - the neutron time-of-flight facility at cern,” 2025. [online]. <https://ntof-exp.web.cern.ch>. [Accessed: Apr. 15, 2025].
- [42] L. N. H. Becquerel, “Nuclear data – table,” 2025. [online]. <http://www.lnhb.fr/home/nuclear-data/nuclear-data-table>. [Accessed: Mar. 17, 2025].
- [43] I. Facility, “Isolde,” 2025. [online]. <https://isolde.web.cern.ch>. [Accessed: Apr. 15, 2025].
- [44] Mirion Technologies, “XtRa™ Extended Range Coaxial Ge Detectors,” 2025. [Online]. <https://www.mirion.com/products/technologies/spectroscopy-scientific-analysis/gamma-spectroscopy/detectors/hpge-detectors-accessories/xtra-extended-range-coaxial-ge-detectors>. [Accessed: Apr. 04, 2025].
- [45] W. J. Conover, *Practical Nonparametric Statistics*. John Wiley & Sons, Inc., 3 ed., 1999.
- [46] Z. Bobbitt, “Paired samples t-test: Definition, formula, and example,” 2025. [Online]. <https://www.statology.org/paired-samples-t-test>. [Accessed: Apr. 14, 2025].
- [47] Built In, “An introduction to the shapiro-wilk test for normality,” 2025. [Online]. <https://builtin.com/data-science/shapiro-wilk-test>. [Accessed: Apr. 14, 2025].
- [48] A. N. K. Reddy and D. K. Sagar, “Half-width at half-maximum, full-width at half-maximum analysis for resolution of asymmetrically apodized optical systems with slit apertures,” *Pramana*, vol. 84, pp. 117–126, Jan. 2015.
- [49] U. N. I. of Standards and T. (NIST), “Lognormal distribution,” 2020. [online]. <https://www.itl.nist.gov/div898/handbook/eda/section3/eda3669.htm>. [Accessed: Apr. 21, 2025].
- [50] ProbabilityCourse, “Gamma distribution,” 2024. [online]. <https://www.probabilitycourse.com/chapter8/822gammadistribution>. [Accessed: Apr. 21, 2025].
- [51] N. S. Cole, “Bias in testing,” *American Psychologist*, vol. 36, no. 10, pp. 1067–1077, 1981.
- [52] A. Sharma, “Understanding skewness in data and its impact on data analysis,” 2025. [Online]. <https://www.analyticsvidhya.com/blog/2020/07/what-is-skewness-statistics>. [Accessed: Apr. 21, 2025].
- [53] D. Science, “Top probability & statistics interview questions,” 2024. [online]. <https://365datascience.com/career-advice/job-interview-tips/probability-and-statistics-interview-questions-for-data-scientists>. [Accessed: May. 02, 2025].
- [54] L. M. Spineli, “Local inconsistency detection using the kullback–leibler divergence measure,” *Systematic Reviews*, vol. 13, p. 261, Oct 2024.

- [55] P. T. von Hippel, “Mean, median, and skew: Correcting a textbook rule,” *Journal of Statistics Education*, vol. 13, no. 2, 2005.
- [56] J. R. Prince, “Comments on equilibrium, transient equilibrium, and secular equilibrium in serial radioactive decay,” *J. Nucl. Med.*, vol. 20, no. 2, pp. 162–164, 1979.



## **Annex A**

# **Gamma spectrometry report CERN**



9/30/2020 3:58:47PM

Page 1 of 7

Analysis\_CERN\_REV\_D

Analysis Report for 28530988

PSAM-005275/Echan.FMA SAS2/Aluminium/125g/Fa4/Box@126cm/R.Charousset

---

## HSE-RP RADIO-ANALYTICAL LAB - GAMMA SPECTROSCOPY ANALYSIS

---

Sample Number : 196606  
Sample Identification : 28530988  
Sample Description : PSAM-005275/Echan.FMA  
SAS2/Aluminium/125g/Fa4/Box@126cm/R.Charousset  
Sample Type : STS  
Sample Size : 1.000E+00 units  
Facility : RP  
Detector Name : ISR7-FA4-1300038  
Operator : Operator 2  
Sample Taken / Activity reported On : 9/30/2020 11:11:49AM  
Acquisition Started : 9/30/2020 11:11:49AM  
Procedure : Aquisition  
Live Time : 1800.0 seconds  
Real Time : 1812.2 seconds  
Dead Time : 0.67 %

Peak Locate Threshold : 3.00  
Peak Locate Range (in channels) : 25 - 8192  
Peak Area Range (in channels) : 25 - 8192  
Identification Energy Tolerance : 1.000 keV  
Geometry : Analysis GEO2  
Energy Calibration Used Done On : 9/28/2020 9:09:02AM  
Efficiency Calibration Used Done On : 9/30/2020 2:50:36PM  
Efficiency Calibration Description : 28530988  
Background File : \\rp-apex-server\ROOT\RP\Data\0000174603.CNF

ATTENTION, nous consulter pour éviter toute  
erreur d'interprétation  
Rapport détaillé / officiel fourni à la demande

La décision de l'élimination du matériel  
(en tant que déchet conventionnel ou radioactif)  
appartient au donneur d'ordre

Analysé par : \_\_\_\_\_  
Vu et vérifié par : \_\_\_\_\_

Analysis Report for 28530988

PSAM-005275/Echan.FMA SAS2/Aluminium/125g/Fa4/Box@126cm/R.Charousset

First Approver : Operator 2  
 First Approver Date : 9/30/2020 3:58:39PM  
 Second Approver :  
 Second Approver Date :

---

## NUCLIDE IDENTIFICATION REPORT

---

Nuclide Library Used : \\rp-apex-server\ROOT\RP\Library\ACTIVSTD.NLB

---

### IDENTIFIED NUCLIDES

---

| <b>Nuclide Name</b> | <b>Half Life</b> | <b>Conf.</b> | <b>Energy (keV)</b>             | <b>Yield(%)</b>       | <b>Activity (Bq/units)</b> | <b>Activity Unc. ( % )</b> | <b>Comment</b>           |
|---------------------|------------------|--------------|---------------------------------|-----------------------|----------------------------|----------------------------|--------------------------|
| Na-22               | 2.60E+00 y       | 0.99         | 1274.53 *                       | 99.94                 | 5.53E+03                   | -                          | 26.89 ----               |
| Sc-44               | 3.93 h           | 0.99         | 1157.00 *<br>1499.00<br>2656.00 | 99.90<br>0.91<br>0.12 | 6.72E+04                   | -                          | 12.71 ----               |
| Ti-44               | 6.07E+01 y       | 0.99         | 67.88 *<br>78.34 *              | 94.40<br>96.20        | 5.62E+04<br>6.30E+04       | -                          | 18.98 ----<br>15.45 ---- |
| Co-60               | 5.27E+00 y       | 0.99         | 1173.24 *<br>1332.50 *          | 99.97<br>99.99        | 9.34E+05<br>9.40E+05       | -                          | 5.58 ----<br>5.33 ----   |

\* = Energy line found in the spectrum.

- = Manually added nuclide.

? = Manually edited nuclide.

@ = Energy line not used for Weighted Mean Activity

Energy Tolerance : 1.000 keV

Nuclide confidence index threshold = 0.30

Errors quoted at 2.000sigma

---

## INTERFERENCE CORRECTED REPORT

---

Analysis Report for 28530988

PSAM-005275/Echan.FMA SAS2/Aluminium/125g/Fa4/Box@126cm/R.Charousset

| <b>Nuclide<br/>Name</b> | <b>Half<br/>Life</b> | <b>Nuclide<br/>Id<br/>Confidence</b> | <b>Wt mean<br/>Activity<br/>(Bq/units)</b> | <b>Wt mean<br/>Activity<br/>Unc. (%)</b> | <b>MDA<br/>(Bq/units)</b> | <b>Comments</b> |
|-------------------------|----------------------|--------------------------------------|--|--|---------------------------|-----------------|
| Na-22                   | 2.60E+00 y           | 0.991                                | 5.53E+03                                   | - 26.89                                  | 3.45E+03                  |                 |
| Sc-44                   | 3.93 h               | 0.993                                | 6.72E+04                                   | - 12.71                                  | 1.14E+04                  |                 |
| Ti-44                   | 6.07E+01 y           | 0.996                                | 5.99E+04                                   | - 12.00                                  | 4.78E+03                  |                 |
| Co-60                   | 5.27E+00 y           | 0.993                                | 9.37E+05                                   | - 3.86                                   | 3.34E+03                  |                 |

? = nuclide is part of an undetermined solution

X = nuclide rejected by the interference analysis

@ = nuclide contains energy lines not used in Weighted Mean Activity

Errors quoted at 2.000sigma

Analysis Report for 28530988

PSAM-005275/Echan.FMA SAS2/Aluminium/125g/Fa4/Box@126cm/R.Charousset

---

## UNIDENTIFIED PEAKS

---

Peak Locate Performed on : 9/30/2020 2:52:08PM  
 Peak Locate From Channel : 25  
 Peak Locate To Channel : 8192

|   | <b>Peak No.</b> | <b>Energy (keV)</b> | <b>Peak Size (CPS)</b> | <b>Peak CPS (%) Uncertainty</b> | <b>Peak Type</b> | <b>Tolerance Nuclide</b> | <b>Comment</b> |
|---|-----------------|---------------------|------------------------|---------------------------------|------------------|--------------------------|----------------|
| F | 1               | 49.75               | 4.03130E-01            | 5.06                            | Tol.             | Te-132                   | -----          |
| M | 3               | 72.96               | 3.16425E-01            | 11.40                           | Tol.             | Bi-207                   | -----          |
| m | 4               | 75.11               | 5.36556E-01            | 7.32                            | Tol.             | Au-194                   | -----          |
|   |                 |                     |                        |                                 |                  | Bi-207                   | -----          |
|   |                 |                     |                        |                                 |                  | Ra-226                   | -----          |
|   |                 |                     |                        |                                 |                  | Th-232                   | -----          |
| F | 6               | 84.94               | 1.54265E-01            | 26.95                           | Tol.             | Bi-207                   | -----          |
| F | 7               | 510.87              | 3.37700E+00            | 1.57                            |                  |                          | -----          |

---

M = First peak in a multiplet region  
 m = Other peak in a multiplet region  
 F = Fitted singlet  
 Errors quoted at 2.000sigma

---



---

## NUCLIDE MDA REPORT

---

Nuclide Library Used : \\rp-apex-server\ROOT\RP\Library\ACTIVSTD.NLB

|   | <b>Nuclide Name</b> | <b>Nuclide MDA (Bq/units)</b> |
|---|---------------------|-------------------------------|
|   | Be-7                | 4.45E+04                      |
| + | Na-22 *             | 3.45E+03                      |
|   | Na-24               | 9.43E+02                      |
|   | Al-26               | 2.05E+03                      |
|   | Cl-38               | 4.42E+03                      |
|   | Cl-39               | 4.57E+03                      |
|   | K-40                | 8.42E+04                      |
|   | Ar-41               | 3.85E+03                      |



Analysis Report for 28530988

PSAM-005275/Echan.FMA SAS2/Aluminium/125g/Fa4/Box@126cm/R.Charousset

| <b>Nuclide Name</b> |        |   | <b>Nuclide MDA<br/>(Bq/units)</b> |
|---------------------|--------|---|-----------------------------------|
|                     |        |   |                                   |
|                     | K-42   |   | 1.46E+04                          |
|                     | K-43   |   | 5.04E+03                          |
| +                   | Sc-44  | * | 1.14E+04                          |
|                     | Sc-44m |   | 4.45E+03                          |
| +                   | Ti-44  | * | 4.78E+03                          |
|                     | Sc-46  |   | 8.69E+03                          |
|                     | Ca-47  |   | 5.52E+03                          |
|                     | Sc-47  |   | 5.16E+03                          |
|                     | Sc-48  |   | 3.67E+03                          |
|                     | V-48   |   | 3.77E+03                          |
|                     | Cr-51  |   | 4.30E+04                          |
|                     | Mn-52  |   | 1.94E+03                          |
|                     | Mn-54  |   | 7.31E+03                          |
|                     | Co-55  |   | 1.32E+04                          |
|                     | Co-56  |   | 4.14E+03                          |
|                     | Ni-56  |   | 3.58E+03                          |
|                     | Co-57  |   | 4.41E+03                          |
|                     | Co-58  |   | 6.95E+03                          |
|                     | Fe-59  |   | 8.96E+03                          |
| +                   | Co-60  | * | 3.34E+03                          |
|                     | Cu-64  |   | 4.67E+05                          |
|                     | Ni-65  |   | 7.88E+03                          |
|                     | Zn-65  |   | 1.84E+04                          |
|                     | Zn-69  |   | 4.77E+03                          |
|                     | Zn-72  |   | 4.33E+03                          |
|                     | Se-75  |   | 6.24E+03                          |
|                     | As-76  |   | 1.02E+04                          |
|                     | Br-77  |   | 1.74E+04                          |
|                     | Br-82  |   | 6.57E+03                          |
|                     | Rb-83  |   | 1.02E+04                          |
|                     | Sr-85  |   | 8.85E+03                          |
|                     | Sr-85m |   | 4.67E+03                          |
|                     | Kr-88  |   | 4.78E+03                          |
|                     | Rb-88  |   | 7.17E+03                          |
|                     | Y-88   |   | 1.55E+03                          |
|                     | Zr-88  |   | 4.57E+03                          |
|                     | Zr-89  |   | 9.46E+03                          |
|                     | Mo-90  |   | 4.84E+03                          |
|                     | Sr-91  |   | 2.62E+04                          |
|                     | Nb-95  |   | 6.76E+03                          |
|                     | Nb-95m |   | 1.58E+04                          |
|                     | Zr-95  |   | 1.18E+04                          |
|                     | Tc-96  |   | 6.73E+03                          |
|                     | Zr-97  |   | 6.82E+03                          |

Analysis Report for 28530988

PSAM-005275/Echan.FMA SAS2/Aluminium/125g/Fa4/Box@126cm/R.Charousset

| <b>Nuclide<br/>Name</b> | <b>Nuclide MDA<br/>(Bq/units)</b> |
|-------------------------|-----------------------------------|
| Mo-99                   | 3.99E+03                          |
| Tc-99                   | 4.07E+03                          |
| Ru-103                  | 5.01E+03                          |
| Ag-105                  | 6.87E+03                          |
| Rh-105                  | 2.20E+04                          |
| Ag-106                  | 7.98E+03                          |
| Ru-106                  | 5.28E+04                          |
| Ag-108m                 | 4.91E+03                          |
| Cd-109                  | 4.50E+03                          |
| Ag-110m                 | 5.80E+03                          |
| Sn-113                  | 3.30E+03                          |
| In-114                  | 9.39E+03                          |
| Te-121                  | 2.94E+03                          |
| Sb-122                  | 6.66E+03                          |
| Te-123                  | 3.60E+03                          |
| I-124                   | 3.18E+03                          |
| Sb-124                  | 3.86E+03                          |
| I-125                   | 1.33E+03                          |
| Sb-125                  | 2.45E+03                          |
| Xe-125                  | 1.48E+03                          |
| I-126                   | 4.42E+03                          |
| Sb-126                  | 5.44E+03                          |
| Xe-127                  | 2.11E+03                          |
| I-130                   | 4.68E+03                          |
| Ba-131                  | 1.14E+03                          |
| I-131                   | 5.43E+03                          |
| Te-132                  | 2.13E+03                          |
| Ba-133                  | 9.40E+02                          |
| Cs-134                  | 5.29E+03                          |
| Cs-136                  | 7.19E+03                          |
| Cs-137                  | 6.47E+03                          |
| Ce-139                  | 9.87E+02                          |
| Ba-140                  | 7.18E+03                          |
| La-140                  | 2.53E+03                          |
| Ce-141                  | 3.45E+03                          |
| Ce-144                  | 6.79E+03                          |
| Eu-152                  | 5.20E+02                          |
| Eu-154                  | 1.13E+03                          |
| Hf-181                  | 5.78E+03                          |
| Ta-182                  | 1.66E+04                          |
| Ir-192                  | 5.07E+03                          |
| Au-194                  | 6.88E+03                          |
| Au-198                  | 4.74E+03                          |
| Tl-202                  | 4.94E+03                          |

Analysis Report for 28530988

PSAM-005275/Echan.FMA SAS2/Aluminium/125g/Fa4/Box@126cm/R.Charousset

| <b>Nuclide<br/>Name</b> | <b>Nuclide MDA<br/>(Bq/units)</b> |
|-------------------------|-----------------------------------|
| Bi-207                  | 4.89E+03                          |
| Ra-226                  | 4.02E+03                          |
| Th-232                  | 9.25E+03                          |
| U-235                   | 6.10E+03                          |
| U-238                   | 8.32E+04                          |
| Am-241                  | 2.46E+04                          |

- + = Nuclide identified during the nuclide identification
- \* = Energy line found in the spectrum
- > = MDA value not calculated
- @ = Half-life too short to be able to perform the decay correction
- ? = CAUTION: MDA value is inconsistent with Currie MDA at 95% confidence level

## DATA REVIEW COMMENTS REPORT

| <b>Creation Date</b> | <b>Comment</b> | <b>User</b> |
|----------------------|----------------|-------------|
|----------------------|----------------|-------------|

No Data Review Comments Entered.